

AERODYNAMICS OF WINGS AT LOW REYNOLDS NUMBERS:  
BOUNDARY LAYER SEPARATION AND REATTACHMENT

by

John McArthur

---

A Dissertation Presented to the  
FACULTY OF THE GRADUATE SCHOOL  
UNIVERSITY OF SOUTHERN CALIFORNIA  
In Partial Fulfillment of the  
Requirements for the Degree  
DOCTOR OF PHILOSOPHY  
(AEROSPACE AND MECHANICAL ENGINEERING)

December 2008

Copyright 2008

John McArthur

# Epigraph

Only through hard work, perseverance, and intellect can men hope to improve their condition, both individually and collectively. Effort must be made in the basic sciences to understand and mathematically model the physical world around us, the engineering sciences to simplify those models and make them beneficial to others, as well as history, economics and politics, to ensure that the benefits are distributed to the public fairly, without unjust bias or incorrect beliefs.

This paper focuses on the first two, however, it is the latter that is so desperately needed in our current era of high-technology. Without it, the potential benefit gained by the sciences will be selfishly hidden and used for destructive purposes.

# Dedication

to my parents for raising me right

...and to the mystery that is reality

# Acknowledgments

This dissertation would not have been possible were it not for the guidance, advise, support, and assistance of my advisor, Dr. Geoff Spedding. It is with deep gratitude that I give appreciation for his efforts. I know I haven't always been the best student, but he was there to help me when needed. This is also true of Dr. Fred Browand, who often filled in for my advisor when he was traveling. Besides that, Dr. Browand was a great mentor and always gave sound advise on the path my research should follow.

Additional guidance was provided by Dr. Larry Redekopp and Dr. Ron Blackwelder. While taking an independent study course on fluid dynamic instability, Dr. Redekopp gave much insight and assistance in understanding instability mechanisms and writing codes to solve the stability equations. Early in my graduate studies, Dr. Blackwelder supported my efforts of designing and building a small scale flying vehicle. This was a major factor in my interest in my later PhD research, and quite possibly explains the long hours spent on the project.

The support of my family was crucial, and very much appreciated. While they didn't always understand what I was doing, or why I was doing it, they were always willing to listen to me as I drifted into my own little world, describing my research. That helped tremendously, and without their support and love, I wouldn't have been able to accomplish this work.

One great source of support were the friends that I have made at USC, and that list is very long and I can't possibly hope to include everyone, but it would include both undergraduate and graduate classmates, members of the Engineering Graduate Student Association, and numerous staff members throughout USC. To name a few: Brian Wetzel, Eric Geller, Stephane Gallet, Cecile Braun, Sonya Collier, Karthikeyan Chockalingham, Bardia Zandian, Marrietta Penoliar, Carolyn Suckow, Margery Berti, and Samantha Graves. Their support and distraction were very helpful.

Finally, and most importantly, was the great love, devotion and support of my girlfriend, current fiancee, and future wife: Huafen Qiao. She has been a constant aid in my pursuit, and was very helpful in staying focused on the work while making sure life wasn't too depressing and dull. She was great at planning trips and activities that were short but fun. Despite the ridiculous amount of time I spent on my work in the past year, she was never (or should I say rarely?) upset by how busy I was and the little time I had to devote to spending quality time together. She understands the importance of education and success, and I am so thankful for having met her. I look forward to spending the rest of my life with her and raising a beautiful family.

# Table of Contents

<b>Epigraph</b>	<b>ii</b>
<b>Dedication</b>	<b>iii</b>
<b>Acknowledgments</b>	<b>iv</b>
<b>List of Figures</b>	<b>viii</b>
<b>Abstract</b>	<b>xi</b>
<b>1 Chapter One: Introduction</b>	<b>1</b>
1.1 Motivation . . . . .	1
1.2 Nomenclature . . . . .	4
1.3 Low Reynolds Number Aerodynamics . . . . .	5
1.4 Laminar Separation Bubble . . . . .	17
1.5 Leading Edge Vortex . . . . .	28
<b>2 Chapter Two: Problem Statement</b>	<b>34</b>
2.1 Model Geometry . . . . .	34
2.2 Force Measurements . . . . .	34
2.3 Eppler 387 Performance . . . . .	35
2.4 Laminar Separation Bubble . . . . .	36
2.5 Leading Edge Vortex . . . . .	36
<b>3 Chapter Three: Proposal</b>	<b>38</b>
<b>4 Chapter Four: Methods</b>	<b>40</b>
4.1 Models . . . . .	40
4.1.1 Rectangular Wings . . . . .	40
4.1.2 Swept Wings . . . . .	42
4.2 Flow Facilities . . . . .	42
4.2.1 Wind Tunnel . . . . .	42
4.2.2 Water Channel . . . . .	46

4.3	Measurement Techniques . . . . .	46
4.3.1	Force Balance . . . . .	46
4.3.2	Particle Image Velocimetry . . . . .	51
4.3.3	Dye Visualization . . . . .	55
<b>5</b>	<b>Chapter Five: Result</b>	<b>56</b>
5.1	Aerodynamics at Re=10k and 20k . . . . .	56
5.1.1	Force Balance Measurements . . . . .	56
5.1.2	Comparison with External Sources . . . . .	64
5.1.3	Separation point . . . . .	71
5.2	Laminar Separation Bubble . . . . .	77
5.2.1	Force Balance Measurements . . . . .	77
5.2.2	Comparison with External Sources . . . . .	82
5.2.3	Flow Field Measurements . . . . .	88
5.2.4	Separation Point . . . . .	92
5.2.5	Roughness . . . . .	96
5.3	Leading Edge Vortex . . . . .	97
5.3.1	Dye Visualization . . . . .	97
5.3.2	Smoke Visualization . . . . .	101
5.3.3	Force Measurements . . . . .	105
<b>6</b>	<b>Chapter Six: Conclusions</b>	<b>108</b>
	<b>References</b>	<b>114</b>

# List of Figures

1.1	The critical Re (Schmitz) . . . . .	6
1.2	Maximum Lift-to-Drag vs Reynolds number (McMasters) . . . . .	7
1.3	Lift curves for NACA 66 <sub>3</sub> -018 airfoil (Mueller) . . . . .	9
1.4	Drag polar of Eppler 387 airfoil at various Re . . . . .	10
1.5	Spanwise variation of the wake (Selig) . . . . .	12
1.6	Effect of end plates on force balance measurements (Mueller) . . . . .	13
1.7	Lift to Drag ratio for three airfoil shapes (Laitone) . . . . .	15
1.8	Lift curve for NACA 0012 in various conditions (Laitone) . . . . .	16
1.9	Description of a laminar separation bubble. (Mueller) . . . . .	18
1.10	Drag polar of a SD7003 airfoil at various Re. (Selig) . . . . .	23
1.11	The laminar separation bubble for the SD7003 airfoil (Ol) . . . . .	24
1.12	Lift and drag of a flat plate airfoil (Mohseni) . . . . .	25
1.13	The laminar separation bubble on the SD7003 airfoil (Radespiel) . . . . .	27
1.14	Drag polar for SD7003 airfoil. (Radespiel) . . . . .	28
1.15	The vortex formed near the leading edge (Maxworthy) . . . . .	30
1.16	The vortex formed by a model hawkmoth (Van Den Berg) . . . . .	31
1.17	The vortex formed by a free flying butterfly (Srygley) . . . . .	32
1.18	The vortex formed by a model swift wing (Videler) . . . . .	33
4.1	Three airfoil shapes studied . . . . .	41

4.2	Swept wing planforms . . . . .	43
4.3	The USC Dryden wind tunnel test section . . . . .	44
4.4	Wind tunnel turbulence uniformity . . . . .	45
4.5	Water channel with wing . . . . .	47
4.6	Force balance planform . . . . .	48
4.7	Drag calibration results . . . . .	52
5.1	Airfoil force coefficients at $Re = 1 \times 10^4$ . . . . .	57
5.2	Airfoil force coefficients at $Re = 2 \times 10^4$ . . . . .	58
5.3	Drag polar at $Re = 1 \times 10^4$ . . . . .	60
5.4	Drag polar at $Re = 2 \times 10^4$ . . . . .	61
5.5	Lift-to-drag ratio at $Re = 1 \times 10^4$ . . . . .	62
5.6	Lift-to-drag ratio at $Re = 2 \times 10^4$ . . . . .	63
5.7	Flat plate polars from literature . . . . .	65
5.8	Flat plate polar comparison . . . . .	66
5.9	Flat plate drag coefficient at zero incidence . . . . .	67
5.10	Cambered plate results from literature . . . . .	68
5.11	Cambered plate at low $Re$ . . . . .	69
5.12	Lifting line theory . . . . .	70
5.13	Separation line for cambered plate . . . . .	72
5.14	Separation point of cambered plate and Eppler 387 . . . . .	73
5.15	Method of measuring separation point . . . . .	74
5.16	Separation point related to forces . . . . .	75
5.17	Eppler 387 forces . . . . .	78
5.18	Eppler 387 lift-to-drag ratio . . . . .	79
5.19	Eppler 387 drag polar . . . . .	81

5.20	Eppler 387 drag polar for 2D and 3D . . . . .	83
5.21	Lifting line theory - Eppler 387 . . . . .	84
5.22	Eppler 387 hysteresis . . . . .	85
5.23	Eppler 387 drag polar for 2D and all previous 60k measurements . . . . .	86
5.24	Eppler 387 drag polar for 2D and UIUC . . . . .	87
5.25	E387 flow fields at Re=30k . . . . .	89
5.26	High Resolution DPIV at Re=30k, $\alpha = 8^\circ$ . . . . .	90
5.27	High Resolution DPIV at Re=30k, $\alpha = 12^\circ$ . . . . .	91
5.28	Boundary layer profile at Re=30k, $\alpha = 12^\circ$ . . . . .	92
5.29	Instantaneous high resolution flow field . . . . .	93
5.30	Instantaneous boundary layer profile . . . . .	94
5.31	Separation streakline for E387 . . . . .	95
5.32	Separation point vs angle of attack for E387 . . . . .	95
5.33	Comparison at Re=40k . . . . .	97
5.34	Comparison at Re=40k . . . . .	98
5.35	Sketches of Dye Visualization Experiments . . . . .	99
5.36	Dye visualization of LEV . . . . .	100
5.37	Dark region indicating vortex on wing . . . . .	101
5.38	Vortex illuminated by particles . . . . .	103
5.39	Vortex spanwise development . . . . .	104
5.40	Swept wing force coefficients . . . . .	106
5.41	Swept wing lift-to-drag ratio . . . . .	107

# Abstract

Due to advances in electronics technology, it is now possible to build small scale flying and swimming vehicles. These vehicles will have size and velocity scales similar to small birds and fish, and their characteristic Reynolds number will be between  $10^4$  and  $10^5$ . Currently, these flying and swimming vehicles do not perform well, and very little research has been done to characterize them, or to explain why they perform so poorly. This dissertation documents three basic investigations into the performance of small scale lifting surfaces, with Reynolds numbers near  $10^4$ .

## **Part I. Low Reynolds number aerodynamics**

Three airfoil shapes were studied at Reynolds numbers of 1 and  $2 \times 10^4$ : a flat plate airfoil, a circular arc cambered airfoil, and the Eppler 387 airfoil. Lift and drag force measurements were made on both 2D and 3D conditions, with the 3D wings having an aspect ratio of 6, and the 2D condition being approximated by placing end plates at the wing tips.

Comparisons to the limited number of previous measurements show adequate agreement. Previous studies have been inconclusive on whether lifting line theory can be applied to this range of  $Re$ , but this study shows that lifting line theory can be applied when there are no sudden changes in the slope of the force curves. This is highly dependent on the airfoil shape of the wing, and explains why previous studies have been inconclusive.

## **Part II. The laminar separation bubble**

The Eppler 387 airfoil was studied at two higher Reynolds numbers: 3 and  $6 \times 10^4$ . Previous studies at a Reynolds number of  $6 \times 10^4$  had shown this airfoil experiences a drag increase at moderate lift, and a subsequent drag decrease at high lift. Previous studies suggested that the drag increase is caused by a laminar separation bubble, but the experiments used to show this were conducted at higher Reynolds numbers and extrapolated down.

Force measurements were combined with flow field measurements at Reynolds numbers 3 and  $6 \times 10^4$  to determine whether the drag increase is really caused by the formation of a laminar separation bubble. The results clearly indicate that the reverse is true, and that the subsequent drag decrease is caused by the laminar separation bubble.

## **Part III. The leading edge vortex**

Four wings with different sweep angles were studied at Reynolds number  $5 \times 10^4$ : sweep angles of  $0^\circ$ ,  $20^\circ$ ,  $40^\circ$ , and  $60^\circ$ . The wings had a simple cambered plate airfoil similar to the cambered airfoil of part I above. Each wing was built to have the same aspect ratio, wing area, and streamwise airfoil shape. Previous studies on bird wings speculate that simply sweeping the wings can cause a leading edge vortex to form, which could cause substantial improvements in performance. However, these studies were not well controlled, and were conducted from a biological perspective.

Qualitative and quantitative flow field measurements were combined with force measurements to conduct a well controlled engineering experiment on the formation and effect of a leading edge vortex on simple swept wings. A stable vortex was found to form over the  $60^\circ$  swept wing at one particular angle of attack, but it was not similar to the traditional notion of a leading edge vortex. The vortex has a small radius, and

extends over little of the span. Force measurements indicate that the vortex has no significant impact on the forces measured. Thus, simply sweeping a wing is not sufficient to form a significant leading edge vortex, and other effects must be considered.

# Chapter 1

## Introduction

### 1.1 Motivation

Advances in energy and actuator technologies make it possible to build small scale flying devices with mean wing chords of 5 cm flying at about 10 m/s. Sensor technology is making these size vehicles useful for military and civilian purposes. In the energy field, lithium batteries have energy and power densities that often double nickel-metal-hydride batteries. New actuators, such as muscle wire and magnet-coils, are lighter and smaller than traditional servo actuators. A variety of sensors, including optical and chemical, have decreased dramatically in size and weight due to advances in electronics. Aircraft at this size and speed could have many uses in military reconnaissance, traffic monitoring, search and rescue, and forest fire detection. [26]

Planes of this size and speed have been built and flown for nearly a decade, starting with the Black Widow built by Aerovironment, and continuing with others, including universities that compete in the annual Micro Air Vehicle (MAV) competition. [10] However, these flying vehicles still have small endurance and range compared with other flying vehicles, are quite inefficient, and have low payload to airframe weight ratios. The payload to takeoff weight ratio of a Boeing 747 is approximately 20%, while that of a typical MAV is just 10%. Hence, MAVs are not widely used. These planes could prove to be useful if these characteristics were improved.

To improve the endurance, range, efficiency and payload capacity of these vehicles, one could look to lighter materials, higher energy density power systems, high

efficiency power systems, or the aerodynamics of the vehicle. This thesis concerns the aerodynamics of the vehicle, and specifically addresses lift and drag generated by the fluid dynamics of particular airfoils and wings for the small scale air vehicles described above.

A useful non-dimensional parameter in the study of aerodynamics is the Reynolds number (Re). This can be seen in the non-dimensional form of the Navier-Stokes equations, which are the equations that govern fluid motion. For an incompressible, Newtonian fluid, these equations have the form:

$$\begin{aligned}\nabla \cdot \mathbf{u} &= 0 \\ \frac{\partial \mathbf{u}}{\partial t} + (\mathbf{u} \cdot \nabla) \mathbf{u} &= \nabla p + \frac{1}{\text{Re}} \nabla^2 \mathbf{u}\end{aligned}\tag{1.1}$$

where  $\nabla$  is the spatial gradient operator normalized by some length scale (L),  $\mathbf{u}$  is the velocity vector normalized by some velocity scale (U),  $t$  is the time normalized by the convective time scale ( $\frac{L}{U}$ ),  $p$  is the pressure normalized by the dynamic pressure ( $\rho U^2$ ), and  $\rho$  is the fluid density. With these normalizations, the Re is defined as:

$$\text{Re} = \frac{\rho U L}{\mu}$$

where  $\mu$  is the fluid viscosity. Since the numerator of the Reynolds number is composed of mass, velocity and size, and the denominator consists of viscosity, the Reynolds number can be thought of as the ratio of inertial forces to viscous forces in the flow. When viscosity is dominant, the flow is laminar and smooth because viscosity distributes and transports momentum throughout the flow. This can be seen in equation 1.1 because with large viscosity, Re will be small. With sufficiently small Re, the Laplacian term on the right will dominate the Navier-Stokes equations and govern the fluid dynamics, and

the non-linear term on the left will not significantly effect the flow. In laminar flows, time-independent boundary conditions must yield time-independent solutions. Laminar flows, with the limit  $Re$  approaching zero, can often be solved analytically, and computational solutions can be found with direct simulations of the Navier-Stokes equations.

When large inertial forces dominate the flow (ie. high  $Re$ ), then the flow becomes turbulent and disorganized because local increases in momentum cause instability. This is seen in equation 1.1 because with dominant inertial forces the  $Re$  will be large, thus the non-linear terms on the left will start to influence the dynamics. With non-linearity, time-independent boundary conditions can now generate time-dependent solutions. At sufficiently high  $Re$ , the non-linear terms dominate, and the fluid is considered fully turbulent. Direct simulations of turbulent flows are computationally expensive and are currently not practical for aircraft design. However, many approximations of the characteristics of turbulent flow have been developed, and these can be implemented in computational algorithms to get solutions that are close enough to experimental results to be useful. The use of these approximations has led to great advances in the design and performance of large, high-speed aircraft that operate at high  $Re$ .

As an example of laminar and turbulent flow, consider the boundary layer that forms on a perfectly smooth flat plate, with no external noise or turbulence in the free stream. The flat plate boundary layer has an  $Re$  that can be defined by the free-stream flow speed ( $U_\infty$ ) and the distance along the plate ( $x$ ). Thus:

$$Re_x = \frac{\rho U_\infty x}{\mu}$$

As the boundary layer travels along the plate,  $Re_x$  increases. For  $Re_x < 3 \times 10^6$ , the boundary layer is laminar, but when  $Re_x > 4 \times 10^6$ , the boundary layer is considered fully turbulent. Thus,  $3 \times 10^6 < Re_x < 4 \times 10^6$  is a transition region where there is neither laminar flow nor turbulent flow. [32] In this region, direct simulation of the

Navier-Stokes equations are typically too time consuming to be used, and conventional turbulence models will not accurately predict the fluid dynamics.

When looking at wings and airfoils, the situation is similar, but there are some differences. The main difference is the existence of a pressure gradient on the upper surface of the airfoil which effects the transitional  $Re$ . Defining an  $Re$  for an airfoil based on the airfoil chord ( $c$ ) gives:

$$Re_c = \frac{\rho U_\infty c}{\mu}$$

While this is the Reynolds number for the entire airfoil, the local Reynolds number ( $Re_x$ ) can still be considered to be the distance along the chord from the leading edge of the airfoil. When  $Re_c > 10^6$ , most of the boundary layer on the wing is turbulent, and the laminar and transitional regions have relatively little effect on the forces exerted on the wing. Thus, computations can use approximations and models for the turbulent boundary layer and get adequate results. When  $Re_c < 10^3$ , there will be sufficient viscosity that the flow over typical airfoils will not transition to turbulence, and the flow can be solved with direct simulation. Thus,  $10^3 < Re_c < 10^6$  is a transitional region for airfoils and wings. It is the region where laminar, transitional and turbulent flow all have a significant effect on the forces generated by the wing, and each must be modeled accurately.

## 1.2 Nomenclature

Throughout this paper, the  $Re$  based on the chord ( $c$ ), typically denoted  $Re_c$ , will simply be referred to as the  $Re$ . The chord line of a wing is the line that connects the trailing edge to the leading edge. The angle that this line makes with the free-stream velocity is the geometric angle of incidence, and will be referred to as  $\alpha$  in this paper. The span

from wing-tip to wing-tip will be denoted  $b$ , and the aspect ratio ( $b/c$ ) will be referred to as  $A$ .

The stream-wise direction is  $x$ , the span-wise direction is  $y$ , and the direction perpendicular to both  $x$  and  $y$  (the vertical) is  $z$ . The velocity components in each of these three directions is  $(u, v, w)$ , respectively.

The lift ( $L$ ) and drag ( $D$ ) forces are in the  $y$  and  $x$  directions, and their coefficients are the forces normalized by the dynamic pressure ( $\frac{1}{2}\rho U_\infty^2$ ) multiplied by the projected area of the wing ( $S = cb$ ). These coefficients are denoted as  $C_L$  and  $C_D$  for finite aspect ratio wings, and  $C_l$  and  $C_d$  for 2D (infinite aspect ratio) wings. The coefficients are only functions of the shape of the wing, and the  $Re$ .

### 1.3 Low Reynolds Number Aerodynamics

The earliest rigorous study of aerodynamics within this range of  $Re$  was conducted by Schmitz during the 1930's. [33] Using a wind tunnel, he measured the forces generated by airfoils in the range  $2 \times 10^4 < Re < 2 \times 10^5$ . He focused his study on three airfoil shapes: a thin flat plate, a thin cambered plate, and a thick cambered airfoil (the N60). His studies showed that the thick cambered airfoil has a critical  $Re$  where the performance changes drastically. Figure 1.1 is a plot of his results for the N60 airfoil across a range of  $Re$ . In this plot, the lift coefficient ( $C_l$ ) and drag coefficient ( $C_d$ ) are called  $c_a$  and  $c_w$  (the German convention). Also, the plot only shows the maximum  $C_l$ , minimum  $C_d$ , and the maximum lift-to-drag ratio ( $C_l/C_d$ ). Above the critical  $Re$  range, the maximum  $C_l$  and maximum  $C_l/C_d$  is much higher than below, and the minimum  $C_d$  has the opposite trend. This critical  $Re$  range is similar to the transitional  $Re$  range described in section 1.1 for a flat plate boundary layer. When an airfoil is below its critical  $Re$  range, the flow is dominated by viscous forces and remains laminar over the

entire airfoil. Above this range, the flow will transition to turbulence somewhere on the airfoil.

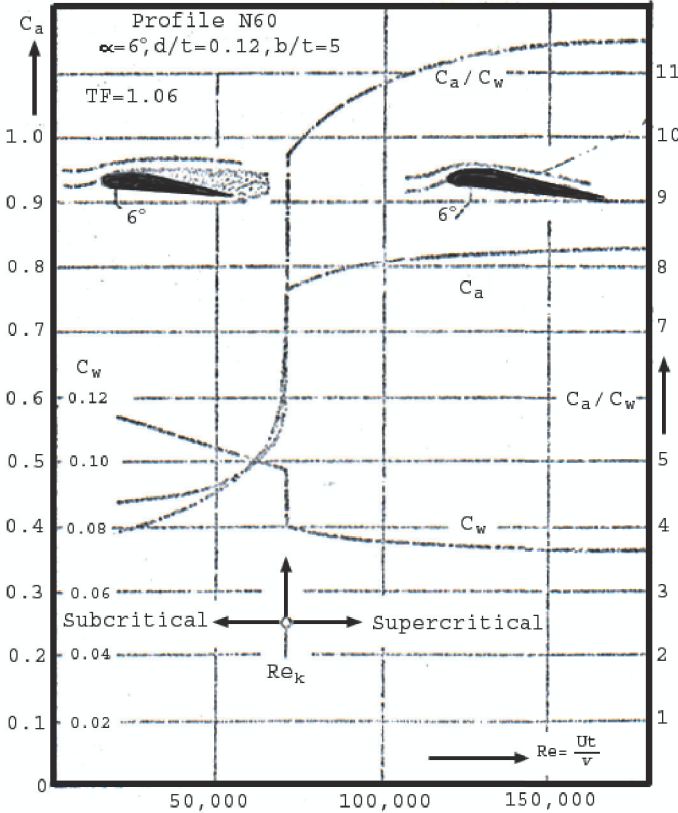


Figure 1.1: The critical  $Re$  (Schmitz)

The maximum lift coefficient, minimum drag coefficient, and maximum lift-to-drag ratio ( $C_a, C_w, C_a/C_w$ ) of the N60 airfoil is plotted against  $Re$  to demonstrate its critical  $Re$ . The sudden maximum lift increase and minimum drag decrease as  $Re$  increases past the critical value is related to the transition of the boundary layer on a flat plate. Here,  $Re$  is defined as  $Ut/\nu$ , where  $t$  is the German convention for the chord ( $c$ ) and  $\nu$  is the kinematic viscosity ( $\mu/\rho$ ). [33]

Over the next few decades, Schmitz’s results were verified and expanded upon by Abbott [2], Riegels [31], and Althaus [4]. For most airfoil sections, the critical Reynolds number is in the range  $10^4 - 10^6$ . [24] By plotting the lift-to-drag ratios of airfoils across

this range of Reynolds number, McMasters generalized these results in 1979 with a wide band as shown in figure 1.2.

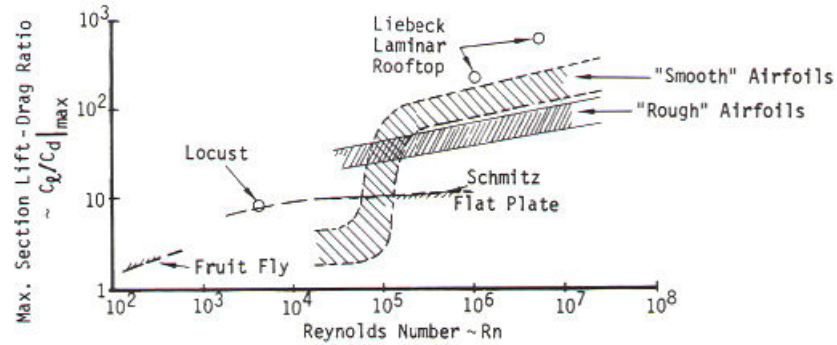


Figure 1.2: Maximum Lift-to-Drag vs Reynolds number (McMasters)

This plot is a generalization of the performance of many airfoils to qualitatively describe what happens as  $Re$  decreases. The data is taken from Jacobs and Sherman [14], Schmitz [33], Abbott and von Doenhoff [1], Riegels [31], Althaus [4], and Hoerner [13]. The figure was made by McMasters and is a summary of their data. [24]

McMasters' plot shows that, in general, smooth airfoils have a higher lift-to-drag ratio than rough airfoils at high  $Re$ . Thus, roughness causes a decrease in performance at  $Re$  above approximately  $10^5$ . However, below this  $Re$ , roughness is beneficial. Smooth airfoils have a large decrease in lift-to-drag ratio, while rough airfoils perform nearly as well as they did at the higher  $Re$ .

Building off this information, Mueller conducted both visualization and force measurement experiments to understand the cause for this performance decrease at low  $Re$ . [25] His studies focused on measuring the lift and drag forces on the NACA 66<sub>3</sub>-018 airfoil at  $4 \times 10^4 < Re < 4 \times 10^5$ . This is a symmetric airfoil that is 18% thick. Due to the limitations of his force balance (minimum resolvable force of 10 mN), the drag force measurements were only made at  $Re > 1 \times 10^5$ . The lift measurements made at  $Re = 4 \times 10^4$  show a dramatic change at  $\alpha \approx 8$  deg, as shown in figure 1.3(a). At  $Re > 10^5$  however, the lift coefficient was found to increase linearly with  $\alpha$ . Using smoke

visualization, Mueller showed that the drastic increase in lift coefficient found at  $Re = 4 \times 10^4$  and  $\alpha \approx 8$  deg is due to the formation of a Laminar Separation Bubble at that angle of attack. This bubble will be described in section 1.4, but for now it is sufficient to note that this measurement is made at  $Re = 4 \times 10^4$ , which is in the range indicated by the McMasters plot as a region where smooth airfoils experience a decrease in performance. It seems likely that the decrease in performance as  $Re$  decreases explained by McMasters is related in some way to the formation of the discontinuity in the lift vs angle of attack plot shown by Mueller.

This finding by Mueller should not be interpreted to contradict the results of Schmitz and the others plotted in McMaster's generalization. Instead, it is a more detailed understanding of how the forces generated by an airfoil change as  $Re$  enters the critical  $Re$  of the airfoil. For the same airfoil, Mueller measured the lift coefficient at  $Re = 4 \times 10^5$ , and that is shown in figure 1.3(b). The maximum lift coefficient is much higher at this larger  $Re$  than at the lower  $Re$  of  $4 \times 10^4$ , consistent with the previous findings.

Another series of extensive airfoil studies at low  $Re$  was conducted by Selig starting in 1986 at Princeton University. In this study, lift and drag were measured for 60 airfoils primarily at  $6 \times 10^4 < Re < 3 \times 10^5$ . [34] The lift was measured directly using a strain-gauge force balance, while the drag was estimated by the wake deficit measured by a pitot tube traversed vertically through the wake. The experiments were primarily concerned with improving the endurance and range of sail planes (non-powered, human-carrying airplanes) that operate in this range of  $Re$ .

The data obtained in this study showed that at  $Re > 1 \times 10^5$ , each airfoil has a drag polar that is qualitatively similar to drag polars at all higher  $Re$ . That is, the drag coefficient is low for a large range of lift coefficients. However, as  $Re$  decreases below this number, many of the airfoils have a significant increase in drag coefficient at moderate lift coefficients, while the drag coefficient at low and high lift coefficients is relatively

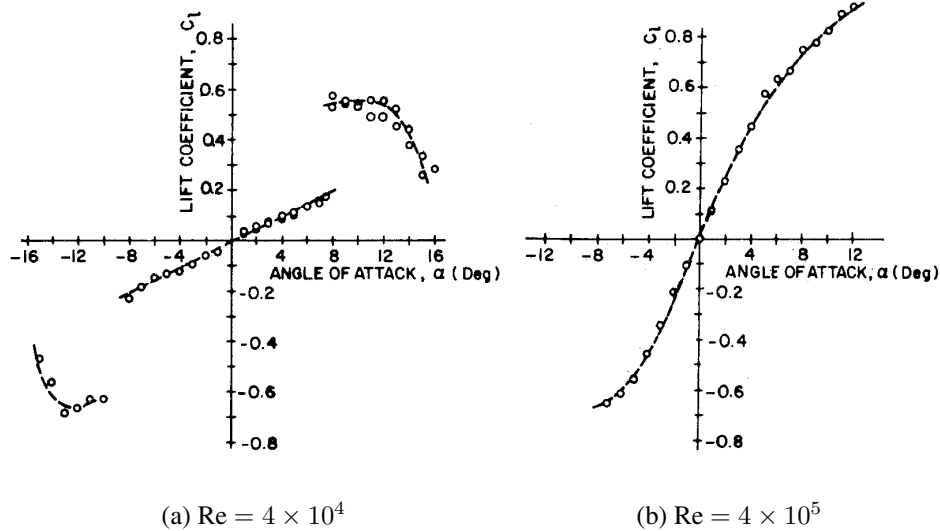


Figure 1.3: Lift curves for NACA 66<sub>3</sub>-018 airfoil (Mueller)

End plates were used to measure 2D airfoil performance. The sudden increase in lift at  $\alpha \approx 8^\circ$  and  $Re = 4 \times 10^4$  might be related to the change in performance indicated in figure 1.2. In this range of  $Re$ , the maximum  $C_l$  increases as  $Re$  increases, consistent with the findings of Schmitz. [25]

low. This is seen in figure 1.4, where the drag polar for the Eppler 387 (E387) airfoil, as measured by various facilities, is plotted across a range of  $Re$ .

The plot in figure 1.4 is a collection of results from various references, assembled into one plot for ease of comparison. The E387 airfoil is chosen for comparisons because it has been studied by more researchers at these  $Re$  than other airfoils. It is also a championship airfoil at sail plane competitions. It was designed by Richard Eppler and has a high maximum lift-to-drag ratio at  $Re \approx 5 \times 10^5$ . [37]

The two most interesting features of figure 1.4 are that there is more disagreement at the lowest  $Re$  and that, despite this disagreement, there is a consistent, qualitative change in the shape of the curve at the lowest  $Re$ . At  $6 \times 10^4 < Re < 3 \times 10^5$ , the drag polars for this airfoil are qualitatively similar to the other airfoils in this study in that the minimum drag coefficient steadily increases as  $Re$  decreases. The drag coefficient increase

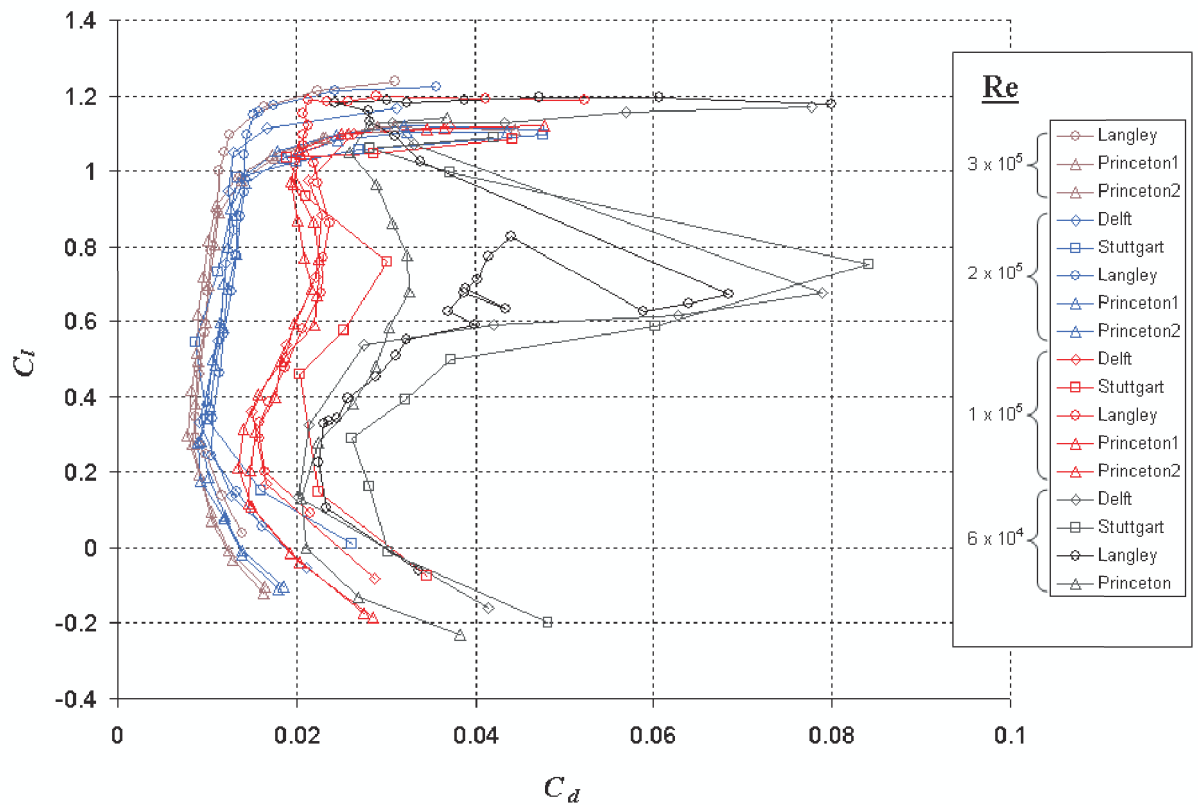


Figure 1.4: Drag polar of Eppler 387 airfoil at various  $Re$

The drag polar of the E387 airfoil at  $6 \times 10^4 < Re < 3 \times 10^5$  has been measured by different facilities. The shape of the E387 airfoil is shown here as well. This is a collection of results from many sources that has been digitized and re-plotted here. [34] [35] [3] [22] [42]

at moderate lift coefficients seen at  $Re = 6 \times 10^4$  was primarily found only for thick, cambered airfoils, similar to the E387. A comparison of drag polars obtained at different facilities, like figure 1.4, shows that data obtained at the lowest  $Re$  are less repeatable than data obtained at higher  $Re$ . This is true for 3 main reasons. 1) The forces measured here are much smaller than the higher  $Re$ , thus the relative uncertainty in the measurement is much higher. 2) The forces generated are much more sensitive to free-stream turbulence, surface roughness, and model geometry. 3) Different measurement techniques can return different results. Determining which explanation is most important

is difficult, especially since none of the facilities report their measurement uncertainty. Reporting the measurement uncertainty can eliminate explanation 1 as being a dominant factor, but literature results are often reported without measurement uncertainties. Without the uncertainties, the significance of the disagreement cannot be determined.

Explanation 2 is typically assumed to be the most important factor in explaining the large disagreements. It is known that free-stream turbulence above 0.1% of the free-stream effects the transition process of a flat-plate boundary layer. [32] Also, the relative length of the transition region (relative to the chord length) increases as the chord-based  $Re$  of the airfoil approaches the critical  $Re$ . Thus, the effect of the transition region is more significant as the  $Re$  approaches the critical  $Re$ . Thus, when comparing experiments with different turbulence levels, the effect will show up in the experiments conducted at  $Re$  closer to the critical  $Re$  range of the airfoil. For the E387, the critical  $Re$  range has not been identified, but it is assumed to be around  $6 \times 10^4$ .

The final explanation is often discussed in the literature as well, but it is generally not considered to be as important as explanation 2. There are primarily two ways to measure the drag of an airfoil: directly with a force balance, or indirectly by measuring the wake and estimating the force using the conservation of momentum. The difference between the two is that the wake can only be measured at discrete points along the span, and then there must be some assumption about the points that are not measured in order to get an estimate of the drag of the whole wing. However, at  $Re \approx 10^5$ , Selig et al showed that the wake is highly three-dimensional and it has much span-wise variation. [36] Figure 1.5 shows the wake deficit measured at different spanwise locations by Selig et al. The measurement shows the considerable spanwise variation described above, and this is at a relatively low angle of attack, and higher  $Re$  than the  $6 \times 10^4$  case. No data is supplied for lower  $Re$ , but the variations most likely increase with decreasing  $Re$ .

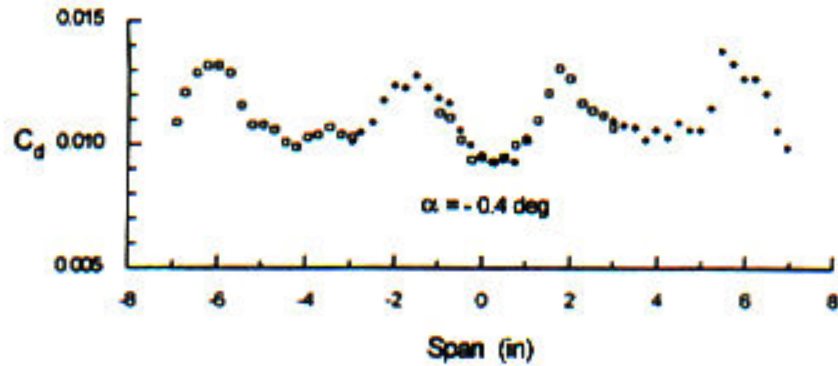


Figure 1.5: Spanwise variation of the wake (Selig)

Wake deficit drag coefficient estimate plotted against the spanwise location of the wake measurement. This is for the Eppler 374 airfoil at  $\alpha = -0.4^\circ$  and  $Re = 2 \times 10^5$ . [36]

Thus, many measurements of the wake would need to be made across the span to measure the drag of the wing accurately. At first, it would seem the direct force balance method would be obviously better than the indirect wake measurement method. However, when measuring airfoil performance experimentally, one must typically use end plates at the wing-tips of a finite span model. Pelletier and Mueller found that at low  $Re$ , these end plates cause significant changes in the forces generated when compared with a true 2D airfoil. [29] Figure 1.6 shows the drag coefficient plotted against Reynolds number for the Eppler 61 airfoil at  $\alpha = 0^\circ$ . The “3-piece airfoil” is a much better approximation of a true 2D airfoil than the other cases plotted. The data by Althaus [3] and de Vries et al was taken using a wake measurement at the center-plane of the airfoil with end plates. Pelletier and Mueller found that end plates cause a 15% increase in drag and a 30% decrease in lift across this range of  $Re$ . The data also indicate that without sufficient sampling of the wake across the span, wake deficit measurements can yield unreliable drag estimates at this range of  $Re$ .

At sufficiently high  $Re$ , these two techniques yield very similar results, and compare well to computational results. Thus, using either of these techniques for airfoil force

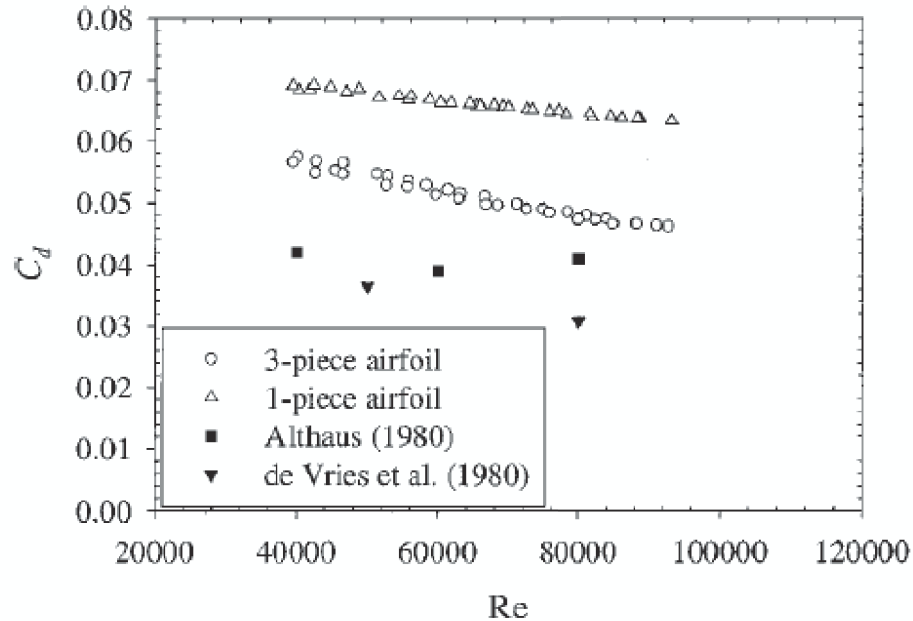


Figure 1.6: Effect of end plates on force balance measurements (Mueller)

The drag coefficient of the E61 airfoil at  $\alpha = 0^\circ$  as measured directly with a force balance by Mueller et al is plotted against the Re. The “3-piece airfoil” does not have end plate effects, and is therefore a much better approximation of a 2D airfoil while the “1-piece airfoil” has end plates at the wing tip. The Althaus [3] and de Vries et al data were obtained by wake deficit measurements in the center of the wing with end plates used. It appears that end plates cause a systematic increase in measured drag, and that wake deficit measurements may yield incorrect drag estimates at these Re due to the 3-dimensional nature of the wake demonstrated by Selig et al [36]. [29]

measurements is adequate at high Re. At Re in the current range of interest, neither technique is fully correct. However, the direct force measurement seems to have a systematic correction across all Re, while the indirect wake measurement method has no method of estimating possible errors.

Using a highly sensitive force balance, Laitone acquired some of the most reliable data on forces generated by low Re wings. [16] In fact, he claimed that his data is the first and only reliable force measurements at  $Re < 10^5$  because his force balance has an uncertainty of  $\pm 0.1$  mN while Schmitz’s was  $\pm 1$  mN and Mueller’s was  $\pm 10$  mN. In

addition, Laitone's wind tunnel had much lower turbulence levels ( $\approx 0.02\%$ ). Laitone measured the lift and drag of a thin wedge (which approximated a flat plate), a 5% cambered plate, and the NACA 0012 at angles of attack from zero lift to well beyond stall. The range of  $Re$  was  $2 \times 10^4 - 7 \times 10^4$  and he demonstrated a variety of results that are peculiar to this range of  $Re$ . The first is that at  $Re \approx 2 \times 10^4$ , the 5% cambered plate achieves the highest lift-to-drag ratio, while the NACA 0012 had the lowest, even lower than a simple thin wedge. This is shown in figure 1.7. In addition to these peculiar findings, figure 1.8 shows that the NACA 0012 has a higher lift coefficient when it is placed backwards in the flow, that is, when the trailing edge is used as the leading edge. These results indicate that a small leading edge radius is preferred at this range of  $Re$ .

He also found that a moderate increase of free-stream turbulence from 0.02% to 0.1% causes the NACA 0012 airfoil to have higher lift coefficients and higher lift-to-drag ratios. Much larger increases in free-stream turbulence (near the values in Schmitz's wind tunnel) cause the NACA 0012 to have much lower lift coefficients and lift-to-drag ratios. His overall conclusion is that at  $Re < 5 \times 10^5$ , potential flow theories do not apply because, the measured lift curve slopes at these  $Re$  are 20% larger than those predicted by Prandtl's lifting line theory. In addition, the induced drag coefficient is dependent on airfoil shape and  $Re$ .

Experiments at  $Re < 5 \times 10^5$  were also conducted by Grundy et al. [11] They measured the forces of the thin, cambered Eppler 61 airfoil (5% thick, 5% camber) at  $Re = 2.5, 3.5, 5, \text{ and } 6 \times 10^4$ . The tests were conducted in a wind tunnel with turbulence levels of 0.1% - 0.3%. Considering that Schubauer and Skramstad found the flat plate transition  $Re$  to be effected by free-stream turbulence levels of 0.1% and higher [32], the measurements of Grundy et al are likely to be effected by the turbulence level in their wind tunnel. In addition, the force balance used is rather insensitive in comparison with

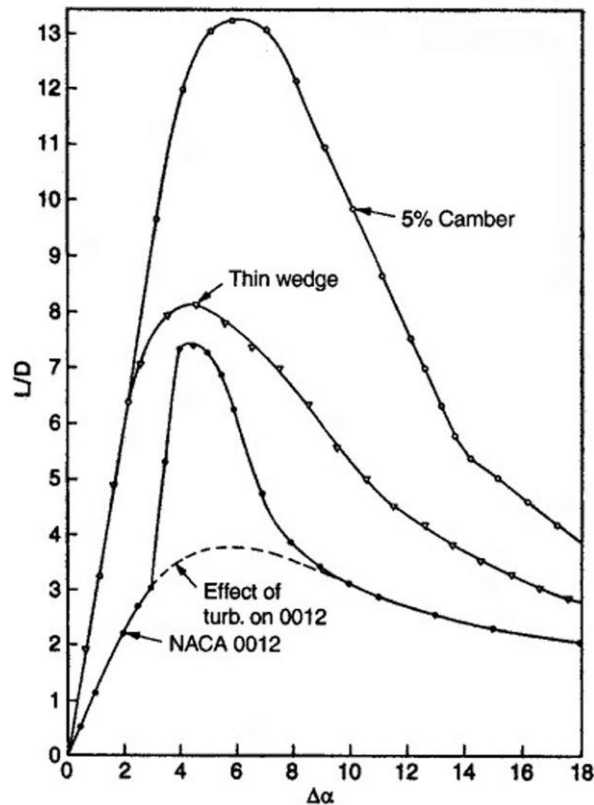


Figure 1.7: Lift to Drag ratio for three airfoil shapes (Laitone)

Data is taken for a thin-wedge (which approximates a flat-plate), a cambered plate, and the NACA 0012 airfoil at  $Re \approx 2 \times 10^4$ . The dashed line indicates the effect of a large increase in free-stream turbulence (close to the value present in Schmitz's experiments) on the NACA 0012 airfoil. [16]

that used by Laitone. Grundy et al used a force balance with a resolution of  $\pm 1$  mN while Laitone's was  $\pm 0.1$  mN.

Despite these possible limitations, Grundy et al were able to find similarity between their force measurements and measurements made at Stuttgart, Delft and Notre Dame. They found the drag coefficient increases at moderate lift coefficients (similar to that shown above for the E387 airfoil), and their values of drag and lift coefficients were within reasonable agreement with previous measurements. They also measured a large

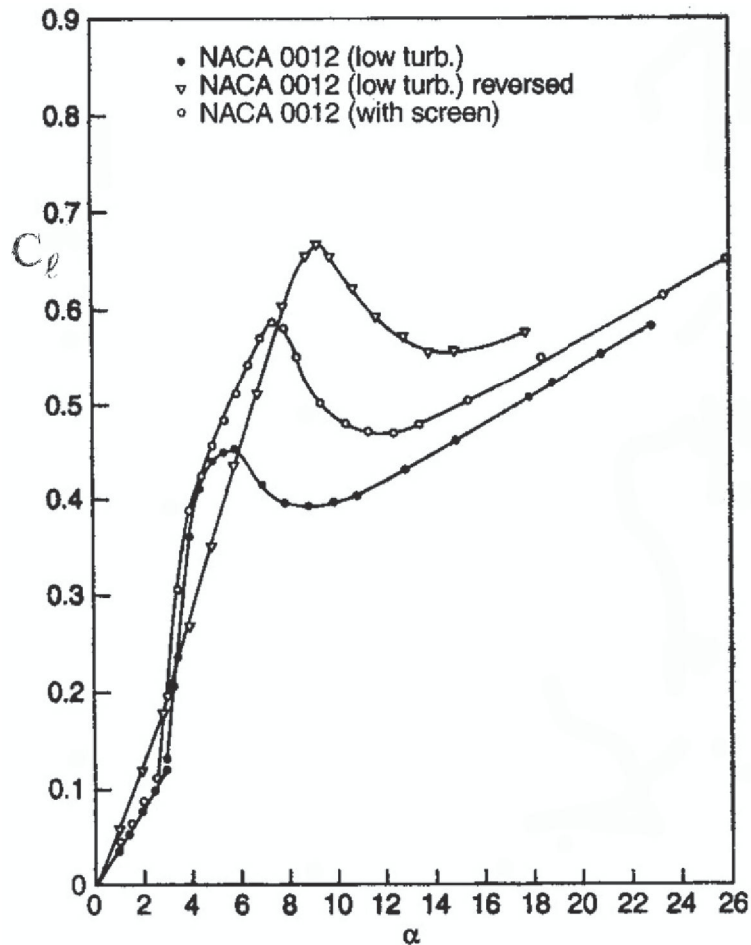


Figure 1.8: Lift curve for NACA 0012 in various conditions (Laitone)  
 The lift coefficient vs angle of attack at  $Re \approx 2 \times 10^4$  shows that free-stream turbulence can have a significant effect on the forces. Also, the sharp leading edge produced by turning the airfoil around has a beneficial effect. The “low turb” case is at 0.02% turbulent while the “with screen” case is at 0.10% turbulence. [16]

degree of hysteresis in their force measurements depending on whether  $\alpha$  was increasing or decreasing. This hysteresis depended on the noise levels present in the wind tunnel, and this was the focus of their studies, to measure the effect of single frequency acoustic disturbances on force generation from wings at these low  $Re$ . It was found that certain frequencies of acoustic excitation in the wind tunnel would cause a decrease in hysteresis.

One unexpected result of the research was in finding an additional explanation for the large discrepancy between measurements made at different facilities. Not only must the different turbulence values be accounted for, but also the different resonant frequencies of the wind tunnels. The work of Grundy et al showed that since airfoil performance at  $2 \times 10^4 < Re < 6 \times 10^4$  is dependent on acoustic excitation, and since each wind tunnel resonates at a different frequency, it is quite likely that different wind tunnels will measure different performance in this range of Re, simply because of the different resonant frequencies..

Experiments conducted by Pelletier and Mueller measured both 2D airfoil performance as well as the performance of 3D rectangular planform wings.[28] They used a wind tunnel with a turbulence level of 0.05% and measured forces generated by a thin flat-plate wing (1.3% thick, 0% camber) and a thin cambered-plate wing (1.3% thick, 4% camber) at  $6 \times 10^4 < Re < 2 \times 10^5$ . They used end plates to measure approximate 2D conditions, and removed one of the end plates to measure approximate 3D conditions. Force measurements were made using a strain gauge force balance with a minimum measurable load of 10 mN, similar to Mueller's previous work in 1982. One of the results of this study was that, unlike the study by Grundy et al, no hysteresis was found. It is not clear whether this is caused by the decreased thickness of the wings, or by the decreased turbulence levels in the free-stream. Also, in contrast to the results of Laitone, potential flow theory seems to adequately predict the lift curve slope for the 3D wings studied at these Re.

## **1.4 Laminar Separation Bubble**

The most common explanation for the unusual behavior of airfoils and wings at these low Re ( $10^4 < Re < 10^5$ ) is the existence of a laminar separation bubble (LSB) at

certain  $\alpha$ . Selig claims that the LSB causes the peculiar drag increase at moderate lift coefficients. Grundy et al explain the hysteresis in their polars, and the large sensitivity to single frequency sound waves, on the LSB. And finally, Pelletier and Mueller state that the lack of hysteresis in their data is related to the lack of an LSB.

An LSB is demonstrated in figure 1.9. It typically begins with a laminar boundary layer that encounters an adverse pressure gradient, which causes the boundary layer to separate. The laminar separated shear flow is unstable and transitions to a turbulent separated shear flow. The turbulence then transports momentum from the free-stream, across the shear layer, and down towards the surface. When the momentum transport is sufficient, the turbulent boundary layer is considered to be reattached to the surface, thus closing the separation bubble.[19]

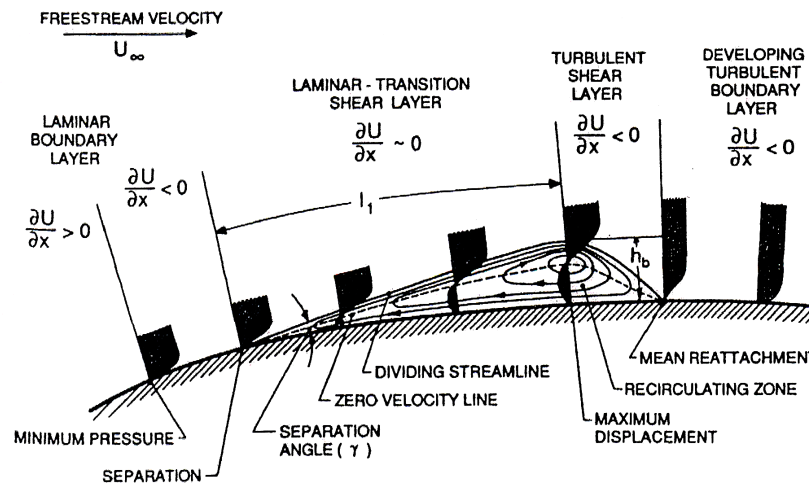


Figure 1.9: Description of a laminar separation bubble. (Mueller)

The boundary layer is initially laminar, and separates just after the point of minimum pressure. The separated shear layer is much more unstable than an attached boundary layer and will transition to turbulence more quickly. Turbulent flows are able to transport momentum across the mean flow, and turbulent reattachment occurs downstream of the transition point. [6]

According to Selig et al, this LSB is responsible for the drag coefficient increase at moderate lift coefficients when the Eppler 387 airfoil is at  $Re \approx 6 \times 10^4$  (see figure 1.4). He states on page 54 of Airfoils at Low Speed [34] that “The effects of a laminar separation bubble are apparent only at an  $Re$  of 60k through the mid-lift range, where the drag coefficient reaches a maximum of 0.032 at a [lift coefficient] of 0.5”. Selig et al call this drag increase the “bubble drag” because they believe it is caused by the LSB. [20] However, none of his studies at that time had investigated the boundary layer of the airfoils tested, and thus no direct evidence of this conclusion can be found.

Later tests by Selig et al used surface oil flow visualization techniques to discern the existence and size of the LSB. [20] [37] This technique is used to visualize the time-averaged flow properties near the surface. With it, one can distinguish steady-state laminar and turbulent flow regions, separation/reattachment points, and the transition regions of a boundary layer. The tests conducted clearly show that there is a laminar separation point, and that there is a turbulent reattachment point. However, data were only shown for the relatively high  $Re$  of  $2 \times 10^5$  and  $3 \times 10^5$ . [37] The drag polar of the airfoil at these  $Re$  have much smaller drag increase at moderate lift coefficients (see figure 1.4). The “bubble drag” is only discernable for  $Re \leq 1 \times 10^5$ , an  $Re$  at which surface oil flow visualization is not available.

Selig et al claim that the LSB is responsible for the drag coefficient increase at moderate lift coefficients. However, there were no flow field measurements of the boundary layer to support such findings, only surface oil flow visualizations. Further, there were no flow measurements at all for the airfoil at  $Re \leq 1 \times 10^5$ , where the drag increase is most apparent.

A detailed review of the literature shows that there is no other support for this interpretation of the “bubble drag” either. Grundy et al claim that the increase in drag at moderate lift coefficients is associated with a “long separation bubble”, while the decrease

in drag as lift increases is associated with a transition in the flow from a long separation bubble to a short separation bubble. No measurements of the boundary layer are presented to support this claim. [11]

Laitone makes no mention of an LSB in his experiments on a flat plate, a cambered plate, and the NACA0012 airfoil at  $2 \times 10^4 < Re < 7 \times 10^4$ . [16] Meanwhile, Pelletier and Mueller find no LSB in their experiments on thin flat and cambered plates at  $6 \times 10^4 < Re < 2 \times 10^5$ . Using hydrogen bubbles in a water channel, they found that at all angles of attack there was no reattachment after the laminar separation. This seems to explain the lack of hysteresis found in their results, and the lack of drag increase at moderate lift coefficients. [28] However, there is still limited evidence to support the theory that the LSB actually causes the hysteresis or the drag increase at moderate lift coefficients.

Many other studies have focused on understanding the LSB, but each is limited by one of the following. Many of them do not study the effect of the LSB on the forces generated by the wing, many are often limited to a very small range of  $\alpha$ , some of them investigate conditions where there is no drag increase at moderate lift coefficients, and some study geometries that have little significance to practical flying vehicles.

Arena and Mueller studied the LSB formed by an airfoil with a cylindrical leading edge, followed by a constant thickness section, followed by a linearly tapered trailing edge. The LSB formed near the leading edge, just after the cylindrical section, and was measured by use of pressure taps on the upper surface, surface oil flow visualization, and smoke visualization. The study looked at  $-4^\circ < \alpha < 6^\circ$ , and  $1.5 \times 10^5 < Re < 4.5 \times 10^5$ . [5] This study showed that as  $Re$  decreases across this range, the LSB increases in size from approximately 10% of the chord, to nearly 20%. As angle of incidence increases, the bubble also increases in size. They also point out the inherent

difficulties in measuring the location and size of the unsteady bubble. The use of time-average techniques may be inappropriate, and averages of instantaneous measurements may be skewed due to inadequate sampling. These topics were not discussed in their reports of the experiments.

Broeren and Bragg conducted detailed studies of the LSB at low Re and related the LSB to the stall type. [7] At  $Re = 3 \times 10^5$ , they measured the time-dependent growth and decay of the LSB on the upper surface of the LRN(1)-1007 airfoil at  $\alpha = 15^\circ$ . The measurements were made using 2-component Laser Doppler Anemometry, with measurements made within 0.2 mm of the surface. The airfoil at this angle of incidence is  $2^\circ$  below the stall angle, and there are very large fluctuations in the forces generated at this angle of attack. By measuring the flow field around the wing, they found a time periodic nature of the LSB: the LSB started small, then grew until it reached the trailing edge causing full separation, then suddenly became small again.

In a later paper, they relate this growth to the force fluctuations, and show that the dominant frequency of the fluctuating LSB is the same as that of the fluctuating lift force. [8] They also classified airfoils at this Re as having 5 common types of stall, and that each stall type was associated with a different amount of lift fluctuation near stall. The 5 stall types are: Trailing Edge, Leading Edge, Trailing Edge/Leading Edge, Thin Airfoil, and Thin Airfoil/Trailing Edge. The last two have an LSB that in some way causes the stall, either by growing until it reaches the trailing edge, or by growing until it reaches the point of trailing edge separation. These types of stall have the highest lift fluctuations near stall, with the combination Thin Airfoil/Trailing Edge stall having higher lift fluctuations than the pure Thin Airfoil stall.

A detailed comparison between time-averaged measurements of an LSB was done by Ol et al. [27] Experiments were performed at 3 facilities: a water-filled tow tank at the Institute for Aerospace Research, a wind tunnel at the Technical University of

Braunschweig, and a water channel at the Air Force Research Lab. Each facility used PIV to measure the flow field around the SD7003 airfoil at  $\alpha = 4^\circ$  and  $Re = 6 \times 10^4$ . The resolution of the PIV system was adequate to resolve the boundary layer, and hence the LSB that is present at this angle of incidence. While there is an LSB for this airfoil at these conditions, and while it is at an  $Re < 10^5$ , the drag polar of the SD7003 has no characteristic "bubble drag" such as the E387 shown in figure 1.4. The drag polar of this airfoil, as found reported by Selig et al [35], is shown in figure 1.10 at various  $Re$ , including the one investigated by Ol et al. It seems that the LSB measured by Ol et al does not cause a drag increase at moderate lift coefficients. Thus the separation bubble is having very little effect on the shape of the drag polar of the airfoil, and may not be the explanation for the drag increase at moderate lift coefficients found for the E387 at  $Re = 6 \times 10^4$ .

While good agreement in LSB size and location was found between the facilities compared by Ol et al, measurements were only made at one angle of incidence and one  $Re$ . This yields little insight on how the bubble grows. Also, no force measurements were made, and it is not clear how the LSB effects the forces generated by the airfoil.

Computational techniques are also being used to investigate the LSB at low  $Re$ . In the above study by Ol et al, they compared Xfoil results to their measurements of the LSB. Xfoil computes the flow around an airfoil by first computing the potential flow on a grid around the airfoil using a panel method, then it solves the boundary layer equations at points along the airfoil. The largest positive amplification rate of waves for each boundary layer profile is calculated and integrated along the surface. The integration of the amplification rates (referred to as the N-value) has been experimentally correlated to the point of transition to turbulence, and there is a critical N-value at which transition to turbulence occurs. For most cases, the critical N-value is 9. Thus, with some assumptions and some correlations, one can compute the external flow, the boundary

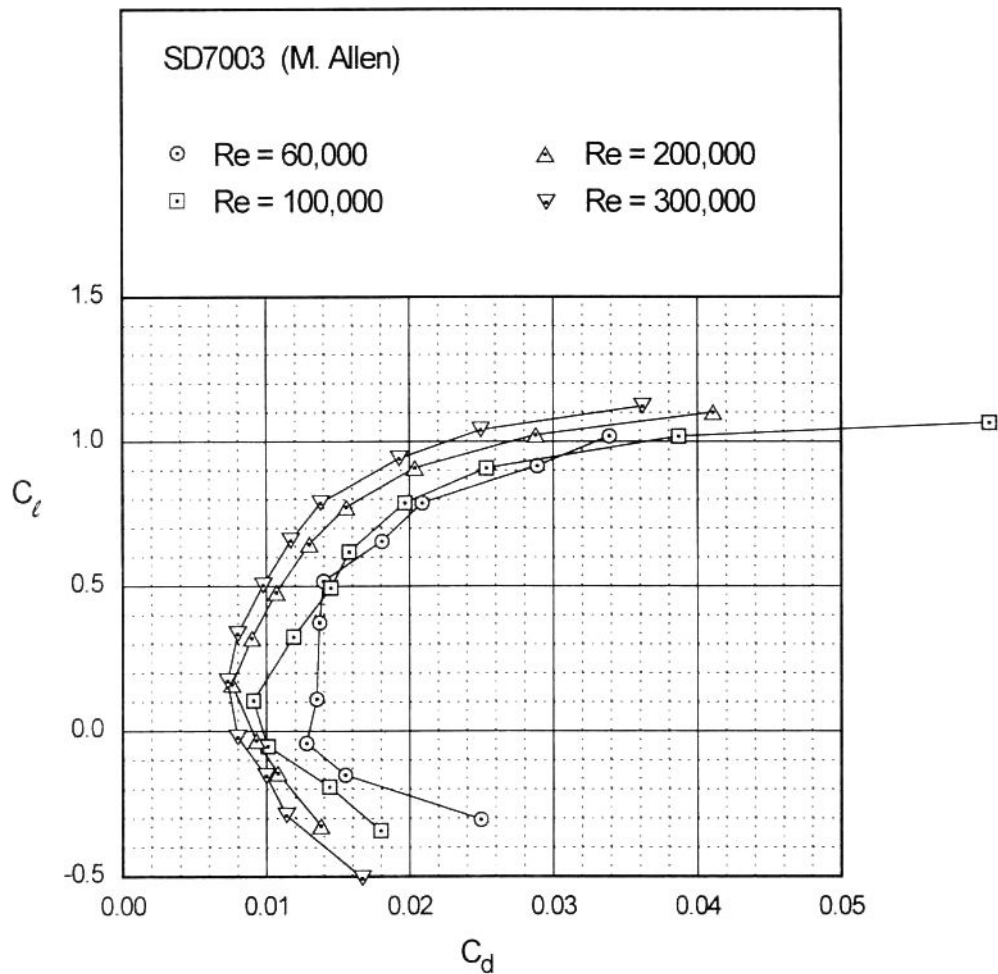


Figure 1.10: Drag polar of a SD7003 airfoil at various Re. (Selig)

The drag polar at the lowest Re shows no sign of the so called “bubble drag” which should cause a dramatic drag increase at moderate lift coefficients. [35]

layer profile along the surface, and the transition to turbulence. After transition, turbulence models can be used to model the flow.

Since Xfoil only computes the flow near the surface and the forces on the wing, the recirculating flow cannot be verified by plotting velocity fields. However, by plotting the local skin friction coefficient of the wing, Xfoil can indicate a region of reverse

flow, which would identify the location of an LSB. This is shown in figure 1.11 as a plot of skin friction vs location along the upper surface of the SD7003 airfoil. Laminar separation occurs when the skin friction becomes negative, and turbulent reattachment occurs when it becomes positive again.

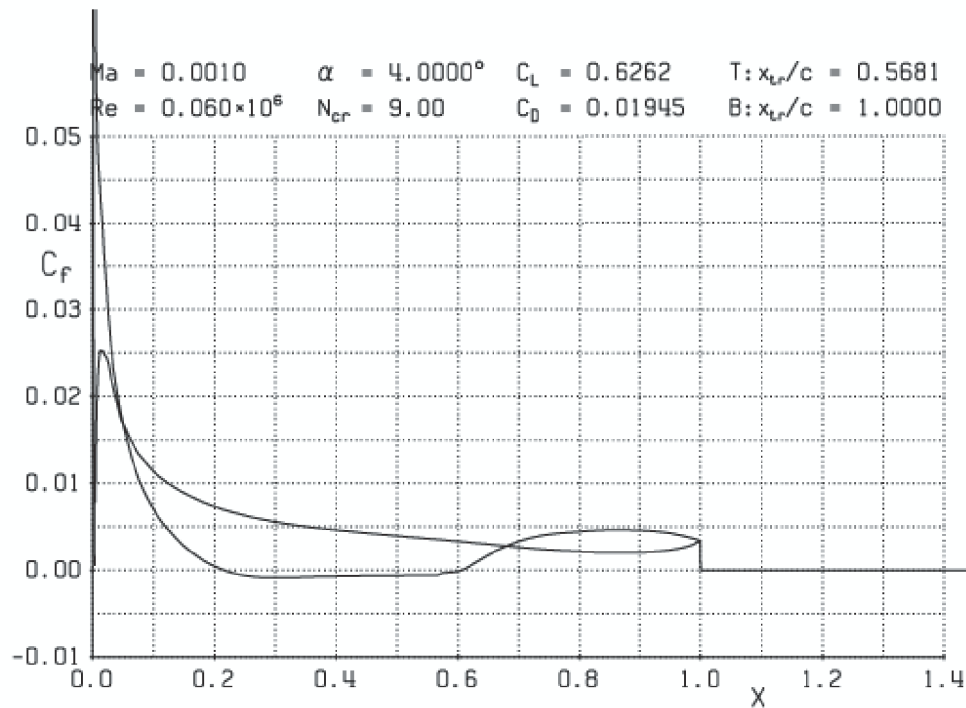


Figure 1.11: The laminar separation bubble for the SD7003 airfoil (OI)

A plot of skin friction coefficient vs chord-wise location for the SD7003 at  $Re = 6 \times 10^4$  and  $\alpha = 4^\circ$  is used to measure the length of the bubble. This result is from Xfoil using a critical N-value of 9. The location of the LSB is indicated by the region where the skin friction coefficient is negative. [27]

The results of Xfoil showed an LSB at approximately the same location as the measurements, but no quantitative uncertainty analysis was made and it is unclear how accurate the Xfoil results will be in various other cases. In addition, since Xfoil does not calculate flow fields, no comparisons of circulations or bubble height could be made.[27]

In a study by Mohseni et al, the computation of the flow field around an aspect ratio 1.2 flying-wing airplane at  $Re = 1.4 \times 10^5$  using an E387 airfoil was also able to calculate the presence of an LSB. [12] The 3-dimensional computation used a direct numeric simulation of the Navier-Stokes equations, and makes no mention of any transition or turbulence models. At this  $Re$ , it is unclear whether the computation they describe has the spatial and temporal resolution to capture the transition to turbulence. There is no comparison with measurements made on a similar configuration, but they did compare computed force on a flat plate at various  $\alpha$  to measurements made by Mueller et al. As shown in figure 1.12, the computational results were not in good agreement with the measurements. This questions the validity of the computational technique, and the LSB computed by it. Furthermore, the  $Re$  of this computation is well above that shown to be the  $Re$  that causes the drag increase at moderate lift coefficients.

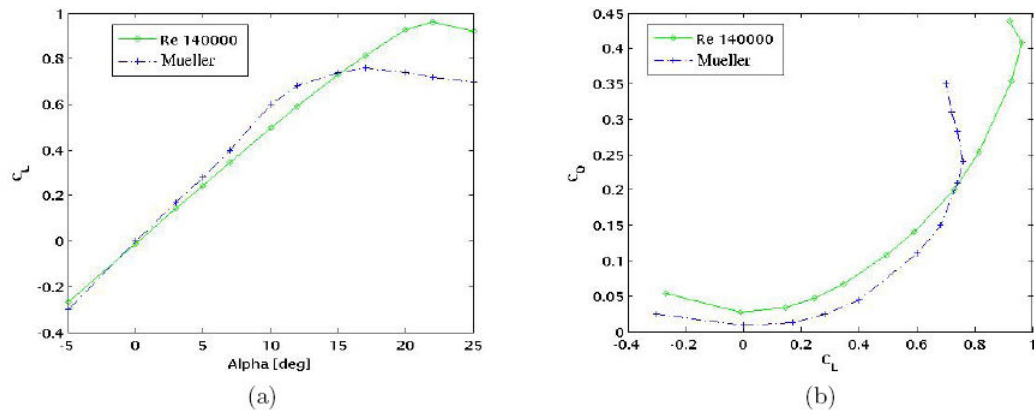


Figure 1.12: Lift and drag of a flat plate airfoil (Mohseni)

The forces from computational results of Mohseni et al are compared with the experimental measurements of Mueller et al for a flat plate at  $Re = 1.4 \times 10^5$ . The disagreement here is substantial, with the maximum lift being more than 20% greater and the minimum drag being more than 50% greater than the experimental measurements. [12]

Finally, in a study by Radespiel et al, a computational technique based on linear stability theory of boundary layers was used to compute the LSB on a SD7003 airfoil at

$Re = 6 \times 10^4$ ,  $\alpha = 4^\circ, 8^\circ, 11^\circ$ , and in both steady and unsteady flow. The computational technique is similar to Xfoil in that it computes the external flow, the boundary-layer profile, and relies on a critical N-value to identify the location of transition to turbulence. The difference is that it uses an Unsteady Reynolds-Averaged Navier-Stokes (URANS) equation to compute the external and boundary layer flow rather than the panel-method and boundary layer equations used by Xfoil. Once the critical N-value has been reached, the URANS equation computes both the spatial and temporal growth of the turbulence from the point of transition, which is required for unsteady computations.

The computational results are compared with experimental measurements taken at the same conditions. The experimental measurements consisted of PIV measurements which resolved the boundary layer flow, and hence visualized the LSB. An example of the experiments and computations are shown in figure 1.13 where the experiments are labeled as WUB, and the rest are computational results with various turbulence models. The turbulence level in the experiments was 0.8%, 8 times as large as the turbulence level that effects the transition of a flat plate boundary layer. It is unclear whether computations should be compared with experimental results that have such large values of free-stream turbulence.

Streamlines are plotted along with the normalized turbulent shear, an indication of the turbulence intensity. The LSB can be seen as the region of recirculating flow, and the transition to turbulence seems to be caused by the shear layer of the LSB. The plots are for  $\alpha = 8^\circ$  and three types of turbulence models are used in the computations. The first two are developed by Menter and are called the baseline (BSL) and the baseline 2-layer (BSL-2L) models. The third is from Wallin and can be used for both compressible and incompressible turbulent boundary layers. For this application, it seems that the BSL models perform the best, and based on comparisons at other  $\alpha$  and using various other

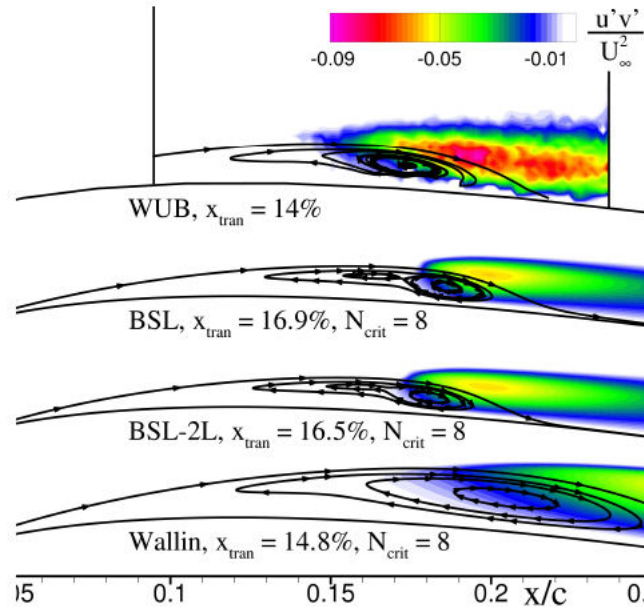


Figure 1.13: The laminar separation bubble on the SD7003 airfoil (Radespiel) Experimental and computational results at  $Re = 6 \times 10^4$  and  $\alpha = 8^\circ$  are compared. The WUB result is from PIV measurements in a water channel, and the other three are from computations with various turbulence models. Streamlines are indicated by lines with arrows, and turbulent shear is indicated by the color map. The transition point is listed in percentage of the chord, and the critical N-value is 8 for this comparison. [30]

critical N-values, Radespiel et al determine that the BSL-2L model is the most appropriate, although they point out that the computations are not completely satisfactory.

In addition to comparing the LSB computations to experimental measurements of the LSB, they also compared the forces computed to forces measured by Selig et al in [34] [35]. The comparison in figure 1.14 shows the lift coefficient plotted against  $\alpha$  and the drag coefficient. The open symbols are plotted against  $\alpha$  and the filled symbols are plotted against the drag coefficient. Despite the large differences in computed LSB size and shape, the forces computed by each of the turbulence models are quite similar and all are within the experiments conducted by Selig et al. Granted the experiments were conducted more than 5 years apart and at two different wind tunnel facilities, but this

comparison seems to indicate that while an LSB exists for this airfoil at this  $Re$  and  $\alpha$ , it does not seem to significantly affect the forces generated by the airfoil. This plot also indicates that a basic understanding of which drag polar is correct limits one's ability to validate a computational technique.

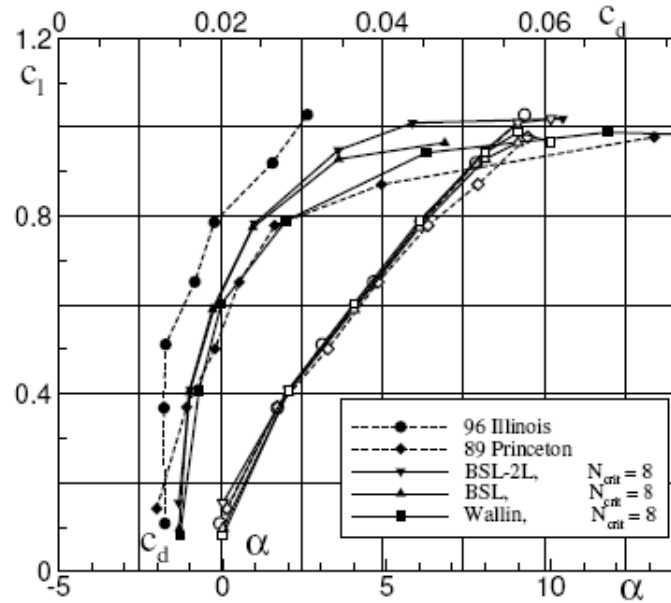


Figure 1.14: Drag polar for SD7003 airfoil. (Radespiel)

The experimentally measured results from Illinois and Princeton (dashed lines) are compared with the computational results of Radespiel et al (solid lines). The lift coefficient vs  $\alpha$  is shown in the open symbols while the filled circles are lift coefficient vs drag coefficient. The airfoil is at  $Re = 6 \times 10^4$ . [30]

## 1.5 Leading Edge Vortex

Another type of laminar separation followed by reattachment to the airfoil upper surface is a stable vortex over the wing. When this vortex occurs near the leading edge, it is often referred to as a leading edge vortex (LEV). An LEV is formed by separation at the sharp leading edge of a wing. The separation rolls up on top of the wing, and forms a

vortex near the leading edge. The flow outside the vortex is able to reattach to the airfoil surface. The vortex is stabilized by the span-wise flow from the wing root to the wing tip. This span-wise flow causes the vortex to form a helical shape as it travels down the span.

The LEV has historically been linked to small, flapping, biological, hovering fliers, such as flies and bees. The Reynolds number for these hovering systems is often defined as  $Re_\omega = \frac{\omega c^2}{\nu}$ , where  $\omega$  is the angular velocity of the wing,  $c$  is the maximum chord, and  $\nu$  is the kinematic viscosity. The first speculation of a vortex forming near the leading edge of a flapping wing was after observations of unusually high  $C_L$  values from flapping wing insects by Weis-Fogh. [43] He observed several species of insects and found that they “fling” their wings apart before downstroke. He believed this could cause a vortex to form and remain attached to the wing during downstroke.

Later studies by Maxworthy [21] and Spedding & Maxworthy [38] verified that there was increased lift due to the “fling” mechanism theorized by Weis-Fogh. Using a dynamically scaled model and flow measurements, Maxworthy demonstrated the vortex formed during the fling process and maintained during the subsequent downstroke of the wing. [21] These measurements were made at  $Re_\omega = 32$  (similar to insect flight) and  $1.3 \times 10^4$  (to test inviscid theories). In figure 1.15, the 3-dimensional wing is in the downstroke phase of motion, and the vortex has a helical shape, starting near the wing root and extending outboard to the wing tip. Studies by Spedding & Maxworthy used a 2-dimensional apparatus with flow and force measurement to demonstrate the increased lift provided by the “fling” mechanism. [38]

Many subsequent studies on biological flying systems (especially insects) have revealed that a dominant feature of the flow physics of a flapping wing at low  $Re$  is the formation of an LEV. Ellington et al used a mechanical flapper to illustrate the formation of an LEV on the wing of a hawkmoth and differentiated the effects of rotation

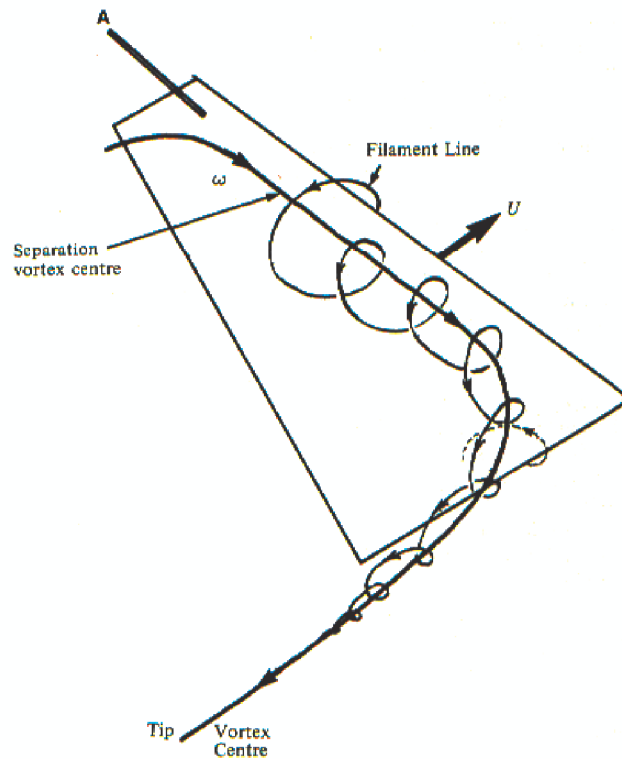


Figure 1.15: The vortex formed near the leading edge (Maxworthy)

The wing is rotating from left to right around point A with some angle of attack. This rotation causes each section of the wing to move with a different velocity. Separation occurs at the leading edge, and spanwise flow transports the vorticity to the wing tip before it can accumulate and shed into the wake. This vorticity is the LEV. At the wing tip, the LEV joins with the trailing wing-tip vortex. [21]

for delayed stall, and the subsequent downstroke that uses the LEV. [40] An image from their results is shown in figure 1.16, and it illustrates the wing location, the vortex that grows from the wing root to the wing tip, and the wing tip vortex that it merges with.

Srygley and Thomas found a slight difference in the form of the LEV present on red admiral butterflies. Previously, the vortex was believed to form on either side of the insect body, and grow toward the wing tip. However, evidence in their study suggests that the LEV extends across the body, as shown in figure 1.17. [39]

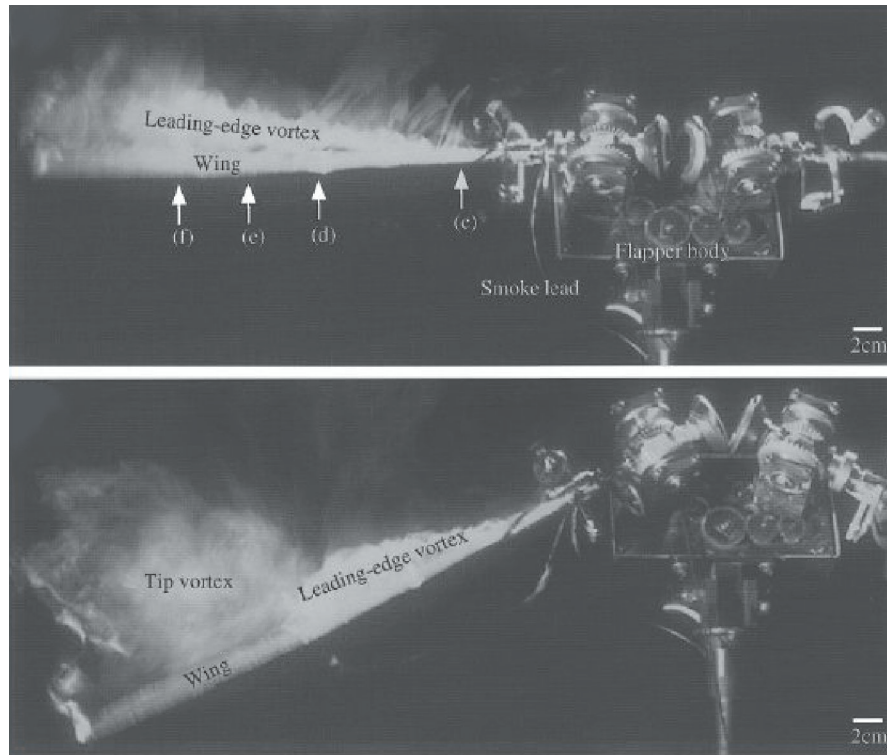


Figure 1.16: The vortex formed by a model hawkmoth (Van Den Berg) These images of a mechanism designed to mimic the motion of a hawkmoth illustrate the formation of the LEV during downstroke. Smoke is released from point c, near the root of the wing, at the beginning of downstroke. This smoke is transported along the span by the LEV, and can be seen in the upper image at mid-downstroke. The lower image is at the end of downstroke, and the LEV does not extend as far, as the wing-tip vortex has moved inboard. [40]

More recently, there have been studies that have measured an LEV on the fixed, swept wing of a Swift (a small bird). [41] [18] The first study at  $3.7 \times 10^3 < Re < 3.7 \times 10^4$  indicated that the  $60^\circ$  swept hand-wing of the Swift develops an LEV at an angle of attack of  $\alpha = 10^\circ$  and it was speculated that the LEV may cause an increase in lift. [41] The study was performed on a plastic model of a Swift's wing placed in a water channel, and it was noted that the wing was able to passively flex and rotate in the flow. The model was made with a sharp leading edge, and no force measurements were made. Flow field measurements (DPIV) were made near the wing to identify the

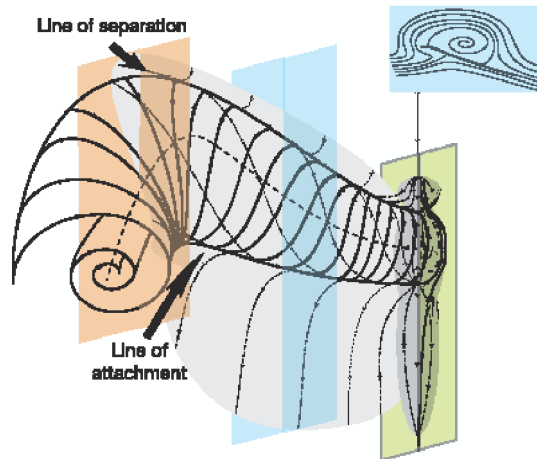


Figure 1.17: The vortex formed by a free flying butterfly (Srygley)  
 This schematic illustrates how separation and reattachment are caused by the LEV, and how this can increase the effective camber. [39]

formation of the LEV, and a schematic of this LEV is shown in figure 1.18. Despite the lack of force measurements, the LEV was thought to provide an increase in lift for the small bird, similar to what happens for insect flight.

However, the later study shows that the LEV appears at  $\Lambda > 30^\circ$  and does not provide an increase in lift. [18] The wings used in this study were frozen wings of dead Swifts, arranged in different sweep configurations. They were also able to flex and rotate passively in the flow. The sweep of the wing was varied by rotating the wings back, thus changing the aspect ratio and area of the wing. Force balance measurements were made in a wind tunnel, and the LEV presence was determined using a tuft of hair moved along the wing surface. It was determined that the LEV did not increase the lift produced by the wing because to form the LEV, the wing needed to be swept back, which reduced the wing area. Essentially, any increase in lift generated by the LEV (if there is any), is neglected by the decrease in lift caused by the decrease in wing area from sweeping the wings back.

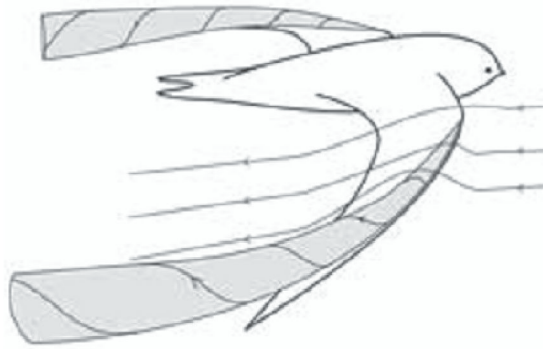


Figure 1.18: The vortex formed by a model swift wing (Videler)

This LEV is formed with a steady wing, but generates the necessary spanwise flow with the swept wings. Studies on this mechanism have not been conclusive, and more controlled experiments must be conducted to determine the importance of sweep in generating an LEV in this way. [41]

These last two studies suggest that it might be possible to improve fixed-wing air vehicles by using a LEV. The later study claims that the LEV does not increase the lift, but fails to consider the possibility of a  $C_L$  improvement caused by the LEV. In studying the formation of an LEV on a swept wing at  $Re \approx 10^4$ , these studies have focused on replicating biological models that have unspecified and varying sweep along the span, unspecified and varying taper angles along the span, and flexible models that allow for unknown dihedral and twist in the wing. Also, the airfoil shape used is unknown and may play a dominant role in their results. Finally, neither study measured both the flow field and forces of the model. Hence, it is still unclear whether the LEV forms and how it effects the forces on the wing. It is also unclear how the various geometric properties of the wing effect their results. If an air vehicle is to be designed to use a leading edge vortex, carefully controlled experiments must be carried out where the properties of the model are fully known.

# Chapter 2

## Problem Statement

### 2.1 Model Geometry

Any flying vehicle will have a finite aspect ratio. Thus far, the majority of the tests have restricted themselves to studies of 2D airfoil geometries by using end plates. If the goal is to gather data useful to flying vehicles, then some study should be done of finite aspect ratio wings to understand how three-dimensionality effects the aerodynamics of wings at this range of  $Re$ .

Studying both finite aspect ratio wings and 2D airfoils allows comparisons to be made using potential flow theories such as Lifting Line Theory. Comparisons with these theories have been made by Laitone [16] and Mueller [29], but their results lead to opposite conclusions. Laitone's study of aspect ratio 6 wings indicates that lifting line theory does not apply to this range of  $Re$ , while Mueller's results from aspect ratio 3 wings suggest that it does. It is still unclear whether these theories apply at  $Re < 10^5$ .

### 2.2 Force Measurements

There is a very limited amount of data on the forces generated by airfoils and wings at  $10^4 < Re < 10^5$ . There was only one study mentioned in the previous chapter [16] that was focused solely on this range of  $Re$ , and this was also the only study of airfoils and wings at  $Re < 5 \times 10^4$ . Every other study was typically focused on  $Re > 10^5$ .

Since planes are currently being built with operational  $Re$  as low as  $3 \times 10^4$ , and since there is much interest in operating at even smaller  $Re$ , it is important to understand how the forces generated by the wing change throughout the entire range of  $10^4 < Re < 10^5$ .

Measuring forces at these low  $Re$  is a challenge because the forces are so small. Since the lift is typically an order of magnitude larger than the drag, lift measurements have typically been done using a strain gauge force balance. However, drag measurements have often relied on the wake defect. Due to the span-wise variation in the wake of wings at these low  $Re$ , this technique can yield inaccurate results.

Some studies that have attempted to measure drag at these low  $Re$  used a force balance with a minimum resolvable force that is near the drag forces measured. The only reliable measurements of both the lift and the drag of airfoils and wings at this  $Re$  was done by Laitone, and he used a strain gauge force balance that was capable of resolving adequately small forces (0.1 mN). [16]

## 2.3 Eppler 387 Performance

The E387 is one of the most widely studied airfoils at  $Re \approx 10^5$ . Section 1.3 showed reliable force measurements made at various facilities. The measurements were in relatively good agreement when  $Re \geq 10^5$ , but at  $Re = 6 \times 10^4$  (the lowest  $Re$  of the studies) there was considerable disagreement in the measurements. Also, at this  $Re$ , there was a drastic drag increase at moderate lift coefficients.

The source of these discrepancies is not fully understood, and the cause of this drag increase has not been identified satisfactorily. Further, it is not clear what happens to the forces as the  $Re$  decreases below  $6 \times 10^4$ .

## 2.4 Laminar Separation Bubble

The laminar separation bubble is currently used to explain the peculiar drag increase at moderate lift coefficients often seen for airfoils at low  $Re$  (eg. the E387 at  $Re = 6 \times 10^4$ ). Selig refers to this drag increase as the “bubble drag”. However, experiments done thus far to measure the LSB have focused on cases where there is very little drag increase at moderate lift coefficients. The results of Selig [37] and Broeren and Bragg [8] showed surface oil flow visualization for the E387 at  $Re \geq 2 \times 10^5$ . However, at these  $Re$ , the E387 has no drag increase at moderate lift coefficients (see figure 1.4). The bubble drag doesn’t seem to be present until  $Re \leq 1 \times 10^5$ . When an experiment to visualize the LSB was performed at  $Re \leq 1 \times 10^5$ , it was performed on the SD7003 airfoil at  $Re = 6 \times 10^4$ , that has no drag increase at moderate lift coefficients (see figure 1.10). [27] [35]

Furthermore, every study of the LSB has been conducted at a small number of angles of attack and  $Re$ , and none have studied how the forces generated by the wing are affected by the presence or absence of the LSB. There is no study of the both the forces and flow field of an airfoil when it has a drag increase at moderate lift coefficients to show how the LSB effects the forces generated by the airfoil.

## 2.5 Leading Edge Vortex

Previous measurements of the LEV formed on swept wings at  $Re < 10^5$  have been conducted from a biological perspective: to identify fluid-dynamic mechanisms that explain how a specific bird flies. However, when building new small scale flying devices, this is not as useful as taking an engineering perspective: to identify the important parameters that cause these fluid-dynamic mechanisms to form. Previous experiments have been done on model bird wings that have taper, non-constant airfoil geometry, non-constant

sweep angle, and feathers. They also have some amount of flexibility that allows them to flex and rotate, giving an undefined dihedral angle and  $\alpha$ . Furthermore, when they study the effect of sweep, they often vary the aspect ratio, stream-wise chord length, and area of the wing as well.

# Chapter 3

## Proposal

The first objective of this study is to measure the forces produced by wing and airfoils at  $Re \leq 6 \times 10^4$ . Three airfoil shapes are tested at  $Re = 1, 2 \times 10^4$ , in 2D and 3D conditions, and at  $-10^\circ < \alpha < 20^\circ$ . These tests take place in the USC Dryden wind tunnel using a custom designed force balance. This test is designed as a survey study, and also to allow comparison of Lifting Line Theory predictions at this range of  $Re$ .

One of the airfoils is the Eppler 387, and this airfoil is the only airfoil tested at  $Re = 3, 4 \times 10^4$ . These higher  $Re$  are used to compare with previous measurements, and to identify the transition from low  $Re$  performance to high  $Re$  performance, illustrated in Schmitz's plot (see figure 1.1). Both 2D and 3D conditions are tested, and measurements are made at  $-10^\circ < \alpha < 20^\circ$ .

Flow field measurements of the Eppler 387 at these higher  $Re$  are taken using PIV in the wind tunnel. The flow field measurements will have two magnification levels. One level will view the entire chord of the wing, and will capture the global flow field, while the other will be zoomed in on approximately 25% of the chord to identify details of the boundary layer.

To identify how sweep effects thin, cambered wings at  $Re < 10^4$ , a series of swept wings are built with sweep angles between  $0^\circ$  and  $60^\circ$ . These wings each have a simple, thin, circular-arc cambered airfoil as the stream-wise cross-section, no taper, constant sweep angle, the same aspect ratio of 6, and the wings are made of brass, which is sufficiently rigid to resist any significant change in dihedral or twist of the wing. These wings are tested using dye visualization in the USC water channel. The purpose is to

identify conditions where an LEV forms for a simple geometry with properly defined parameters.

These swept wings are then tested in the wind tunnel, similar to the rectangular wings. Force measurements are taken for all sweep angles and incidence angles, and PIV flow field measurements are made for sweep angles where LEVs are formed. This will determine if the LEV significantly effects the forces generated by the wing or not, and will give estimates of velocity and vorticity around the wing and vortex.

# Chapter 4

## Methods

### 4.1 Models

#### 4.1.1 Rectangular Wings

Three airfoil geometries are chosen for this study: an flat plate airfoil, a cambered plate airfoil, and the Eppler 387 (E387) airfoil. Each wing has a chord of 3.5 cm, and an aspect ratio of 6. They are milled on a CNC mill with 0.0005 in resolution. The wings were then sanded and painted flat black, to ensure the wings are smooth and for improved PIV data acquisition. For image acquisition, one should absorb all incoming light, and flat black does that best. The airfoil shapes used are shown in figure 4.1, and are described in detail below.

The flat plate airfoil was chosen because many other researchers have used a similar geometry in their studies, and because the drag at  $\alpha = 0^\circ$  can be compared with the Blasius boundary layer drag. The airfoil has no camber, a round leading edge, a constant thickness section, and a tapered trailing edge. The exact geometry is based off the models used by Mueller et al in their studies. [28] The leading edge is a 5:1 semi-ellipse, with the major axis along the chord line. The thickness of the wing was 1.3 mm (3.6% thick), 87% thicker than Mueller's 1.93% thick wings. The trailing edge was linearly tapered over the last 18% of the chord, and brought to a sharp edge.

The cambered plate airfoil was chosen also because many other researchers have study this type of shape, and it has been found to perform better at this range of Re than

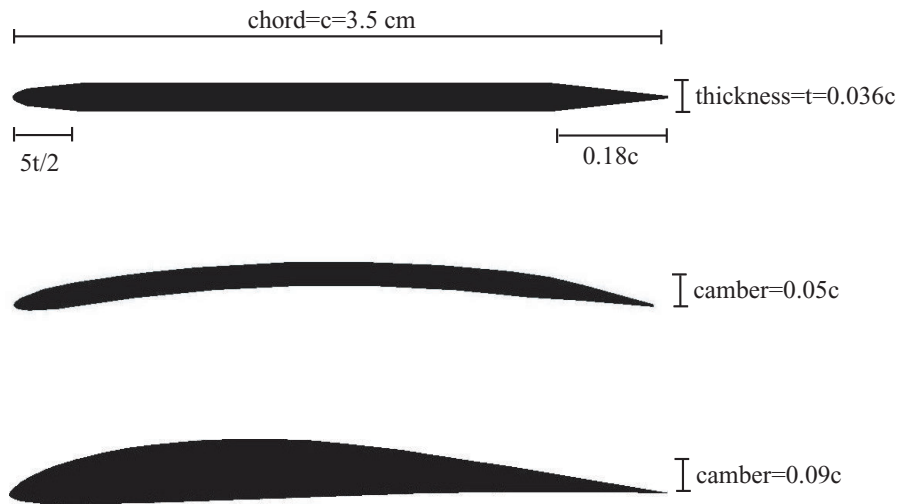


Figure 4.1: Three airfoil shapes studied

Three airfoil shapes were studied: the flat plate airfoil, cambered plate airfoil, and the Eppler 387 airfoil.

many thick, cambered airfoils. The plate is designed exactly as the flat plate airfoil, but the geometry is rounded to a 5% camber. This is the same camber as used by Laitone [16], and is 25% more camber than the 4% cambered plates used by Mueller et al [28].

The Eppler 387 is one of the most widely tested airfoils at  $Re < 10^5$ , and is a championship airfoil for sail plane competitions. It has a maximum thickness of 9% at the 31% chord location, and a maximum camber of 4% at the 42% chord location. While this airfoil has been tested extensively at  $Re \geq 6 \times 10^4$ , it has not been tested at lower  $Re$ , and this will be the first test to do so.

In order to compare our results for the Eppler 387 to previous results, a larger version of this airfoil was made to increase the  $Re$ . This new wing has a chord of 9 cm, and has aspect ratio 6. It was CNC milled similar to the smaller wings, but was not sanded or painted before tests were performed. This larger wing was not rough to the touch, but

there were optical indications of roughness on the surface. Tests were conducted with this rough wing to ensure a laminar separation bubble formed on the wing in the low turbulence wind tunnel. After tests were conducted, the wing was sanded and polished, and tested again.

### **4.1.2 Swept Wings**

Four wings were made of 0.08 cm thick brass shim stock, each with a 4.45 cm chord, 5% circular-arc cambered airfoil and sweep angles:  $\Lambda = 0, 20, 40, 60^\circ$ , as seen in figure 4.2. Each wing has an aspect ratio of 6, an area of  $119 \text{ cm}^2$ , a thickness ratio of 1.8% ( $0.08/4.45$ ), and no taper. The wings were made by rolling the shim stock to the specified camber, then soldering each half of the wing together. The sting (support mount) was made by stacking 3 pieces of the same brass shim stock together. The final 1 cm of the sting did not have the outer 2 pieces attached, to make the sting thinner and have less effect on the flow. It was soldered to the wings in the center of the wing (at the apex). The chord-wise dimension of the sting was 3.4 cm.

## **4.2 Flow Facilities**

### **4.2.1 Wind Tunnel**

The Dryden Wind Tunnel will be used for this study. It is a closed wind tunnel with 12 anti-turbulence screens, and the ratio of the settling chamber cross sectional area to the test section cross sectional area is 7:1. The test section (shown in figure 4.3) is octagonal, and the parallel edges are 1.37 m apart, which gives a cross sectional area of  $1.56 \text{ m}^2$ . The test section has three transparent windows, located on top, on the side, and on the lower left hand corner.

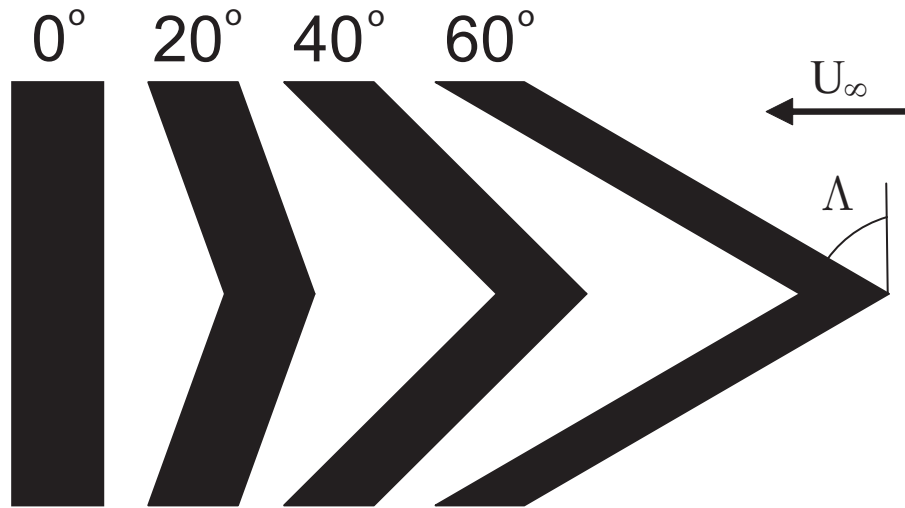


Figure 4.2: Swept wing planforms

Four sweep angles were studied:  $0^\circ$ ,  $20^\circ$ ,  $40^\circ$ , and  $60^\circ$ . Each wing had the same aspect ratio, wing area, streamwise chord, and streamwise airfoil geometry. The airfoil used was a 5% circular-arc cambered plate, with blunt/rectangular leading and trailing edges.

The relatively large number of anti-turbulence screens and the relatively large contraction ratio provides very low turbulence intensities in the free-stream of the test section. The turbulence intensity is defined as

$$q = 100 \times \frac{u'}{U} \quad (4.1)$$

Much care was taken in measuring the turbulence in the test section because at  $Re < 10^5$ , it can have a large effect on the measurements made. The turbulence measurements were made with a hot-wire anemometer probe. Measurements were made across the test section area to ensure spatial homogeneity.

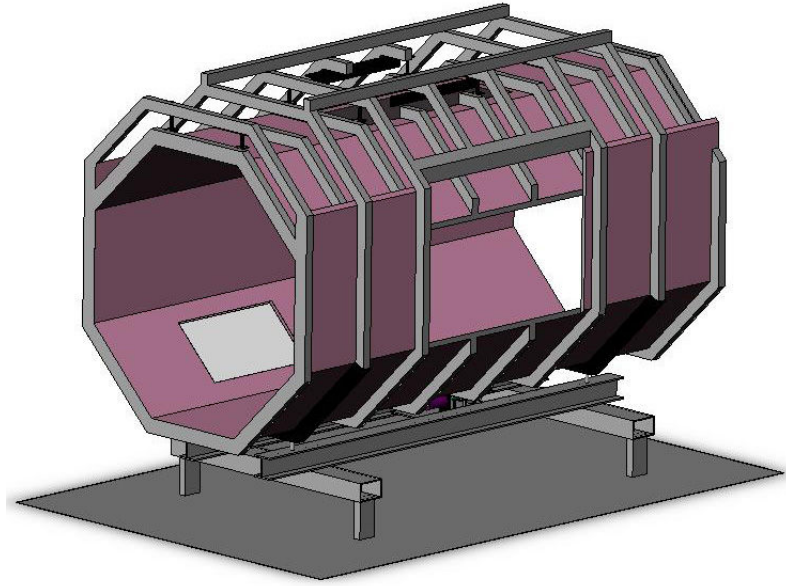


Figure 4.3: The USC Dryden wind tunnel test section

The perpendicular distance from flat side to flat side is 1.37 m, which is more than 6 times larger than the span of the small models, and more than 2.5 times the span of the large E387 model. The three viewing windows are on the top, the side, and at the bottom left.

The hot-wire apparatus consists of a  $1.5 \mu\text{m}$  tungsten wire attached to a support. The wire is supplied with a voltage from an A. A. Laboratory Systems hot wire signal conditioning unit. The current running through the wire increases the temperature of the wire. Since the resistance of the wire is directly related to the temperature, this increase in temperature will increase the resistance. When the hot-wire is placed in a flow, the temperature of the wire is decreased proportional to the velocity of the flow. The signal conditioning unit adjusts the voltage to maintain a constant wire resistance, and hence a constant temperature of the wire. If there is higher velocity, then less voltage and current will be required to maintain a constant resistance and temperature of the wire. Thus, the voltage required is inversely related to the velocity of the flow. The thermoelectric properties of the wire, and the small diameter, result in frequency responses up to 1 kHz.

This high frequency response allows the measurement of the rapid fluctuations referred to as free-stream turbulence.

Results of the turbulence measurement show that the turbulence level is uniform across the test section, and is always below 0.03%. A measurement of the velocity fluctuations was done in the upper right quadrant of the wind tunnel, and figure 4.4 is a plot of the RMS of the velocity fluctuations plotted across that section of the wind tunnel. This measurement was taken for a free-stream speed of 10 m/s, and fluctuations as small as 0.01 m/s were well resolved with the hot-wire apparatus. The average turbulence in the wind tunnel is 0.025%, which is well below the 0.1% identified by Schubauer and Skramstad [32] as causing early transition on flat plates. Thus, the effect of turbulence on the present tests should be minimal.

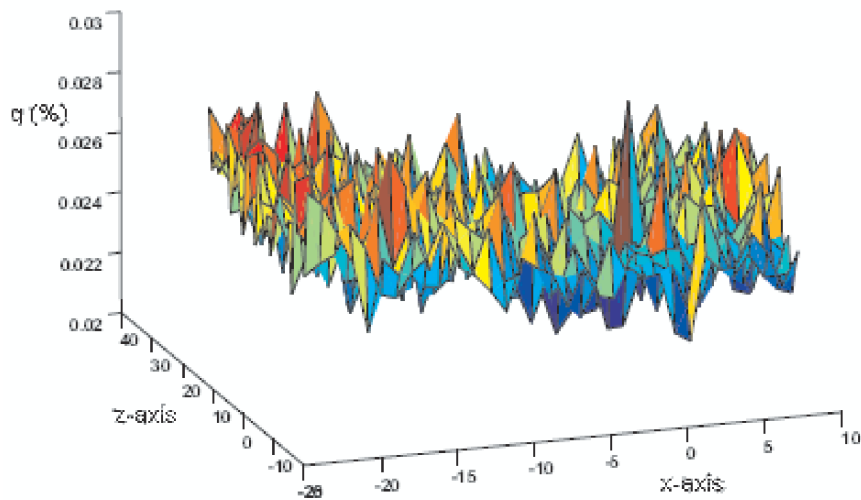


Figure 4.4: Wind tunnel turbulence uniformity

A plot of RMS velocity fluctuations in the USC Dryden Wind Tunnel shows that everywhere the turbulence intensity is less than 0.03%. The x-axis is the location in the horizontal cross-stream direction, while the z-axis is the vertical cross-stream direction. The ordinate is the turbulence intensity at a given point in the wind tunnel. The plot is for the upper right corner of the wind tunnel, and the center of the wind tunnel is at (0,0).

## **4.2.2 Water Channel**

Dye injection experiments were conducted on swept, cambered plate wings in the USC water channel. The water channel is a closed-loop, horizontal flow facility. The channel has a depth of 60 cm, a width of 91 cm, a length of 10 m, and was run at a speed of 10 m/s for all tests of this study. A diagram of the water channel is shown in figure 4.5.

This flow speed was chosen based on a balance of pros and cons. For comparisons with the wind tunnel results, the desired  $Re$  was  $10^4$ . However, for proper comparisons, the aspect ratio of the wings should also be 6, as in the wind tunnel experiments. To minimize the effects of the channel walls, at least 1 span should separate the wing tips and the walls on either side, so the wing span is limited to 30 cm, and the chord should be approximately 5 cm. To match the  $Re$ , the water channel speed should be 20 m/s. However, dye visualization was not feasible at this high speed as the dye streak became unstable. Thus, 10 m/s was chosen as a reasonable balance.

## **4.3 Measurement Techniques**

### **4.3.1 Force Balance**

For measuring forces in the wind tunnel, a custom-made force balance will be used. The force balance resembles a 3 layer sandwich composed of a bottom plate, a cruciform in the middle, and a top plate. The bottom plate attaches to the cruciform at two opposing endpoints of the cruciform, while the top plate attaches at the other two opposing endpoints. In figure 4.6 the long side-arms on the left and right attach to the top plate. Four strain gauges are located on each arm of the crucifix, and they form a wheatstone bridge which is used to measure the deflection of each arm. The strain at each strain gauge

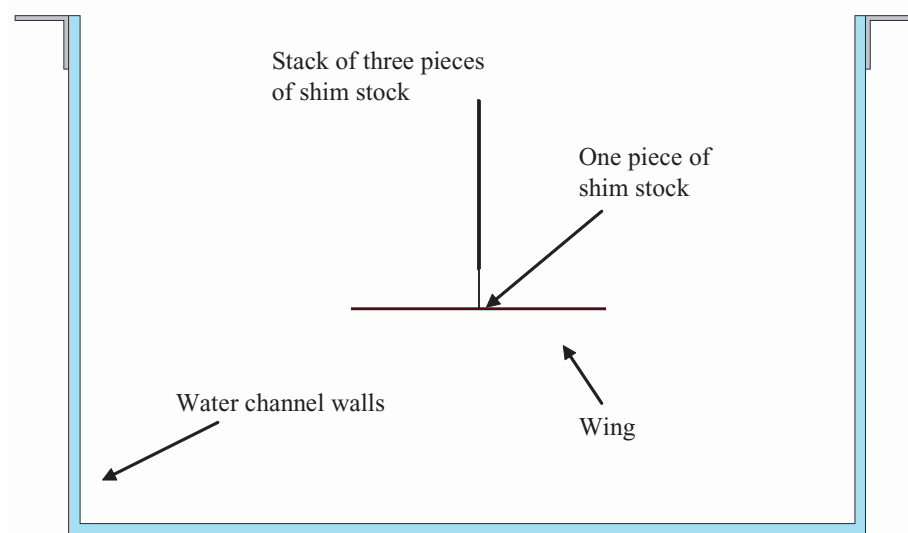


Figure 4.5: Water channel with wing

This streamwise view of the water channel demonstrates the relative size of the wing. The width of the water channel is more than 3 times the span of the swept wings.

location is maximized for a given deflection by hollowing out the arm, and placing the strain gauge at the thinnest point of the arm.

In the diagram, the output voltage of bridge A and D are sensitive to horizontal forces, while bridge B and C are sensitive to vertical forces. Thus, any force applied to the force balance can be resolved into two directions which are decoupled and measured independently. Combining the voltages from the bridges ( $V_A$ ,  $V_B$ ,  $V_C$ ,  $V_D$ ), one can produce 2 voltages related to the forces.

$$V_{Horizontal} = V_A + V_D$$

$$V_{Vertical} = V_B + V_C$$

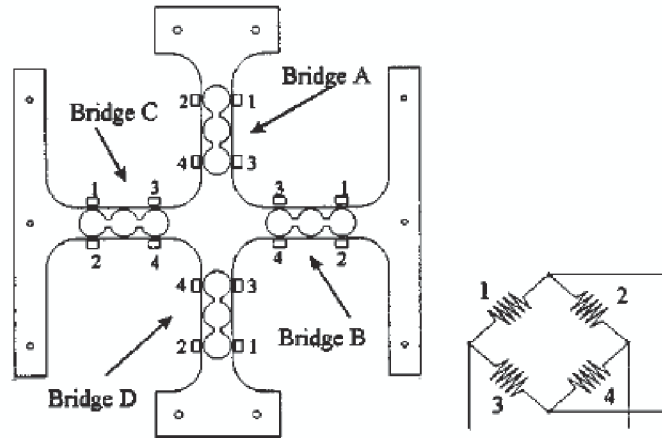


Figure 4.6: Force balance planform

The long side arms attach to the top plate, while the short side arms attach to the bottom plate. Four strain gauges are placed at the thinnest points of each arm, and as far from each other as possible. These form a wheatstone bridge: the excitation voltage is applied from top-to-bottom, and the bridge voltage is measured across the left and right corners.

Any out-of-plane moment applied to the force balance will not effect the output of these 2 voltages. This is because of the symmetry in the design. A calibration between the forces applied to the force balance and the voltages recorded, yields the calibration coefficients. For improved accuracy of the measurements, a cross-talk calibration scheme is employed which allows both forces to each effect the voltages described above. The following equation describes the cross-talk:

$$V_{Horizontal} = A_{11}F_{Horizontal} + A_{12}F_{Vertical} + A_{13}$$

$$V_{Vertical} = A_{21}F_{Horizontal} + A_{22}F_{Vertical} + A_{23}$$

where A is the calibration matrix, and F is the forces applied in the given direction. Cross-talk is important because it has been observed that applying a horizontal force

causes a small but significant affect on the vertical voltage, and vice-versa. When running an experiment, this set of equations must be inverted to yield the forces as a function of the voltages measured:

$$F_{Horizontal} = B_{11}V_{Horizontal} + B_{12}V_{Vertical} + B_{13}$$

$$F_{Vertical} = B_{21}V_{Horizontal} + B_{22}V_{Vertical} + B_{23}$$

where **B** is now the calibration matrix.

To measure the small forces of the wings at low Re with a force balance, the small voltages produced by the force balance must be measured. An estimate of the magnitude of the lift and drag forces of a wing can be made using the standard equations:

$$L = C_L \frac{1}{2} \rho U^2 cb$$

$$D = C_D \frac{1}{2} \rho U^2 cb$$

where  $C_L$  and  $C_D$ , are the lift and drag coefficients respectively, and  $c$  and  $b$  are the chord and the span of the wing respectively. Rearranging these equations in terms of the Re, and the aspect ratio (A) yields:

$$L = C_L \frac{1}{2} \frac{\mu^2}{\rho} Re^2 A$$

$$D = C_D \frac{1}{2} \frac{\mu^2}{\rho} Re^2 A$$

From this set of equations, one can take any previous experiments and calculate the magnitude of the forces and moments by only knowing the fluid properties, the Re, and the aspect ratio. Referring to figure 1.4, the  $C_L$  and  $C_D$  will likely range from 0 to 1.5 and from 0.01 to 0.1 respectively. From these estimates of the coefficients, assuming

normal atmospheric conditions for  $\mu$  and  $\rho$ , working at a the lowest Re of this study ( $1 \times 10^4$ ), and an aspect ratio 6 wing with 3.5 cm chord, the lift and drag forces will vary from 0 to 100 mN and from 0.8 mN to 8 mN.

The force balance is connected to a signal processing board that applies the excitation voltage and amplifies the bridge output voltage. At the largest amplification factor available, the force balance has a nominal sensitivity of  $1 \frac{\text{mV}}{\text{mN}}$ . This amplified bridge voltage is sent to a computer via a 12-bit analog-to-digital (ADC) converter with 10 volt range. This gives a 2.5 mV resolution of the ADC, which is not adequate for measuring the drag forces at this Re. However, the electronic noise in the system is set above the resolution, and can be used to enhance the resolution by over-sampling and averaging the measurement.[15] The effective number of bits (ENOB) is calculated with the oversampling ratio (OR):

$$\text{ENOB} = \text{NOB} + \log_4(\text{OR})$$

where the 4 is a constant of the equation, and the NOB is the number of bits of the ADC. For this study, 8000 samples were made over the course of 8 seconds and averaged to provide one measurement of the forces. Thus, the oversampling ratio was 8000. This provides an ENOB of 18.5, and a minimum resolvable voltage of 0.05 mV. This is sufficient to resolve the minimum drag force at this Re.

Repeated calibrations showed that the relationship between voltages and forces was linear and consistent over multiple measurements. The calibrations were performed using objects that were measured on a commercial scale with resolution of 0.01 mN, and the calibration was performed in the wind tunnel to minimize any disturbances due to location or moving the force balance. The force balance was placed under the wind tunnel, and a steel rod (commonly referred to as the "sting") was connected to it. The sting protrudes into the wind tunnel, and the wings were designed to be placed at the end

of the sting, in the center of the wind tunnel. The calibration was performed by pulling on the end of the sting in the lift and drag directions. Objects were placed in cups with a string attached that wrapped around a pulley and connected to the sting.

An example of the calibration results for the drag at  $Re = 1 \times 10^4$  is shown in figure 4.7. This plot is generated after each calibration to ensure it was done correctly. The abscissa is the drag forces used during the calibration while the ordinate is the drag forces predicted by using the measured voltages and the calibration coefficient. For a perfect calibration, the points would be in a straight line with a slope of 1. A linear curve fit is plotted along with the calibration points and the equation and R-squared value is shown. The slope is within 0.1% of 1, as is the R-squared value, which is sufficient for this study. Uncertainty is estimated by the RMS of the difference between predicted and actual forces at each calibration point. The uncertainty is estimated to be 0.0003 mN for the drag calibration shown above, and error bars are plotted but are smaller than the symbol size.

The calibration weights used may seem too large based on the estimate of the forces given earlier. The drag for the current experiments was estimated to vary between 0.8 mN and 8 mN at  $Re = 1 \times 10^4$ . The calibration only contains two calibration points below 10 mN, which is not sufficient. However, the drag estimate was based on drag coefficient measurements made by Selig et al at  $Re = 6 \times 10^4$ . As  $Re$  decreases below this  $Re$ , the drag coefficient increases dramatically, and experience has shown the actual drag at  $Re = 1 \times 10^4$  varies between 5 mN and 30 mN. Thus, the current calibrations are sufficient for the measurements made.

### **4.3.2 Particle Image Velocimetry**

For the flow visualization, a custom made Particle Image Velocimetry (PIV) system will be employed. A PIV system works by seeding a flow with particles that act as passive

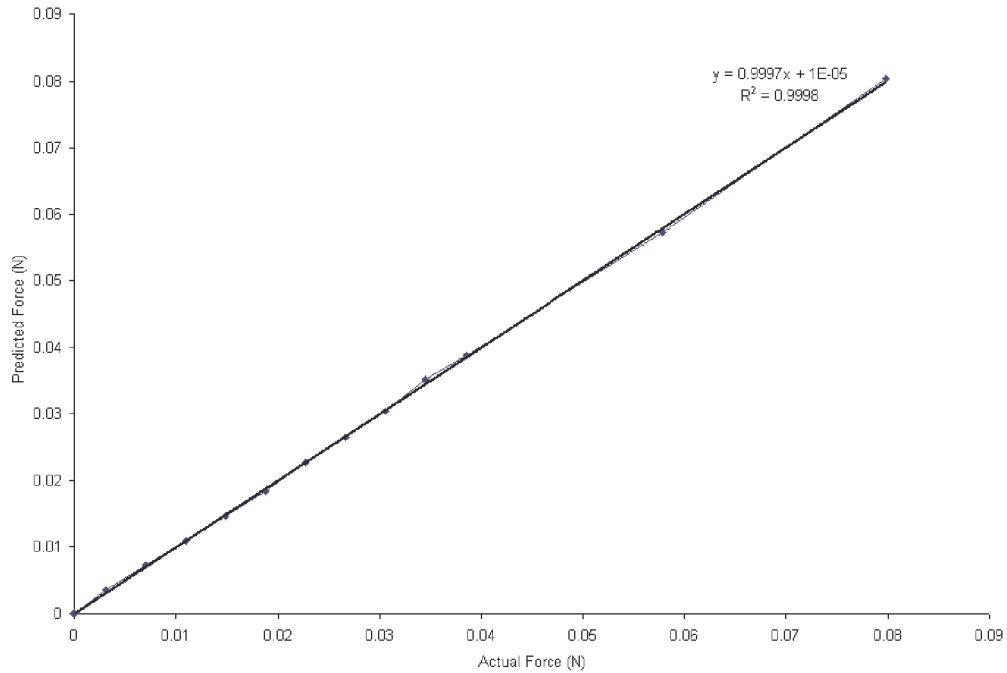


Figure 4.7: Drag calibration results

Calibration of the Drag for the lowest Re measurements. The abscissa is the actual force applied in the drag direction, while the ordinate is the force calculated using the measured voltages and the calibration coefficients. Error bars to represent the uncertainty are smaller than the symbol size.

tracers of the velocity field. Two images are taken of the particles in rapid succession in such a manner that the majority of the particles in the first image are still present in the second image. Then, particle displacements are computed by comparing the two images. Dividing the particle displacements by the time between the images yields the instantaneous velocity at each point. For the current experiment, a laser is used to illuminate a single plane of the flow and thus only 2 components of the velocity field can be measured. The PIV algorithm used to calculate the velocity field in this experiment is called Correlation Image Velocimetry (CIV) and has been documented previously in [9]. All image velocimetry algorithms are focused on the correct reconstruction of both the velocity fields and the spatial gradients, regardless of computational cost.

A Kodak ES 1.0 CCD camera with 1008 x 1018 pixels will be placed above the wind tunnel to capture images. It is connected to a frame grabber card on a digital computer to acquire the images. Two lenses will be used for the study. The first has a focal length of 85 mm and can visualize approximately a 12 cm x 12 cm region at the center of the wind tunnel. This is large enough to capture the flow field around the larger E387 wing with a chord of 9 cm. The other lens has a focal length range of 80-200 mm and can focus on a region as small as 3 cm x 3 cm at the center of the wind tunnel. This lens will be primarily used to visualize the boundary layer of the larger E387 wing and identify separation and reattachment points.

The wind tunnel flow will be seeded with smoke particles generated by heating oil past its boiling point using a Colt 4 smoke generator. The smoke particles have a nominal diameter of 3  $\mu\text{m}$  and act as passive tracers of the velocity field. Two lasers will be used to illuminate a sheet of particles in the wind tunnel. The lasers are 6 W Nd-Yag lasers with 4 ns nominal pulse-width and a repetition rate of 10 Hz. The lasers are fired in rapid succession (typically about 100  $\mu\text{s}$ ) and are timed with a Stanford timing box capable of 1 ns pulse separation. The amount of time between the two lasers firing is determined by the velocity in the wind tunnel and the zoom of the camera. The objective is to have an average particle displacement that is approximately 5 pixels. Thus, the time between pulses is

$$\Delta t = \frac{5}{UZ}$$

where  $\Delta t$  is the time between pulses, the 5 is for the 5 pixel displacement, and Z is the pixels/cm of the camera.

The beam of the lasers is converted to a sheet by using a series of cylindrical and spherical lenses. The objective is to have a wide, thin sheet with adequate amounts to energy to illuminate the particles. The first lens is a spherical lens which acts to focus

the beam. The next lens is a cylindrical-diverging lens which acts to stretch the beam and create a sheet. The final lens is another cylindrical-diverging lens, but oriented perpendicular to the previous lens. It straightens the sheet edges and creates a nearly constant thickness sheet in the beam direction.

The PIV correlation algorithm works by allowing the user to select the size of the correlation and search boxes in number of pixels. The process is to take a correlation box in the first image, and search (within the search box size) for the highest correlation in the second image. The algorithm can achieve sub-pixel resolution by plotting the correlation value for each point in the search box, then curve fitting a smoothed spline surface to it and selecting the location where the curve fit is maximized. This technique has been verified for various cases, and yields a velocity bandwidth of approximately 1/200, which means that velocities are accurate to about 0.5% of the maximum value measured. [9]

Calibration of the PIV system was performed by printing crosses onto a sheet of paper, placing the paper at the location of the laser sheet, focusing the camera on the paper, and taking a picture. The pixels per cm was calculated by image analysis of this reference target. A typical resolution of the camera with the 80 mm lens was  $84.4 \pm 0.2$  pixels/cm.

In any PIV experiment, data acquisition parameters and algorithm settings must be adjusted appropriately for flow complexity. In the present experiments, the sheet thickness was approximately 1 mm thick at the center, and approximately 20 cm wide across the wing tunnel. The timing between images was adjusted based on the ability of the CIV algorithm to find good correlations. Time between images was nominally 200  $\mu$ s. For the CIV algorithm, a correlation box size of 30 pixels, and the search box size of 44 pixels was typically used.

### 4.3.3 Dye Visualization

The dye was injected 16 cm upstream of the wings using a syringe pump and a 1.6 mm outside diameter, 1 mm inside diameter tube. The tube extended vertically into the water channel, has a 4 cm bend radius near the end, and a 2 cm horizontal section after the bend. The water channel was set to a nominal speed of 10 cm/s, which made the chord based  $Re = 5 \times 10^3$ . This choice of dye injection tubing and water channel speed provided enough stiffness in the tubing so that it did not bend, laminar boundary layer flow inside and outside the tube so that the dye streak was steady, and a large enough bend radius so that the vortex shedding of the vertical tube did not effect the dye streak.  $\alpha$  was varied between a nominal  $0^\circ$  and  $20^\circ$  in  $2.5^\circ$  increments.

Images and video were taken using a Sony CyberShot digital camera with manual and automatic mode to allow fine-tuning of the image acquisition parameters. Low temperature compact fluorescent lamps (CFL) were used to light the water channel. Images were taken from the right-side of the wing (looking upstream) and from various angles around the wing. Images were later analyzed to provide a better estimate of the angle of attack of the wing, with less than  $1^\circ$  uncertainty.

# Chapter 5

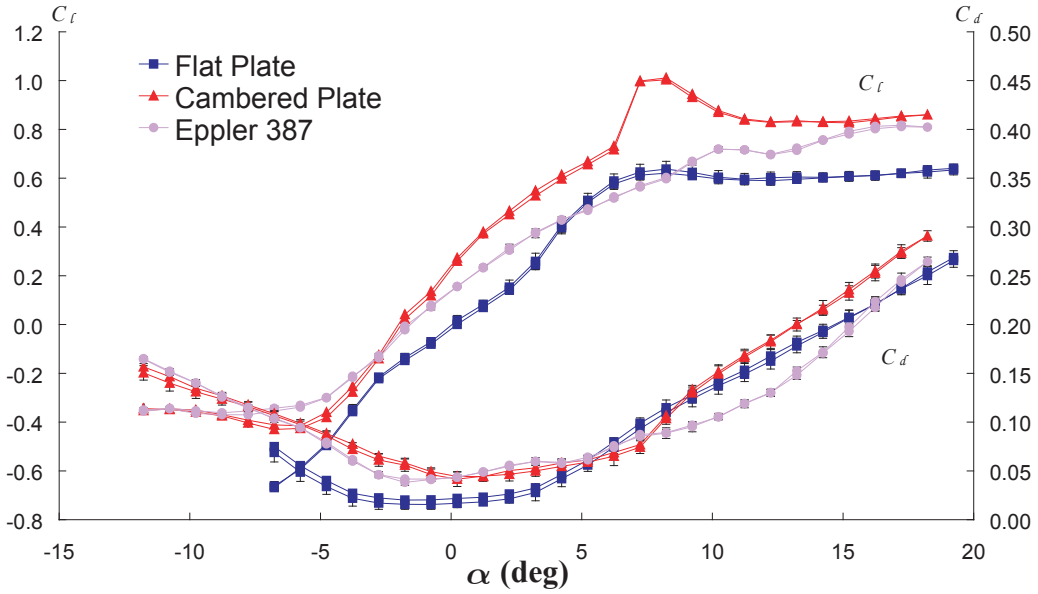
## Results

### 5.1 Aerodynamics at Re=10k and 20k

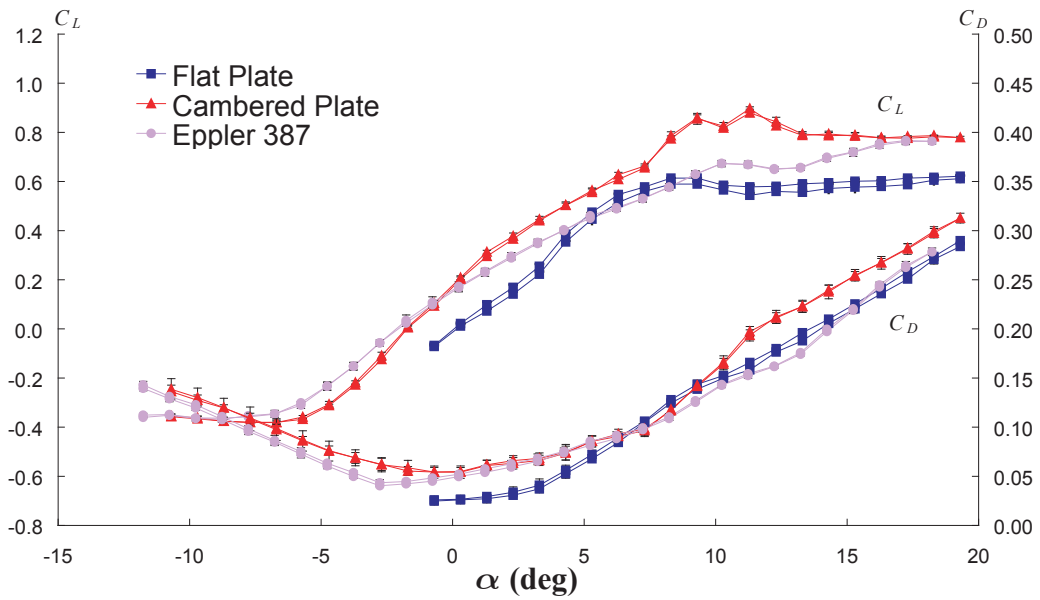
#### 5.1.1 Force Balance Measurements

Force measurements have been made for the flat plate, cambered plate, and E387 airfoils using the force balance. The measurements were made at  $Re = 1 \times 10^4$  and  $2 \times 10^4$  for the range  $-10^\circ < \alpha < 20^\circ$  in  $1^\circ$  increments. Tests have been run with and without end plates to measure 2D airfoil performance, as well as aspect ratio 6 wing performance. The first comparison is of each airfoil shape, at both Re, for the 2D and 3D cases. The measurements for  $Re = 1 \times 10^4$  at 2D and 3D conditions are shown in figures 5.1(a) and 5.1(b), while figures 5.2(a) and 5.2(b) are measurements for  $Re = 2 \times 10^4$  at 2D and 3D conditions. The flat plate was not tested at all  $\alpha < 0$  because it is symmetric. For each plot, the lift and drag coefficients are plotted versus  $\alpha$  and error bars indicate the standard deviation of 4 measurements. For a single measurement, 8000 samples were taken at 1 kHz and averaged. For each of the 4 tests, the wing was started at the lowest  $\alpha$ , then increased to the highest, then decreased back to the lowest. This was done to check for hysteresis.

The 5% cambered plate airfoil attains higher  $C_L$  than the E387 airfoil at most  $\alpha$ , both Re, and at 2D and 3D conditions. This is similar to the results of Laitone ([17]) where a 5% cambered plate achieved higher  $C_L$  values than a NACA0012 airfoil. In this case however, the E387 airfoil was specially designed to be high lift, while the NACA0012

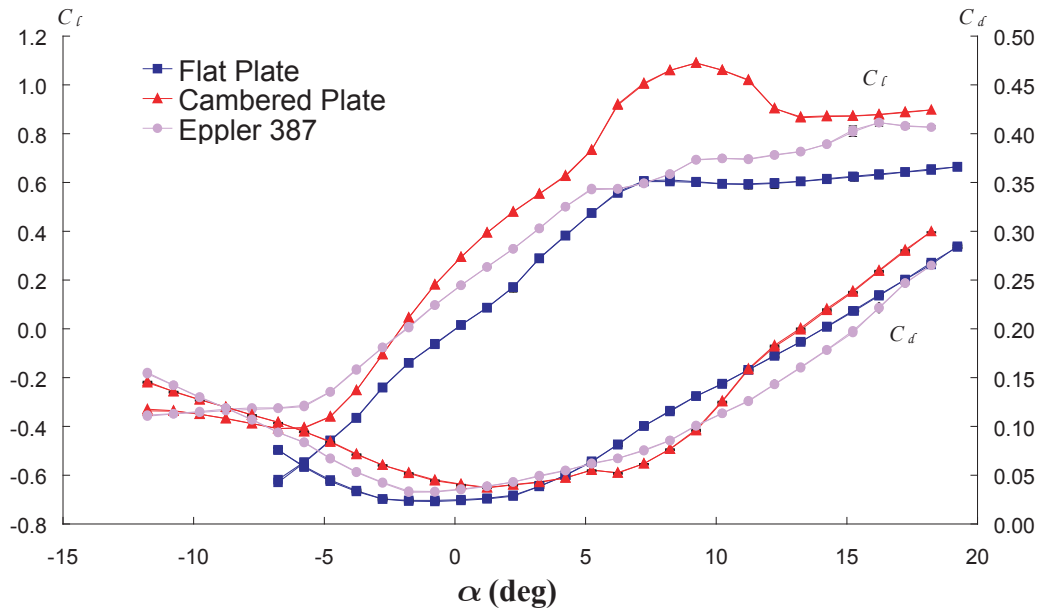


(a) With endplates - 2D airfoil

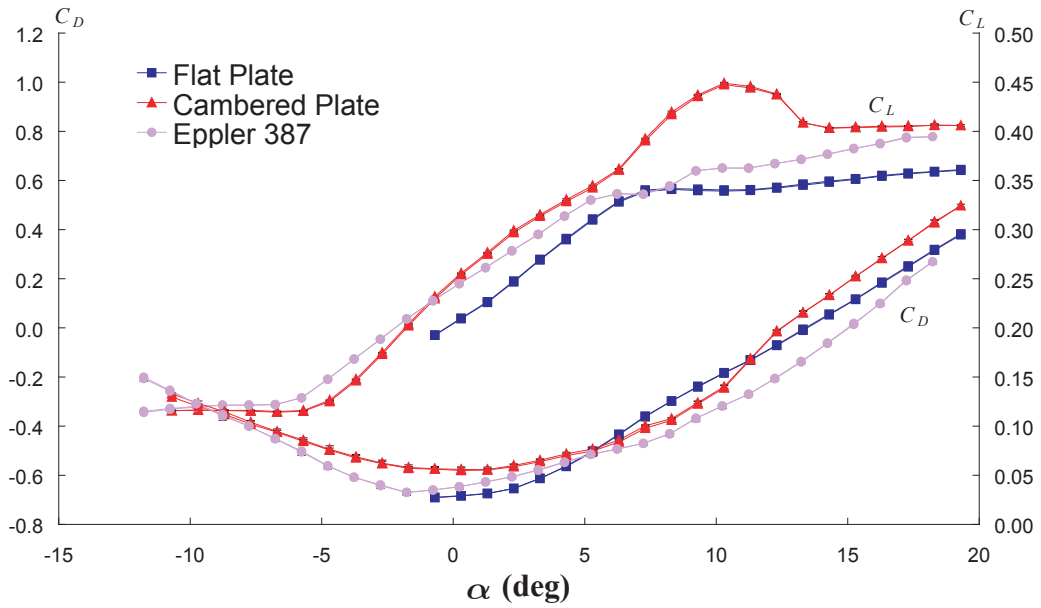


(b) Without endplates - aspect ratio 6 wing

Figure 5.1: Airfoil force coefficients at  $Re = 1 \times 10^4$ . Increasing and decreasing  $\alpha$  are plotted, and error bars represent standard deviations of 4 independent measurements. Error bars are much smaller than the symbol size for the lift measurements, but are visible for the drag measurements.



(a) With endplates - 2D airfoil



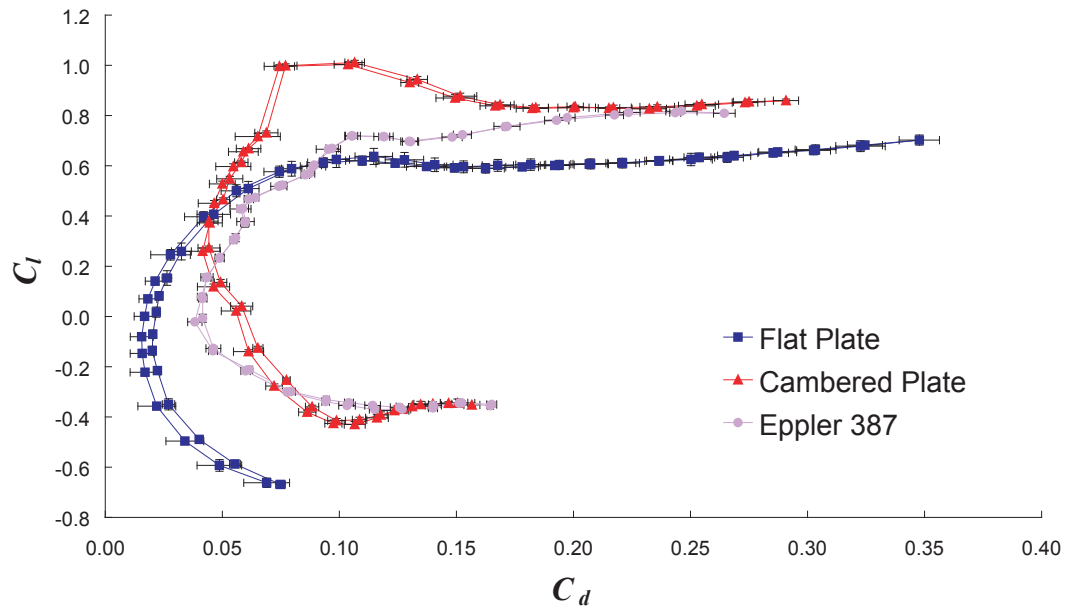
(b) Without endplates - aspect ratio 6 wing

Figure 5.2: Airfoil force coefficients at  $Re = 2 \times 10^4$   
 Data acquisition and uncertainty estimate techniques are similar to those in figure 5.1 but error bars are covered by the symbols for both the lift and the drag data.

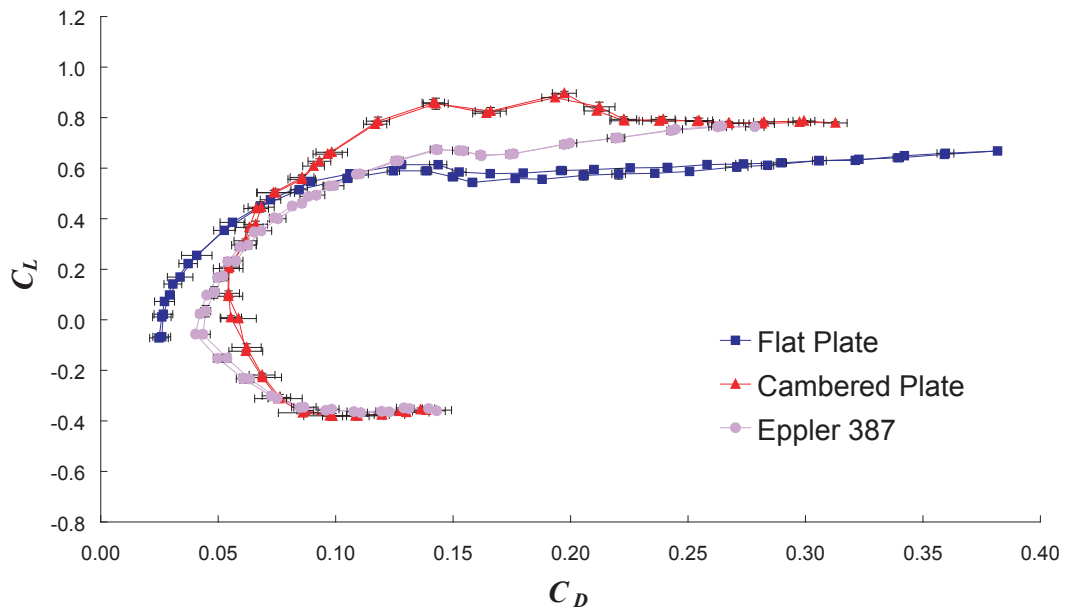
was not. Also, the E387 airfoil is a championship sail plane airfoil, and sail planes operate at the relatively low Re of 500,000. The flat plate airfoil also attains higher  $C_L$  than the E387 airfoil near  $\alpha = 6^\circ$  for the lower Re. This is another example of how thick cambered airfoils do not produce much lift at low Re, while thin airfoils (even if they are uncambered) start to produce higher  $C_L$ . Another observation that can be made is the change in the lift and drag curve slopes that occur for the cambered airfoil in the  $5^\circ < \alpha < 10^\circ$  range. A change in lift or drag curve slope is often related to a sudden qualitative change in the flow around the wing.

The drag polar is plotted in figures 5.3 and 5.4 and the lift-to-drag ratio ( $L/D$ ) is plotted in figures 5.5, and 5.6. In figure 5.3(a), the cambered plate produces approximately twice as much lift as the Eppler 387 for  $C_D = 0.8$ . This effect is only present for the 2D case. At the higher Re (figure 5.4(b)), the Eppler 387 achieves a minimum  $C_D$  that is half the cambered plate's minimum  $C_D$ .

The lift-to-drag ratio plots reveal that at the lower Re (figure 5.5) the flat plate airfoil has a higher  $L/D$  than the Eppler 387. Relating this result to the lift and drag curves of figure 5.1 shows that the higher  $L/D$  is primarily caused by a lower drag at  $\alpha = 4^\circ$  and not by the production of more lift. The other  $L/D$  plots (figure 5.6) show that the cambered plate airfoil has a discontinuity at about  $\alpha = 7^\circ$ , and it seems to increase in severity as the Re and AR increase. At the higher Re, the Eppler 387 has higher  $L/D$  than the flat plate airfoil, and in 3D is very similar to the cambered plate airfoil.

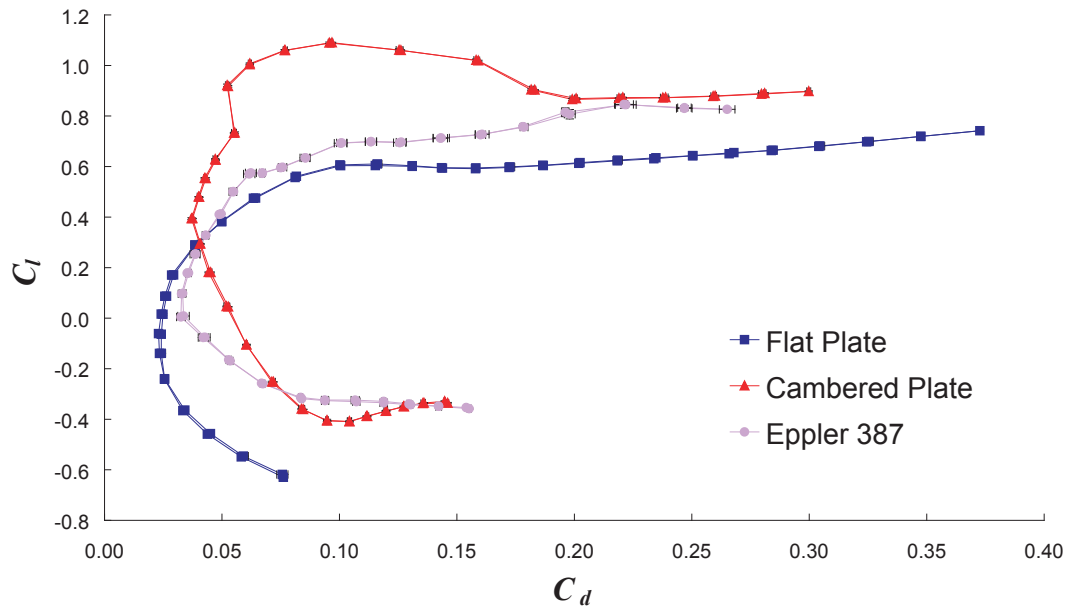


(a) With endplates - 2D airfoil

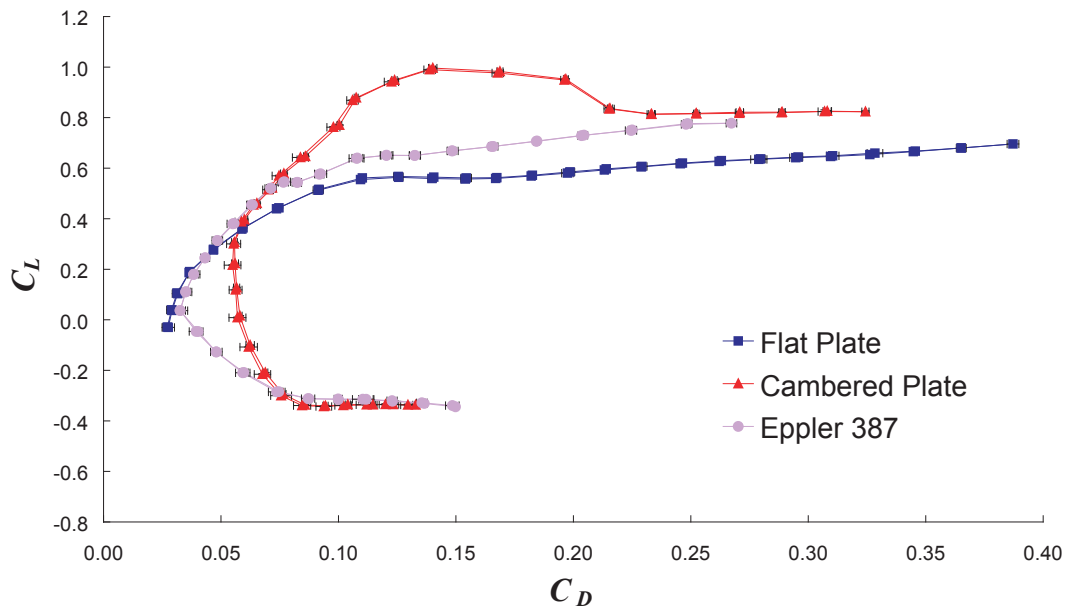


(b) Without endplates - aspect ratio 6 wing

Figure 5.3: Drag polar at  $Re = 1 \times 10^4$   
The drag polar of data plotted in figure 5.1.

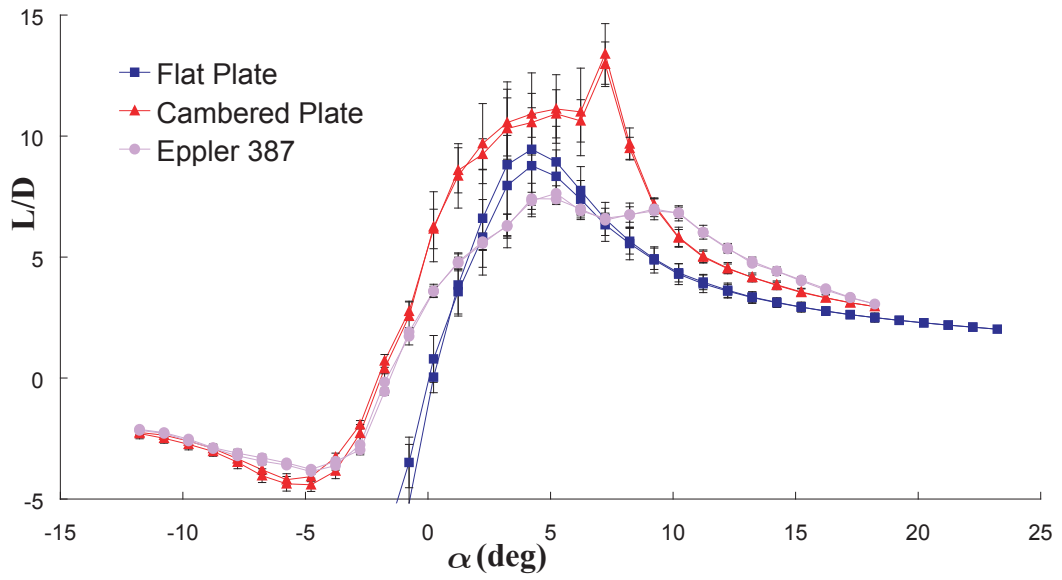


(a) With endplates - 2D airfoil

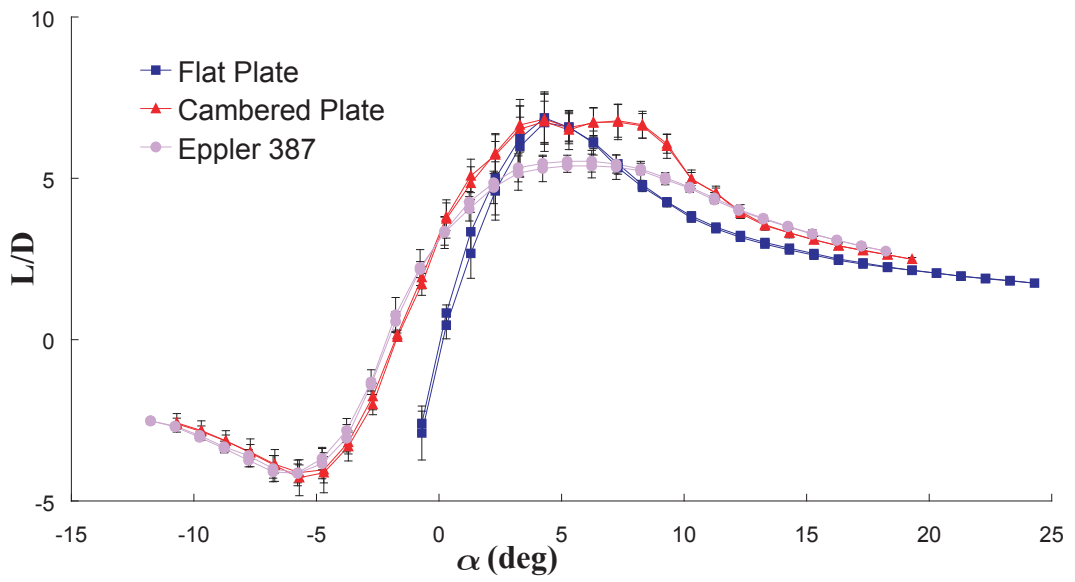


(b) Without endplates - aspect ratio 6 wing

Figure 5.4: Drag polar at  $Re = 2 \times 10^4$   
The drag polar of data plotted in figure 5.2.

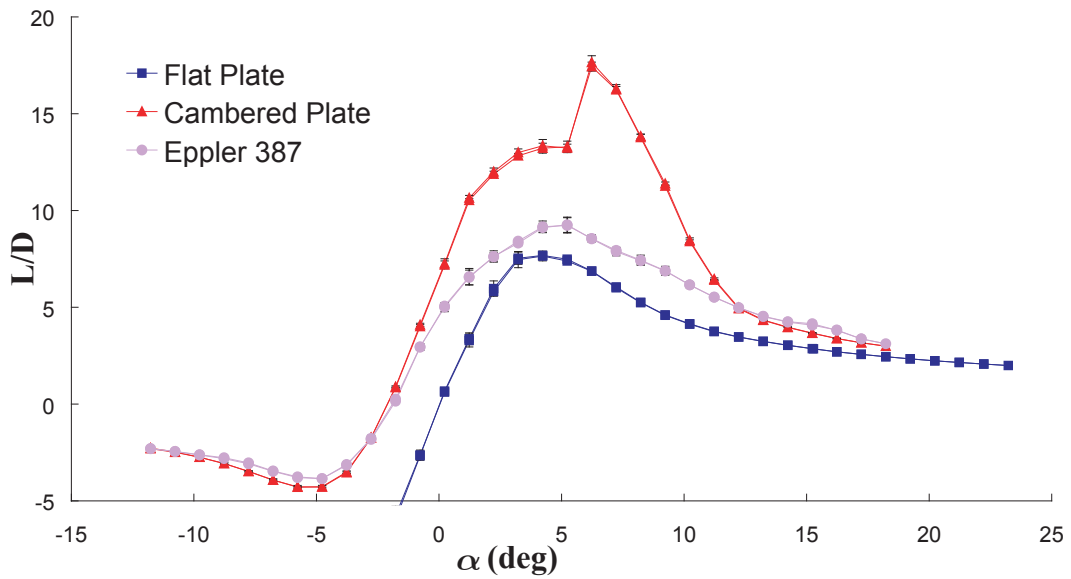


(a) With endplates - 2D airfoil

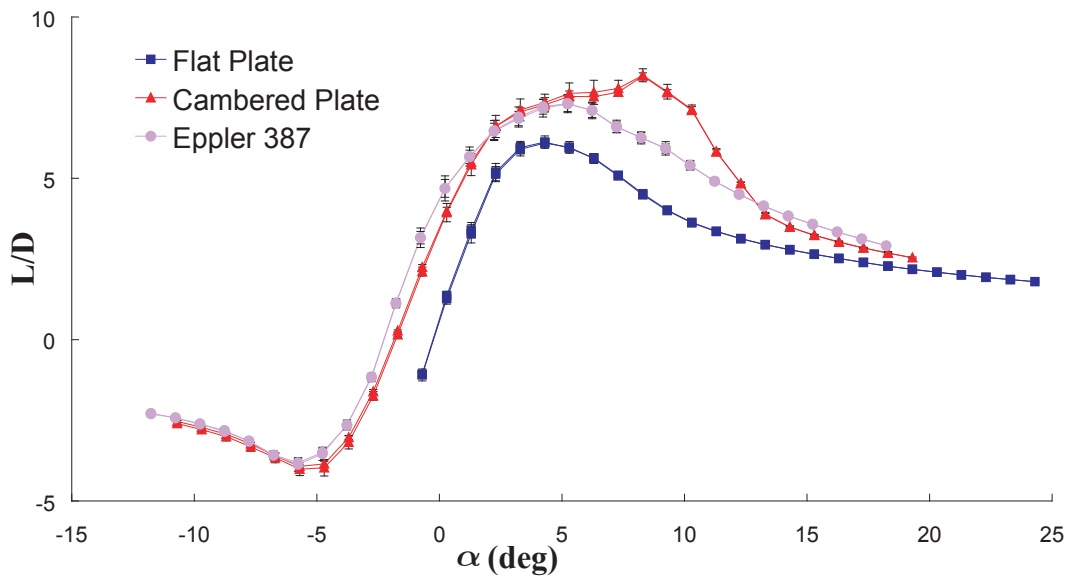


(b) Without endplates - aspect ratio 6 wing

Figure 5.5: Lift-to-drag ratio at  $Re = 1 \times 10^4$   
 The lift-to-drag ratio of data plotted in figure 5.1.



(a) With endplates - 2D airfoil



(b) Without endplates - aspect ratio 6 wing

Figure 5.6: Lift-to-drag ratio at  $Re = 2 \times 10^4$   
 The lift-to-drag ratio of data plotted in figure 5.2.

## 5.1.2 Comparison with External Sources

The force measurements for the flat plate airfoil can be compared with the literature. Figure 5.7 is a plot of all literature results from studies of flat plate lift and drag at  $Re < 5 \times 10^4$ . As  $Re$  and  $AR$  increase, the  $C_L$  increases and the  $C_D$  decreases. Mueller's results show this except for the  $C_L$  measurements at a few  $\alpha$ . Schmitz's results show this at  $\alpha > 5^\circ$ , and below this his measurements most likely have large uncertainty. Selig's results are difficult to interpret due to their small  $\alpha$  and  $Re$  range, but they generally exhibit the expected trends. When comparing results from different researchers, the only data that is contrary to the expected trends is Schmitz's results, as his two lowest  $Re$  have too large of  $C_L$  while his highest  $Re$  has too large of  $C_D$ . Again, Schmitz's results are likely have large uncertainty due to the relatively poor resolution of his force balance.

Since the Laitone results were conducted at an  $Re$  closest to the present experiments, figure 5.8 is a comparison between them. The measurements are in agreement, and the present experiments follow the expected trends for changing  $Re$  and  $AR$ . However, Laitone's  $C_L$  results have a smooth increase to the maximum, while the present experiments exhibit a change in slope at about  $\alpha = 3^\circ$ .

A comparison of the flat plate drag measurements can be made at  $\alpha = 0^\circ$  because there is an analytic expression for the drag of a flat plate at zero incidence and at various  $Re$  can be derived using the Blasius boundary layer. Figure 5.9 is a plot of  $C_D$  at  $\alpha = 0^\circ$  versus  $Re$ , and the experimental results of Schmitz, Selig, Mueller, and Laitone have all been plotted. Additionally, the computational results of Mittal et al are also plotted here. The Schmitz measurements were made at 3 different  $Re$  for 2D airfoils by using end-plates. The Selig measurements are similar, but at different values of  $Re$ . The Mueller measurements are at one value of  $Re$ , but for 3 different values of  $AR$  (inf, 6, and 2). The Laitone measurement is only at one  $Re$ , but is closest to the present measurements

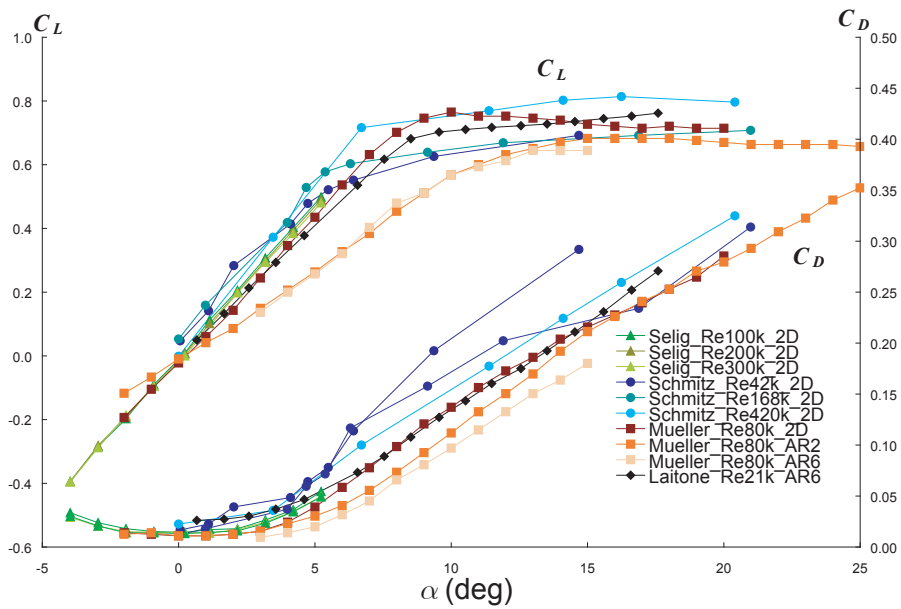


Figure 5.7: Flat plate polars from literature

Drag polars for a flat plate airfoil at various Re and AR from different facilities are compared. Most likely, the only researcher that does not follow the expected trend is Schmitz, and his uncertainty would be large due to poor resolution of his force balance.

and is in good agreement with them. The Mittal computations at first seem rather high compared with the present measurements, but the geometry used had a round trailing edge, which would cause more separation and increased drag due to pressure. Hence, when the pressure drag is eliminated and only the shear drag is considered, the computations are in good agreement with the present measurements. All of these results are compared with the drag of a Blasius boundary layer on top of an infinitely thin flat plate with  $\alpha = 0^\circ$ . At low Re, the measurements and computations are in good agreement with the Blasius boundary layer calculations, but at high Re there is significant disagreement. This may be due to the transition of the boundary layer, as the Blasius prediction should hold when the boundary layer is laminar, but as Re increases, the boundary layer should transition and become turbulent.

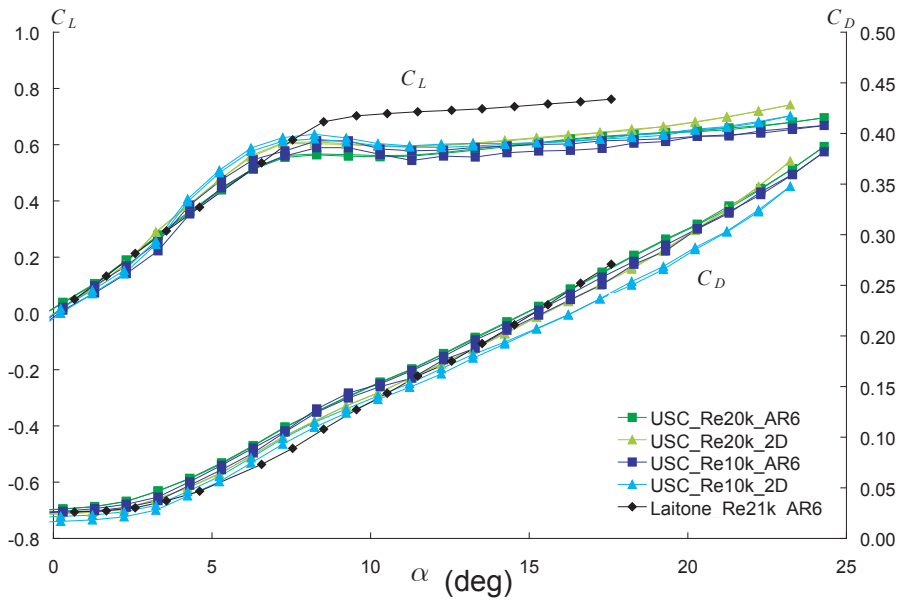


Figure 5.8: Flat plate polar comparison

Drag polar for a flat plate from Laitone is compared with the present experiments, and they seem to be in reasonable agreement. The change in slope at  $\alpha = 4^\circ$  will be discussed later.

Figure 5.10 is a plot of measurements made by Schmitz, Mueller, and Laitone for cambered plate airfoils at various Re and AR. Generally, the results of an individual researcher is consistent with the expectations that as Re increases and AR increases, the  $C_L$  increases and the  $C_D$  decreases. Comparison of one researcher's results with another is difficult because the geometries used were not the same. Laitone worked with a geometry similar to the present study, a 5% circular arc cambered plate. Mueller was also similar, but the camber was 4% of the chord. Schmitz's cambered plate had a maximum camber of 5.8% located at 40% of the chord, but no precise definition of the airfoil coordinates could be found.

Some comparison of these results could be useful. For instance, Mueller's (4% camber) 2D results for  $C_L$  at Re=60k are below Schmitz's (5.8% camber) 2D results at Re=42k. Thus, the 1.8% higher camber produces more additional lift than the lift lost

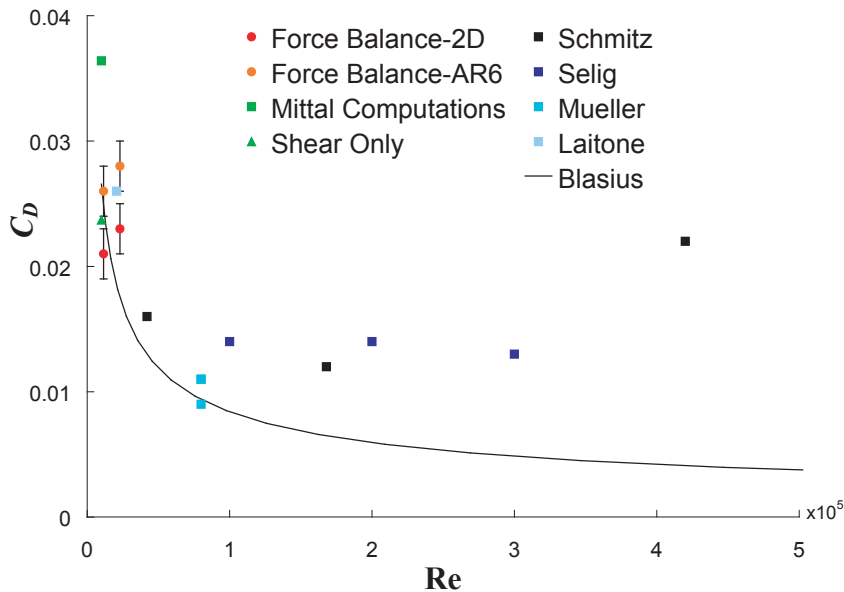


Figure 5.9: Flat plate drag coefficient at zero incidence

The drag produced by a Blasius boundary layer is plotted as the theoretical line, while the previous experimental measurements of Selig, Schmitz, Mueller and Laitone are plotted as blue square symbols. The present measurements are plotted as Force Balance data with circle symbols. The Mittal Computations are computational results produced by Mittal et al, while the shear only data point is when the computations remove the pressure drag and have only the shear component. Since the computational geometry had a rounded trailing edge, the pressure drag is expected to be much greater than in the present measurements which had a sharp tapered trailing edge.

by the 18k decrease in Re. Mueller's (4% camber) AR=6 results for  $C_L$  at Re=60k is also in disagreement with Laitone's (5% camber) AR=6 results at Re = 20k. Again, the additional lift gained by increased camber is larger in magnitude than the lift lost by the decrease in Re. Similar patterns can be seen in the  $C_D$  curves, but as the literature rarely supplied uncertainty estimates, it is difficult to determine how significant the drag disagreements are.

Since the results of Laitone are the closest in Re to the current results, a comparison of them is shown in figure 5.11. The comparison reveals quite good agreement for the

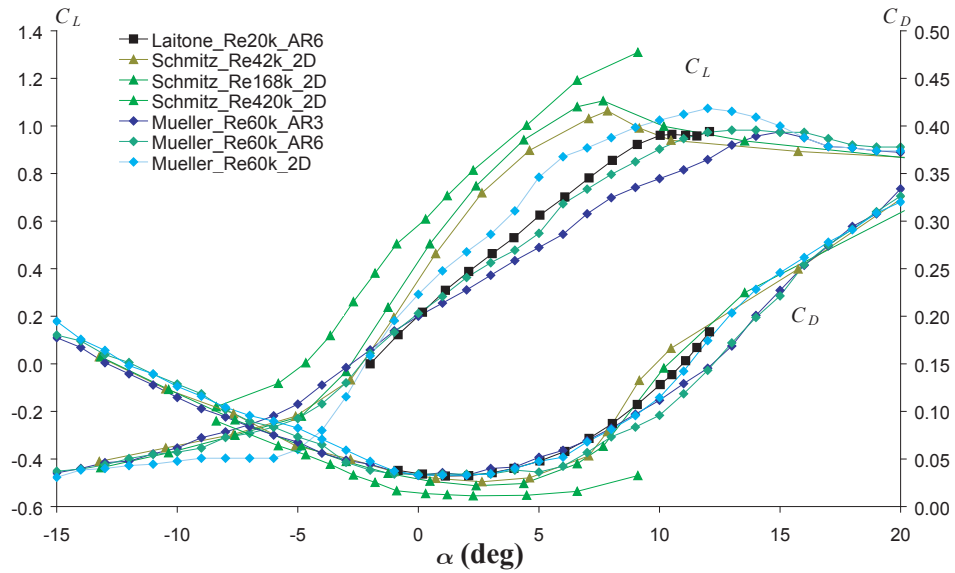


Figure 5.10: Cambered plate results from literature

Lift and drag coefficients from Laitone, Schmitz, and Mueller are plotted as a function of  $\alpha$ . Individual researchers results are consistent with expected general trends, but comparison between researchers shows some inconsistency.

$C_L$  measurements at all  $\alpha$  except near  $\alpha = 6^\circ$  where Laitone's results increase smoothly to the maximum, while the current results have a discontinuity in the slope at about  $\alpha = 6^\circ$ . The comparison of  $C_D$  measurements is not in as good agreement, as the present measurements are sometimes nearly twice the measurements of Laitone. These facts are consistent with the fact that Laitone's wind tunnel turbulence was much larger than the wind tunnel used for the present measurements, and might be the explanation. Other explanations include different model roughnesses or geometries.

The difference between the drag of a two-dimensional airfoil with infinite AR, and that of a three-dimensional wing with finite AR can be related theoretically using lifting line theory. In this theory, the 2D drag ( $C_{d,i}$ ) is related to the 3D drag ( $C_D$ ) by the induced drag ( $C_{D,i}$ ) such that

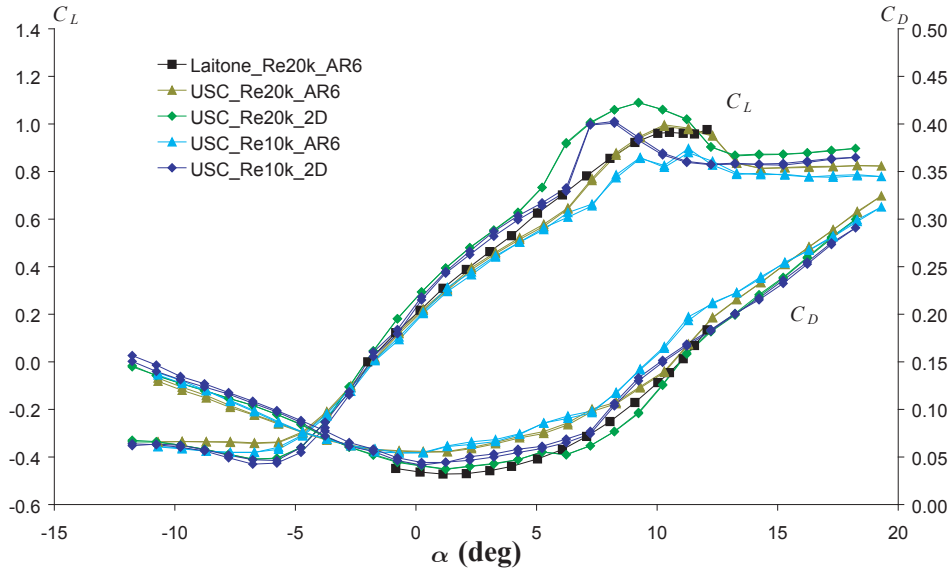
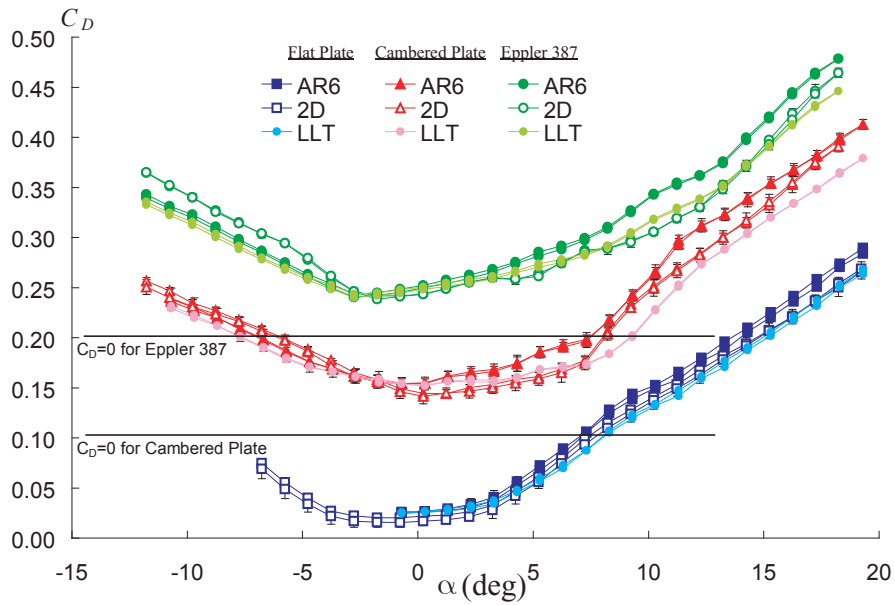


Figure 5.11: Cambered plate at low Re  
Laitone's measurements at Re=20k are compared with the present measurements. The  $C_L$  measurements are in good agreement, but the  $C_D$  results are quite different.

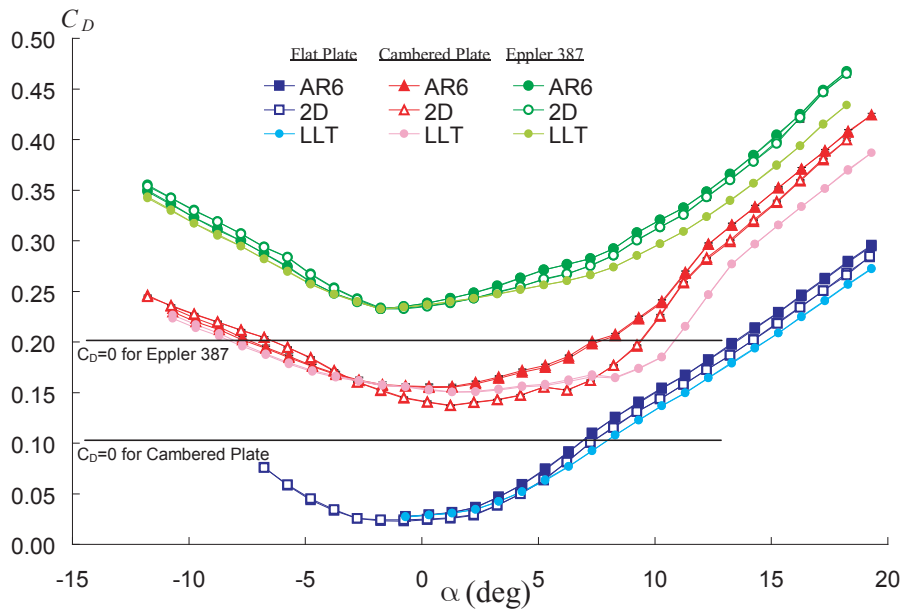
$$C_D = C_d + C_{d,i} \quad (5.1)$$

$$C_{d,i} = \frac{C_L^2}{\pi e AR} \quad (5.2)$$

where  $e$  is the Oswald efficiency factor and depends on the span-wise distribution of  $C_l$  on the wing. This theory works well at high Re, but it is unclear whether it applies at these low Re. Using the inviscid formulation of lifting line theory, a rectangular wing has  $e = 0.96$ . Using  $AR = 6$ , and the  $C_L$  from each  $\alpha$ , figure 5.12 applies lifting line theory to the present data for each airfoil shape and for both Re. It seems that the theory works reasonably well for the lower Re case (figure 5.12(a)), especially for the Eppler 387 and flat plate airfoils. The theory works with for the cambered plate airfoil at low  $\alpha$ , but doesn't work at  $\alpha > 7^\circ$ .



(a)  $Re = 1 \times 10^4$



(b)  $Re = 2 \times 10^4$

Figure 5.12: Lifting line theory

By subtracting the induced drag from the 3D drag, and comparing that to the 2D drag, the accuracy of lifting line theory at these  $Re$  can be evaluated. Lifting line theory is quite accurate for the flat plate and E387 airfoils at low  $Re$ , but at higher  $Re$  it is not as accurate. Each airfoil is shifted vertically by 0.1 to allow for easier comparison. 70

At the higher Re (figure 5.12(b)), lifting line theory overestimates the induced drag for each case. The flat plate case has the least disagreement, with the theoretical prediction actually being within the uncertainty estimates of the 2D measurements, but is consistently in the lower bound of the uncertainty. The Eppler 387 case has significant disagreement with the theory at  $\alpha > 5^\circ$ . For the cambered plate case, the theory works well up to about  $\alpha = 7^\circ$ , after which there is large disagreement.

These results are relatively independent of the value of  $e$  that is used. The inverse relation between induced drag ( $C_{d,i}$ ) and  $e$  means that as  $e$  gets smaller, the rate at which  $C_{d,i}$  changes with  $e$  is larger. Thus, for values of  $e$  from about 0.7 to about 1.0, the above conclusions are still consistent.

### 5.1.3 Separation point

The forces measured above are caused by the fluid moving around the wings. When the fluid motion changes, the forces change, and this can be demonstrated by using pictures of particles moving around the wing. This technique is used in DPIV experiments, and the results are typically used to measure the velocity field around the wing. However, the vectors of the velocity field are spatial averages of a number of pixels, and hence some structures of the flow are lost in the data processing. The smaller the structures, the more the processing will smear them out.

Figure 5.13 is a demonstration of one image of smoke particles surrounding the wing as they move around it. In the image, the wing's span is perpendicular to the image, and the upper surface of the wing is the white curved line in the center. The field is illuminated by a laser light sheet emitted from the top of the image, and hence the black region below the wing is the shadow caused by the wing blocking the laser. The flow is from left to right and it is the cambered plate airfoil with  $AR = 6$ ,  $Re = 2 \times 10^4$ , and  $\alpha = 6^\circ$ . The large image on the left is the original image, and is about 1000 x 1000

pixels, but has been reduced to fit on the page. The red region near the trailing edge has been represented in original detail in the small image on the right.

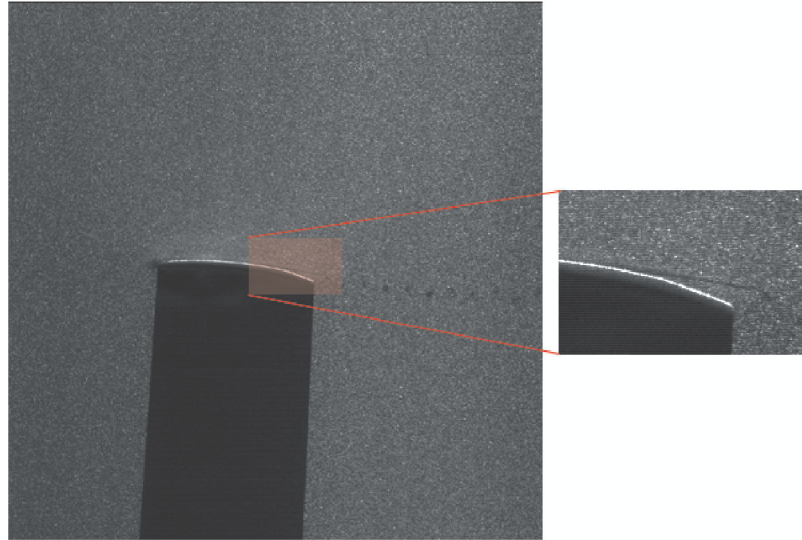


Figure 5.13: Separation line for cambered plate

An image of the cambered plate wing (span normal to page) with smoke particles surrounding the wing demonstrates the separation line. The white curved line in center of image is the upper surface, and the red region is shown in full resolution in small image on the right. The dark region is more apparent in the small image, and indicates the separation streakline where there are few particles because it is made up of the boundary layer flow. The image is for the cambered plate at  $Re = 2 \times 10^4$ ,  $AR = 6$ ,  $\alpha = 6^\circ$ , and at the mid-span ( $y = \frac{b}{2}$ ).

This image demonstrates a small scale structure that is undetectable by traditional PIV techniques, namely, the dark region emitted from the upper surface near the trailing edge. The dark region indicates the separation streakline. The reason the separation streakline appears as a dark region is that it intersects with the surface of the wing, and in the boundary layer near the surface, there are very few smoke particles. The dark region eventually breaks up due to the instability of the shear layer, and/or the interaction with the wake, depending on how close the separation point is to the trailing edge. Further

evidence that this dark region indicates the separation streakline is presented later in this chapter.

Since the separation streakline cannot be detected by PIV techniques, it must be measured from the raw images. This was done for each case, and at each angle of attack for which the dark region was clearly visible. The dark region was never visible in the flat plate case, but the cambered plate and Eppler 387 cases had easily identifiable dark regions, and very different characteristics as  $\alpha$  increased. To explain, figure 5.14 shows how the separation point location ( $x_s$ ) changes as  $\alpha$  is increased. The separation point is represented as a fraction of the chord ( $c$ ), and was measured by finding the intersection of the upper surface and the separation streakline, and projecting that onto the chord line, as shown in figure 5.15.

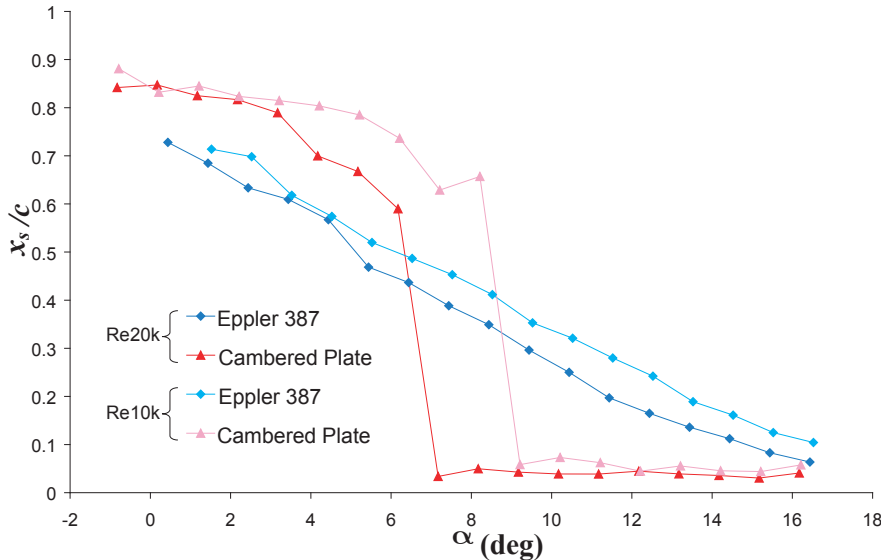


Figure 5.14: Separation point of cambered plate and Eppler 387  
 The separation point of the Eppler 387 and the cambered plate airfoil are plotted against  $\alpha$ . Both Re are plotted, and all plots are from the mid-span at the AR = 6 condition. The data acquisition is described in figure 5.15.

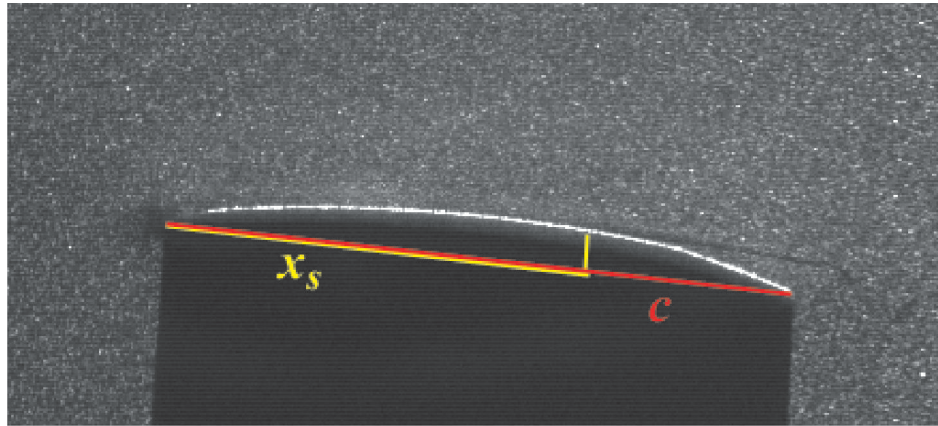


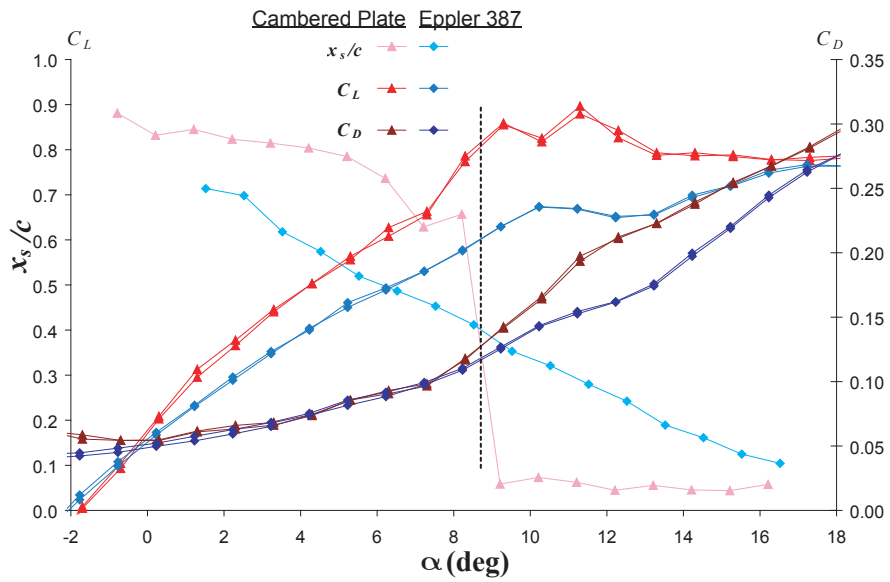
Figure 5.15: Method of measuring separation point

This image is the same as the image in figure 5.13, but at a greater magnification.

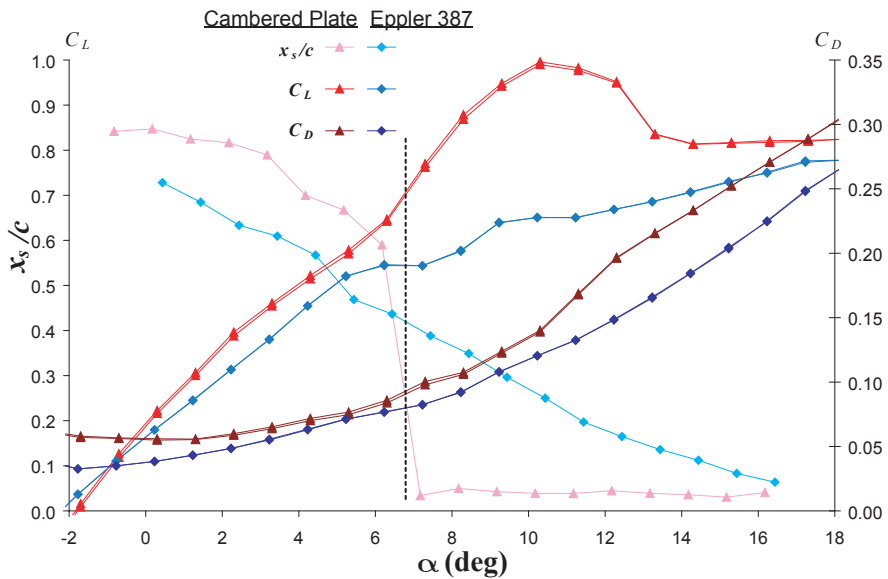
The separation point on the cambered plate suddenly moves to the leading edge as  $\alpha$  increases above a critical value, while for the Eppler 387 it gradually moves forward as  $\alpha$  increases. For both cases, the separation occurs closer to the leading edge at higher Re than it does at lower Re, and for the cambered plate the discontinuity occurs at  $\alpha = 7^\circ$  for the higher Re, but not until  $\alpha = 9^\circ$  for the lower Re. It is likely that the separation point at low Reynolds number is closer to the trailing edge because the boundary layer is thicker, and moves the minimum pressure point back.

The separation point location can be related to the force coefficients presented earlier. This comparison is made in figure 5.16 for both Re and at AR = 6. At the higher Re (figure 5.16(b)), the discontinuity in the separation point for the cambered plate is at the same  $\alpha$  as the sudden increase in  $C_L$ . There is not much change in  $C_D$  here, and the curves for the Eppler 387 are all smooth, with no significant discontinuities.

At the lower Re (figure 5.16(a)), the sudden change in separation point is more related to a sudden increase in  $C_D$  rather than  $C_L$ . The  $C_L$  increases  $1^\circ$  before the separation point moves forward. The reason for the difference remains unclear, but certainly it is related to the sensitivity to small changes in Re at these moderate values



(a)  $Re = 1 \times 10^4$



(b)  $Re = 2 \times 10^4$

Figure 5.16: Separation point related to forces

The changes in separation point are related to the changes in  $C_L$  and  $C_D$ . At the higher  $Re$ , the cambered plate's sudden change in separation point is related to the sudden increase in lift, while at the lower  $Re$ , it is more related to the sudden increase in drag. All data is for  $AR = 6$ .

of  $Re$ . At larger  $Re$ , a change of  $\Delta Re = 10,000$  would yield no measurable difference in separation point or forces. However, at this  $Re$ , where the boundary layer is laminar over much of the wing, but the stability of that boundary layer is very sensitive to the  $Re$ , and small changes in the stability can cause large changes in the fluid motion around the wing, and hence on the forces generated by the wing.

## 5.2 Laminar Separation Bubble

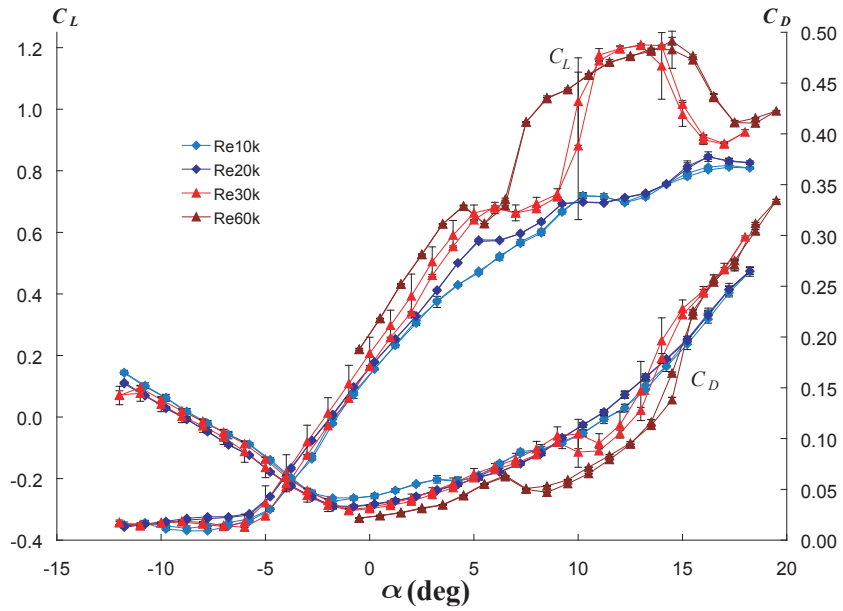
### 5.2.1 Force Balance Measurements

Lift and drag measurements have been made for the E387 airfoil at  $Re = 1, 2, 3,$  and  $6 \times 10^4$ . The measurements were made at  $-10^\circ < \alpha < 20^\circ$  in  $1^\circ$  increments. The lowest two  $Re$  were obtained with the smaller wing (3.5 cm chord), while the highest two  $Re$  were obtained with the larger wing (9 cm chord). The results for the lower two  $Re$  have already been presented and compared with the flat plate and cambered plate in the previous section, but will be presented here as well for comparison purposes. Plots of lift and drag coefficient vs  $\alpha$  are shown in figure 5.17(a). For this data, end plates were used to approximate 2D flow conditions. Figure 5.17(b) shows the force coefficients for the  $AR = 6$  case. In both plots, hysteresis was investigated by making measurements while increasing and decreasing  $\alpha$ . The uncertainty was estimated in the same way as described in the previous section. Error bars are plotted to represent this uncertainty, but they are typically smaller than the symbol size.

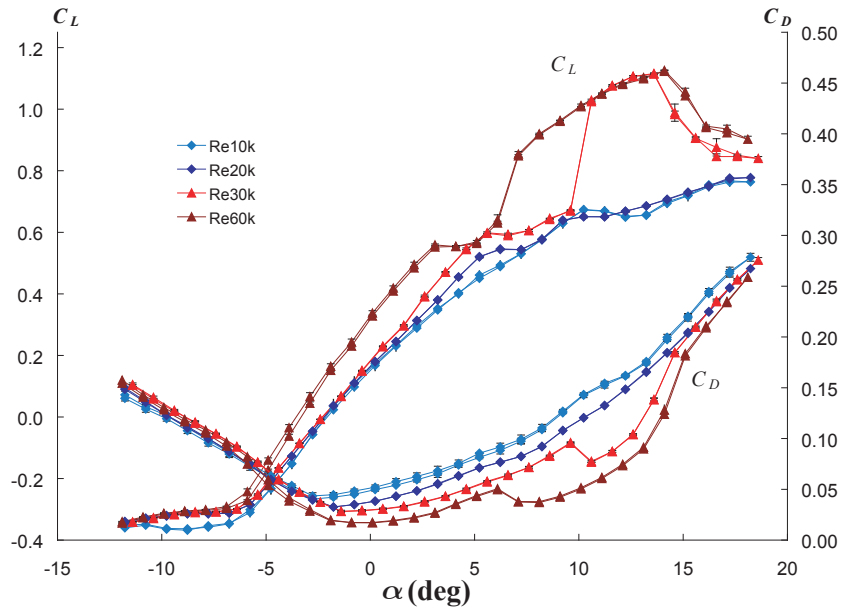
Both the 2D and the aspect ratio 6 data show the sudden lift increase and drag decrease measured by other researchers using the E387 at  $Re = 6 \times 10^4$ . As the  $Re$  decreases to  $3 \times 10^4$ , the magnitude of the drag decrease goes down, and at  $Re = 2 \times 10^4$  the drag is monotonic with  $\alpha$  and the discontinuities in  $C_L$  have vanished.

Plots of the lift-to-drag ratio for the above cases is shown in figure 5.18, where a gradual improvement in efficiency can be seen as  $Re$  increases. The maximum lift-to-drag ratio increases rapidly with  $Re$ , consistent with the generalization of McMasters (see figure 1.2). [24]

The drag polars for these cases is plotted in figure 5.19. In both the 2D and 3D case, the discontinuity in  $C_L$  and  $C_D$  can again be seen to grow as  $Re$  increases. In the 3D



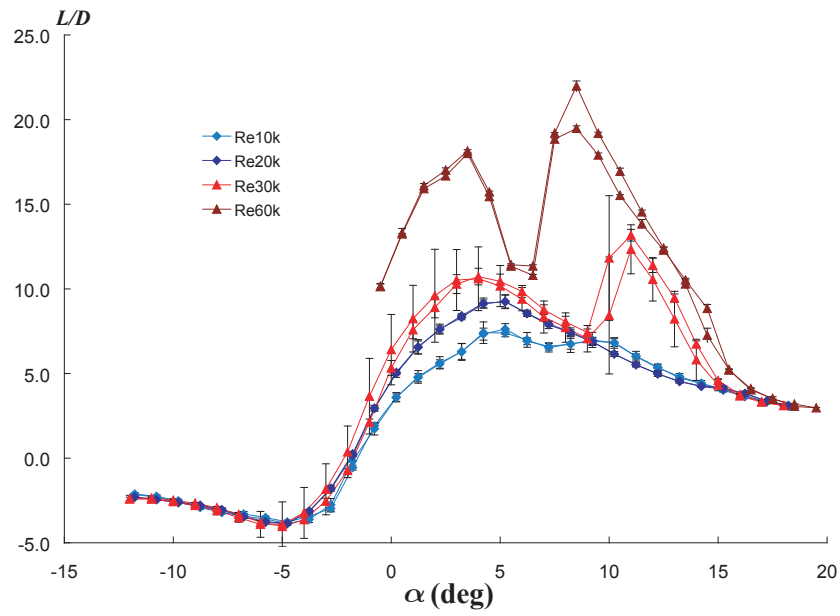
(a) With endplates - 2D airfoil



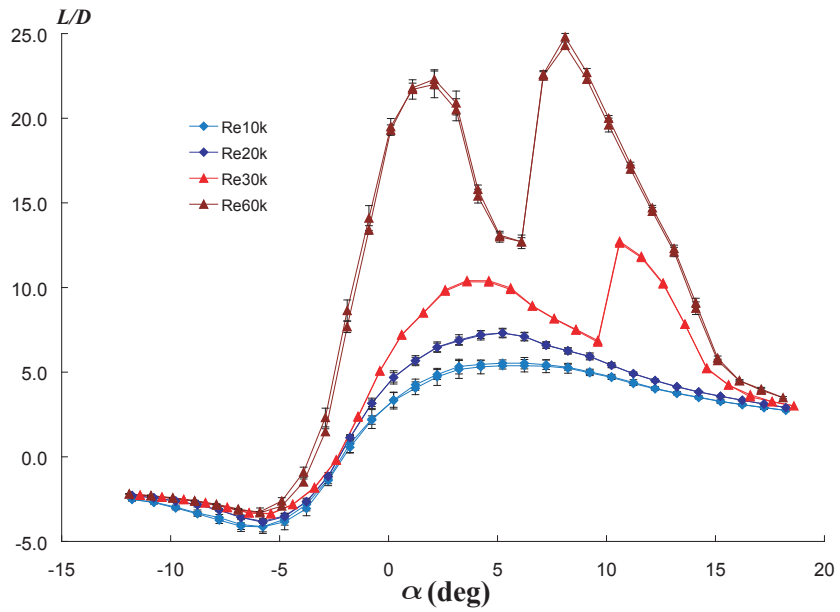
(b) Without endplates - aspect ratio 6 wing

Figure 5.17: Eppler 387 forces

The lift and drag coefficient is plotted against  $\alpha$  for the E387 airfoil. Data was taken for both increasing and decreasing  $\alpha$ . The uncertainty is plotted with error bars, but is typically smaller than the symbols.



(a) With endplates - 2D airfoil



(b) Without endplates - aspect ratio 6 wing

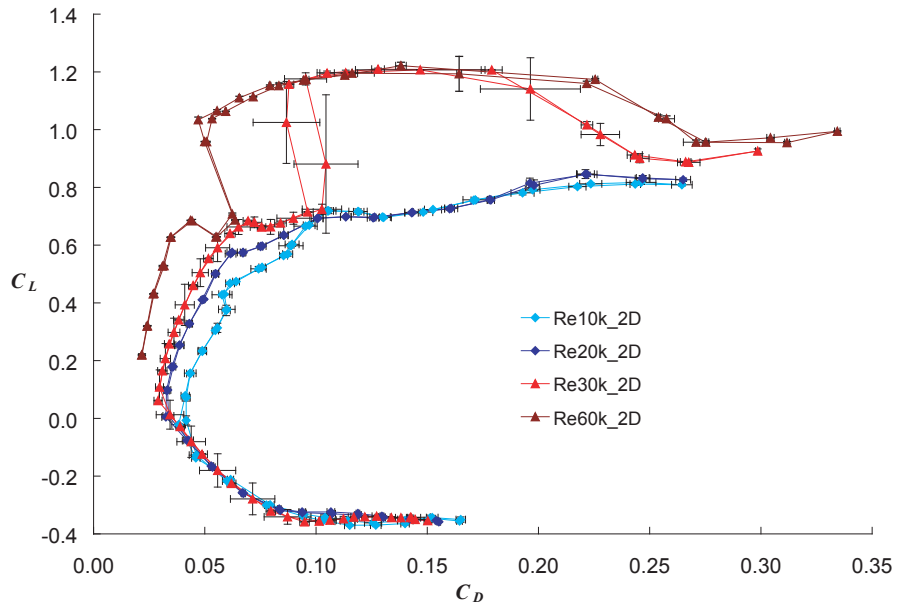
Figure 5.18: Eppler 387 lift-to-drag ratio  
 The lift-to-drag ratio of the data plotted in figure 5.17. Uncertainty estimates are plotted with error bars.

case, it is clear that the minimum  $C_D$  for the highest Re is about half of that of the lowest Re.

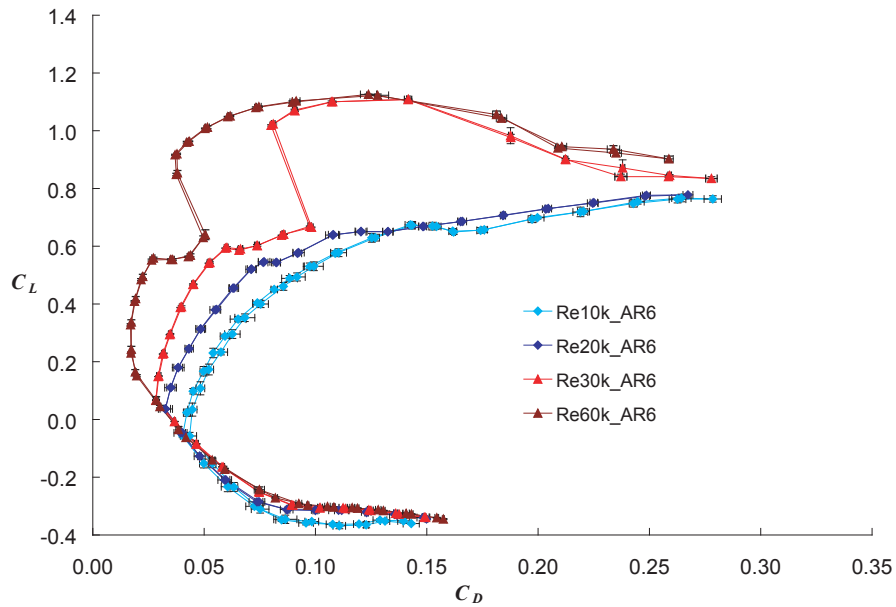
In figures 5.17, 5.18, and 5.19 the 2D data has much larger uncertainty and a less smooth change as  $\alpha$  and Re increases. This is most likely due to the effect of the end plates, as it is possible that the wings touched the end plates slightly during some parts of some tests, and not during others. In most wind tunnels, the wing spans the entire test section, and hence the endplates are closer to the wall than the present experiments and can be made more rigid. Also, the sting that connects the wing to the force balance is shorter, and has less vibration during testing. For these reasons, the 2D data from the present experiments are not as reliable as the 3D data, and some future results will only have data for the 3D case.

One aspect of the 2D data which will be discussed in more detail later and is not believed to be an effect of touching the end plates, is the hysteresis seen at  $Re = 3 \times 10^4$  and  $\alpha = 10^\circ$ . The difference in  $C_L$  between the increasing and decreasing  $\alpha$  curves, and the large uncertainty, indicates that this is hysteresis similar to that reported by Grundy et al [11].

In comparing the results at the various Re, it is important to keep in mind that these results come from using 2 different wings. One has a 3.5 cm chord and has been sanded and painted, while the other has a 9 cm chord and bare aluminum out of the mill and is rather rough. While the similarities between the two (such as the way the  $C_L$  curve for the Re=30k case is similar in shape to the Re=20k case near  $\alpha = 5^\circ$ , and how they merge near  $\alpha = 9^\circ$ ), it should be remembered that they have nominally the same geometry, but not exactly the same. Also, the roughness is known to cause large differences in lift and drag at this range of Re, so the similarities might be a coincidence, or as a statement about how nominally similar shapes will have strong similarities in the force  $C_L$  and  $C_D$



(a) With endplates - 2D airfoil



(b) Without endplates - aspect ratio 6 wing

Figure 5.19: Eppler 387 drag polar

The drag polar for the Eppler 387 demonstrates the gradual progression of discontinuities as the Re increases. In addition, the difference in drag between the different Re cases is more apparent.

curves despite the strong dependence on Re. Or, viewed a different way, that it is a rapid change with Re, but not a sudden change at a critical Re.

### 5.2.2 Comparison with External Sources

Comparing the 2D and 3D results will test how applicable lifting line theory is for this airfoil at this range of Re. In figure 5.20, the 2D and 3D polars are plotted, and shows that for the two largest Re, the 2D airfoil has a larger maximum  $C_L$ . This is expected as lift should increase as AR increases. However, drag should decrease as AR increases, and this does not happen for the two largest Re. In the range  $0 < C_L < 0.6$ , the two lowest Re have the expected trend: the 2D airfoil has lower  $C_D$  than the 3D wing. However, at  $Re = 3 \times 10^4$ , the  $C_D$  is nearly the same in this range of  $C_L$ . Moving to  $Re = 6 \times 10^4$ , the trend is reversed, and the 2D case actually has more drag than the 3D case.

Plotting the 2D and 3D drag coefficients is done in figure 5.21. This is similar to figure 5.12 where each increase in Re is shifted vertically by 0.1 from the previous Re. Again, the 3D results have the induced drag ( $C_{D,i}$ ) subtracted from them for comparison with the 2D results (see equation 5.2). The better they agree, the more applicable lifting line theory will be for that case.

As Re increases, the applicability of lifting line theory decreases. Again, at  $Re=60k$ , the general trend that lifting line theory predicts (that 3D drag is larger than 2D drag) is reversed. The reason for this reversal has yet to be fully explained, but it is clear that there are some beneficial 3-dimensional effects for this airfoil at this Re. Perhaps the spanwise flow and wing-tip vortices delays separation, hence reducing the pressure drag. This was not investigated in the current study, but is considered as a possibility for future research.

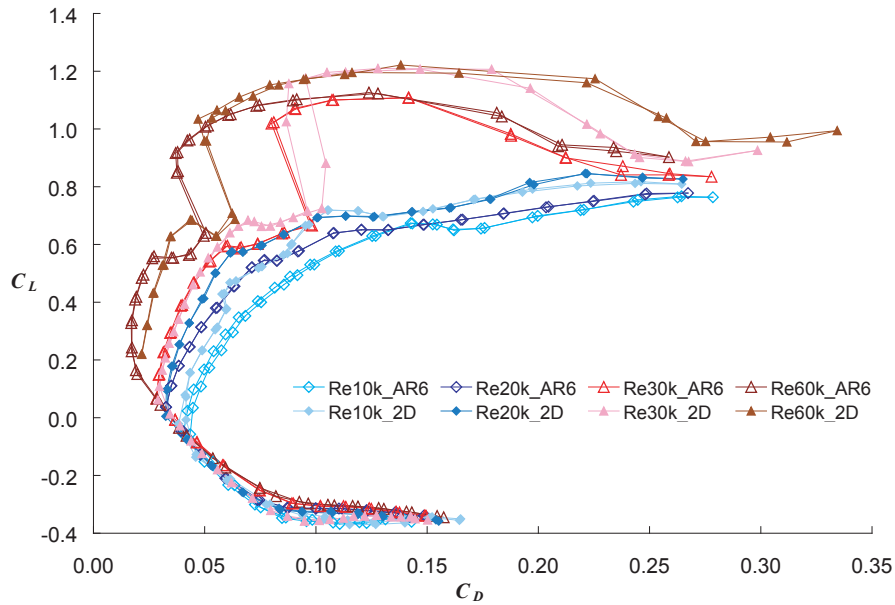


Figure 5.20: Eppler 387 drag polar for 2D and 3D

The  $C_L$  plotted against the  $C_D$  can help identify trends as AR increases. At moderate  $C_L$  (0.2-0.8) the drag behavior is consistent with lifting line theory for the lower Re, while at the higher Re, the behavior is opposite the trend predicted by lifting line theory. For the higher Re at the higher  $C_L$  (0.8-1.4), the lift behaves as expected, with the higher AR achieving higher maximum  $C_L$ .

As mentioned in section 5.2.1, the 2D results for the Eppler 387 at Re=30k show signs of hysteresis near  $\alpha = 10^\circ$ . This hysteresis was studied with greater detail by making measurements in  $0.1^\circ$  increments. In figure 5.22, 2D and 3D measurements of the E387 at Re=30k are plotted along with the results of the higher  $\alpha$  resolution measurements, which were conducted for the 3D condition. The higher resolution measurements made also found evidence for hysteresis, but at  $1^\circ$  higher  $\alpha$ . This difference is believed to be significant as the uncertainty in  $\alpha$  is approximately  $0.1^\circ$ . The hysteresis occurs over a  $0.4^\circ$  range of  $\alpha$ , and proceeds in a counter-clockwise direction.

There is some discrepancy between the higher resolution measurements and the lower resolution measurements. The increasing  $\alpha$  path begins to rise at about  $\alpha = 10.8^\circ$

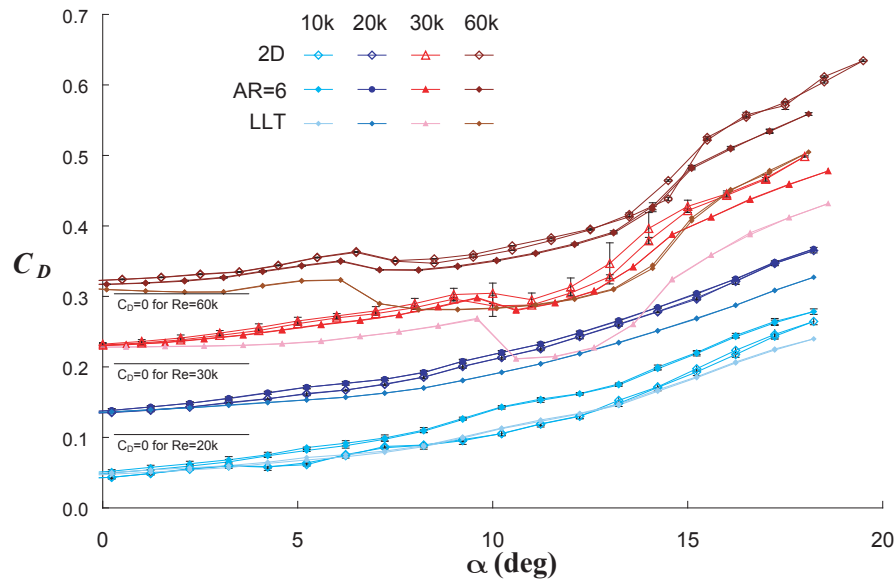


Figure 5.21: Lifting line theory - Eppler 387

The drag coefficient of the E387 at each of the four Re and in 2D and 3D conditions is plotted against  $\alpha$ . This is similar to figure 5.12 with each Re shifted vertically by 0.1 for easier comparison. Lifting line theory can be applied for this wing at the lowest Re with reasonable accuracy, but as Re increases, the accuracy of lifting line theory decreases.

and the decreasing  $\alpha$  path falls at about  $\alpha = 10.4^\circ$ . However, in the lower resolution measurement, the data point at  $\alpha = 10.5^\circ$  is consistently on the decreasing  $\alpha$  path, regardless of the direction  $\alpha$  is changing. Since this measurement is in the region of hysteresis, it is expected that it would demonstrate this hysteresis, similar to what is seen in the 2D case. The fact that it does not might be related to the step size, or vibrations in the model, or the step speed. Regardless of the reason, the hysteresis location seems dependent on exactly how the measurements are made.

The primary reason for making measurements up to  $\text{Re} = 6 \times 10^4$  is to compare the results to previous measurements. Figure 5.23 is a plot of the present 2D measurements, along with all previous measurements at  $\text{Re} = 6 \times 10^4$ . The present measurements are in reasonable agreement with the previous measurements, which have considerable scatter.

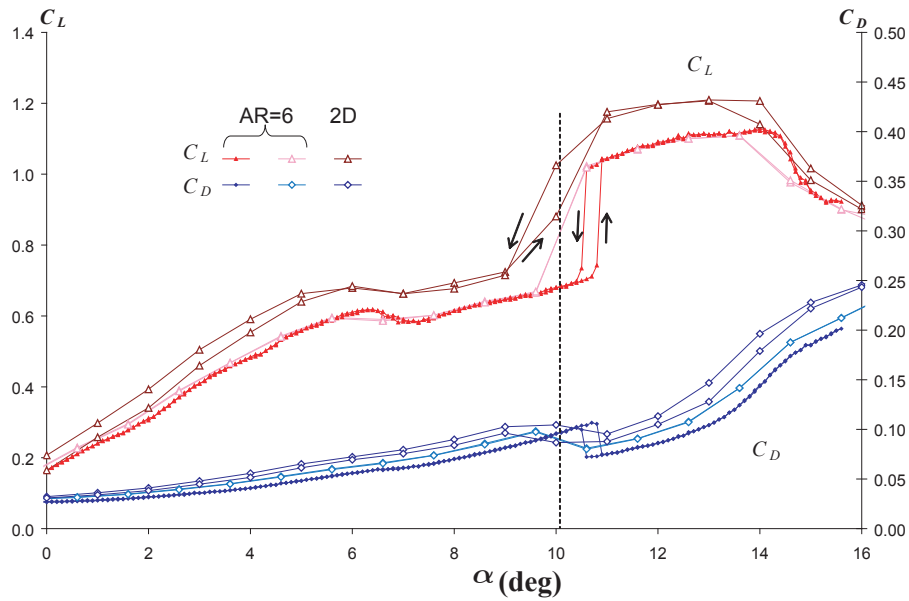


Figure 5.22: Eppler 387 hysteresis

Slight hysteresis was observed at  $Re=30k$  for the 2D case, so measurements were made for this  $Re$  at  $0.1^\circ$  increments in  $\alpha$ . The 3D case was used for these higher  $\alpha$  resolution measurements since they are more applicable to real slight systems. Hysteresis was observed, but only over a  $0.4^\circ$  range of  $\alpha$ .

At small negative values of  $C_L$ , there are no measurements for the present tests. At small positive values of  $C_L$ , the agreement is very good with the present measurements in the middle of previous measurements. In the drag increase region with moderate  $C_L$  values ( $C_L \approx 0.7$ ), the agreement is again quite good, with the present measurements surrounded by previous measurements. The present experiments have a lift decrease with increase in angle of attack at about  $C_L = 0.7$ , and this is rather different from previous results. Out of the 5 facilities, only the experiments conducted at Langley Research Center by McGhee et al have a similar decrease in  $C_L$ . [22] [23]

At higher values of  $C_L$ , the agreement between the present results and the previous results is not as good. They are qualitatively similar, because the lift rapidly increases and the drag decreases over an increase of about  $2^\circ$  in  $\alpha$ , but the amount of lift increase

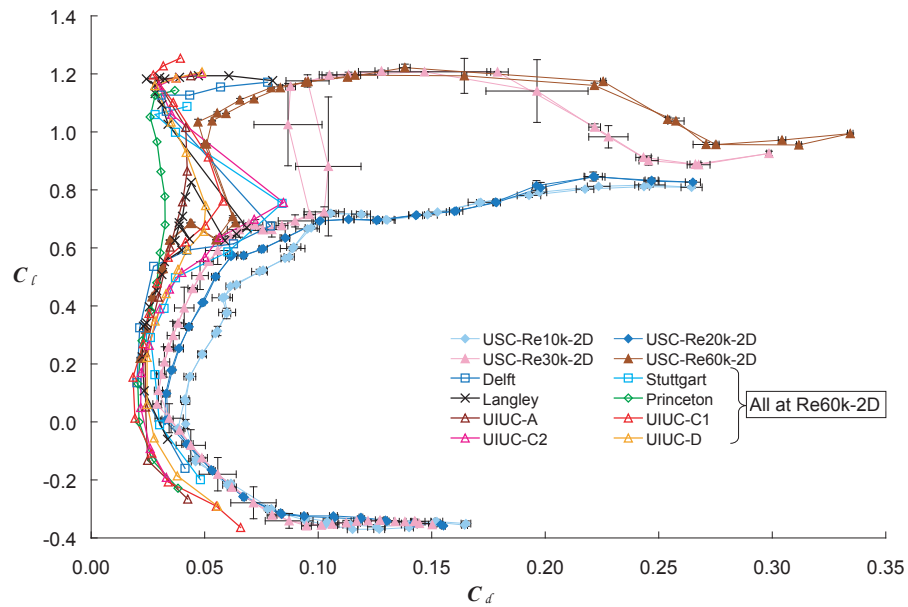


Figure 5.23: Eppler 387 drag polar for 2D and all previous 60k measurements. The present measurements are compared with all previous measurements at  $Re=60k$ . The present measurements at  $Re=60k$  are in reasonable agreement with previous measurements at low  $C_L$  and in the region of drag increase at moderate  $C_L$ , but at high  $C_L$  the present experiments are different. This is most likely caused by different free-stream turbulence levels.

and drag decreases is smaller than has been previously found. The best explanation for this is the lower freestream turbulence in the present experiments, but this will be discussed in greater detail in the conclusions chapter.

The most recent set of measurements from figure 5.23 are those taken at the University of Illinois (Urbana-Champaign) by Selig et al, and they are labeled UIUC [34]. The most recent measurements made by this group are labeled UIUC-D in the figure, and the measurements were at the lowest  $Re$  of a series of measurements made by this group. In figure 5.24, the other measurements made by this group are plotted along with the present measurements to show a gradual trend as the Eppler 387 passes through its critical  $Re$  range.

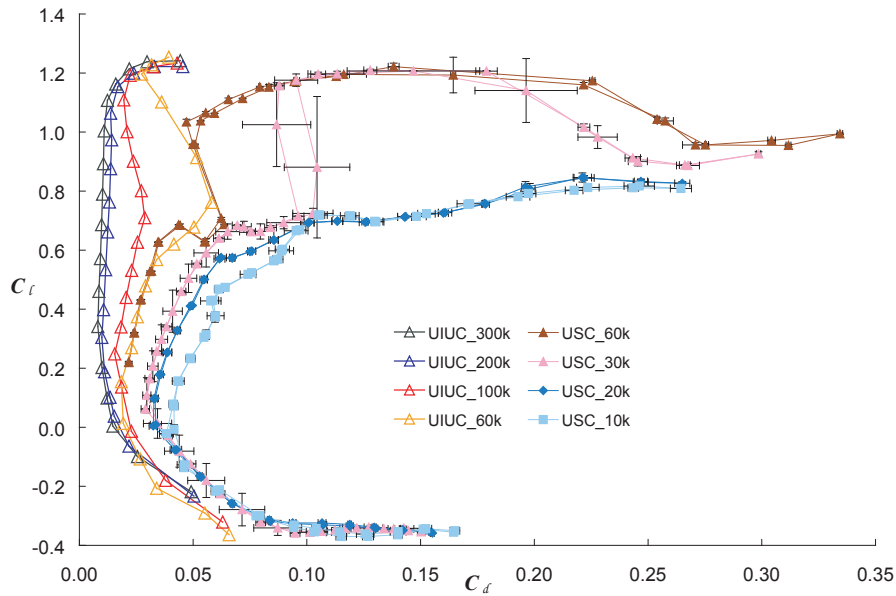


Figure 5.24: Eppler 387 drag polar for 2D and UIUC

The present measurements are compared with measurements made at University of Illinois Urbana-Champaign (UIUC) by Lyon et al. [20]

According to Selig [37], the drag increase at moderate lift coefficients seen at  $Re = 6 \times 10^4$  is caused by a large laminar separation bubble (LSB) with turbulent reattachment near the trailing edge. The subsequent drag decrease at higher  $\alpha$  is caused by the bubble bursting and becoming very small, and turbulent reattachment occurring near the leading edge. However, there is rather limited evidence for this conclusion, and in light of the present measurements at much lower  $Re$ , a new possible interpretation is offered. *The drag increase at moderate lift coefficients is caused by simple laminar separation with no transition to turbulence and no reattachment. The subsequent drag decrease at higher  $\alpha$  is caused by the formation of an LSB.*

### 5.2.3 Flow Field Measurements

The above hypothesis was proven by measuring the flow field around the wing, at  $Re = 3,6 \times 10^4$  and at even values of  $\alpha$  between 0 and 16. The PIV technique described in section 4.3.2 was used, and figure 5.25 shows instantaneous velocity fields for select  $\alpha$  at  $Re = 3 \times 10^4$ . These  $\alpha$  are selected because they are where the force curves change their qualitative behavior, as illustrated in figure 5.17(b).

In figure 5.25, the column of images on the left demonstrate the velocity field with vectors and the vorticity field with the color contour map. The column on the right has the freestream horizontal velocity removed from the flow so that the disturbance velocity field is plotted with vectors. The velocity vectors are plotted in such a way that every other vector is not plotted. Thus, the vector density is about a fourth of the raw data. As  $\alpha$  increases from  $0^\circ$  to  $8^\circ$ , the separation point moves forward as indicated by both the vorticity map and the vector field. The separation point is defined as the point on the surface at which the flow reverses direction. It is also the point at which vorticity is released from the boundary layer into the freestream.

When  $\alpha$  increases from  $8^\circ$  to  $10^\circ$ , the flow is no longer separated over the majority of the airfoil. The separation point has moved further back on the airfoil, and there is not as much vorticity released from the boundary layer. As shown in figure 5.17(b), this relates to the sudden decrease in drag and increase in lift experienced by the wing between these two values of  $\alpha$ . As  $\alpha$  increases further to  $12^\circ$ , the reattached turbulent boundary layer remains attached along most of the chord, while at  $\alpha = 14^\circ$ , there is separation from the leading edge, and no sign of attached flow on the upper surface of the wing.

The reason for the attached flow at  $\alpha = 10^\circ$  is that a laminar separation bubble forms near the leading edge. The separation point at  $\alpha = 8^\circ$  is near the mid-chord, and the flow is separated until the trailing edge. At  $\alpha = 10^\circ$ , the separation point has moved

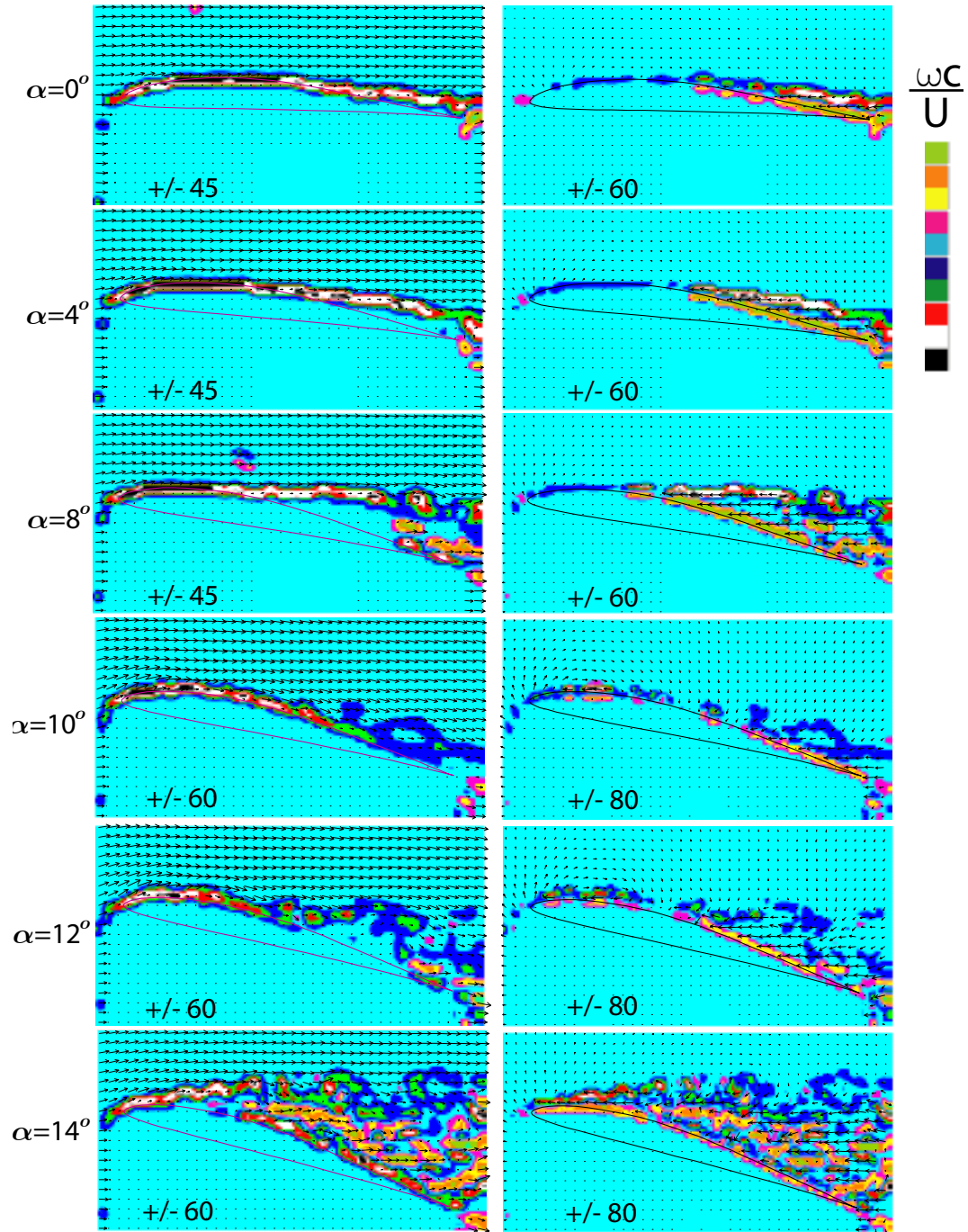


Figure 5.25: E387 Flow Fields at  $Re=30k$

The flow fields were measured using the PIV technique described in section 4.3.2. The left column shows the original flow field to demonstrate the separation, which is defined as the point at which the flow near the boundary reduces to zero. On the right, the free-stream velocity has been removed from each vector to show the disturbance velocity field. The colors represent levels of vorticity, and the color map for each image is shown. The maps are symmetric about zero, and the limits are shown on each image.

to the leading edge, and the separated shear layer becomes unstable and transitions to turbulence. This transition occurs before the trailing edge, and the shear layer is close enough to the wing surface that the flow reattaches to the wing surface.

Using the 200 mm lens, higher spatial resolution velocity fields were obtained to verify the above interpretation. A composite of the 5 images taken along the chord is shown in figure 5.26, and the flow field and vorticity map of the composite looks similar to the low resolution image in figure 5.25. In this composite image, the CCD image is displayed with bright red shaded over the reflection and shadow region, velocity vectors drawn in black (although they are mostly too small to see), and a vorticity color map shaded over top of the image. The colors used in the color map are different from those in figure 5.25 and are described in the caption. The velocity and vorticity fields are averages of 50 realizations.

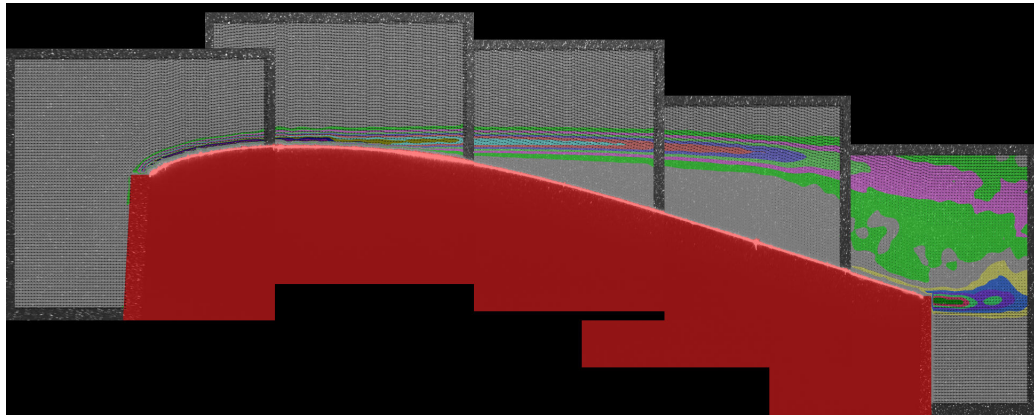


Figure 5.26: High Resolution DPIV at  $Re=30k$ ,  $\alpha = 8^\circ$

The 200mm focal length lens was used to obtain higher spatial resolution, and the images obtained are combined here to visualize the entire wing. The CCD camera image is in the background, with the glare and shadow identified with the red shade. The velocity vectors are drawn in black, but are not fully visible. The vorticity map is shaded with a 20 step color map spread between  $-130 \frac{c}{U}$  and  $90 \frac{c}{U}$ . The grey tone spans the zero value.

Similar images were taken at other even angles of attack, and the results at  $12^\circ$  are shown in figure 5.27. Here the vorticity is again seen to break away near the leading edge, but then reattaches and stays close to the upper surface. The vorticity is spread out over the wing, but is closer than at  $\alpha = 8^\circ$ . A plot of the boundary layer profiles perpendicular to the surface demonstrates that in the average velocity field there is a stagnant region near the leading edge with reattachment downstream. This is seen in figure 5.28.

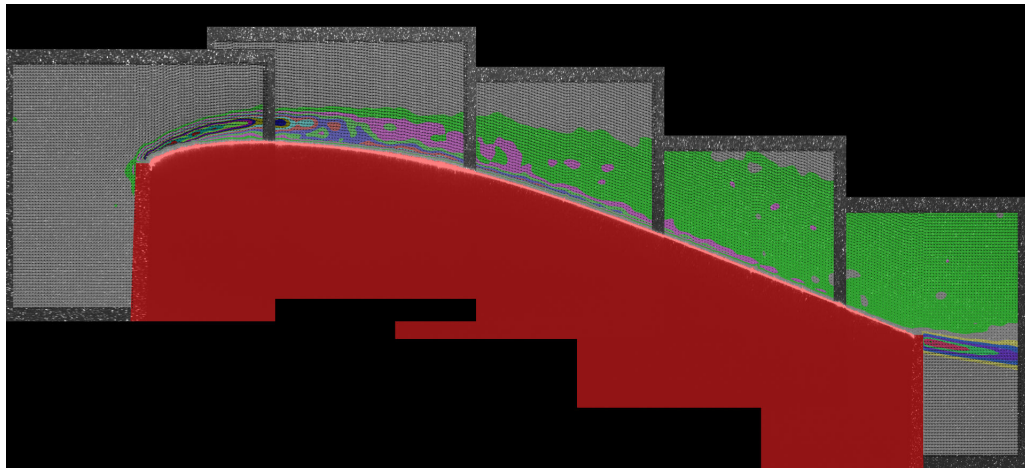


Figure 5.27: High Resolution DPIV at  $Re=30k$ ,  $\alpha = 12^\circ$

At  $12^\circ$ , the vorticity separates from the surface of the wing near the leading edge, and then reattaches for the remainder of the wing. There is some spreading of the vorticity, but the flow is attached unlike at  $\alpha = 8^\circ$ . The color system in this figure is identical to that of figure 5.26.

The average velocity field has very little or no reversed flow. However, viewing a representative instantaneous flow field demonstrates that there is significant reversed flow near the leading edge. Figure 5.29 has a large patch of vorticity, with reversed flow near the surface. This reversed flow is more apparent in the boundary layer profiles of the instantaneous flow, shown in figure 5.30.

These velocity fields demonstrate that the drag increase at moderate  $C_L$  is not caused by the laminar separation bubble, but by simple laminar separation with no reattachment.

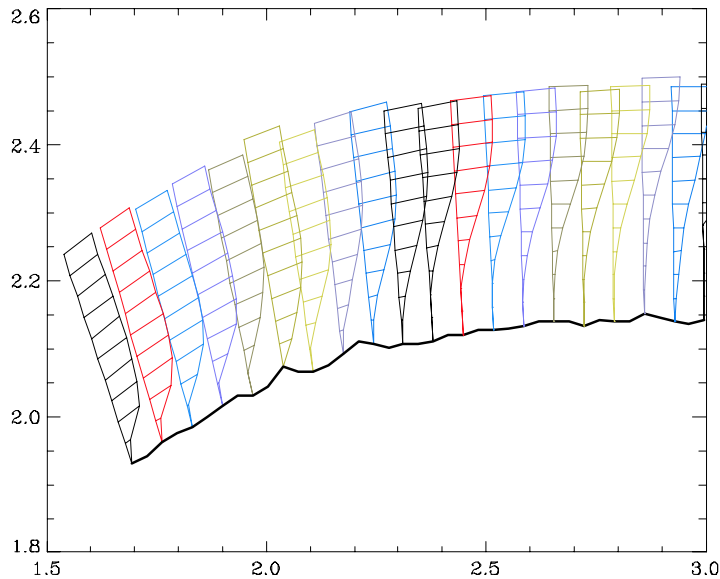


Figure 5.28: Boundary layer profile at  $Re=30k$ ,  $\alpha = 12^\circ$

In the average flow field, the boundary layer near the wing shows a region of stagnated flow near the leading edge. The average flow then reattaches and progresses down the wing. These profiles are taken perpendicular to the wing surface, the profiles are spaced at twice the mean spacing of the vectors in figure 5.27, while the vectors in each profile are spaced at the mean spacing.

The drag decrease at higher  $C_L$  is caused by the laminar separation bubble forming, and the turbulent shear layer reattaching to the wing's upper surface.

## 5.2.4 Separation Point

Similar to what was done in section 5.1.3, the separation point on the wing can be measured using the raw images. Using the raw images rather than the velocity vector fields allows for more precise measurement of the separation point because the PIV process is a spatial average. In acquiring the raw images at the higher  $Re$ , a new technique of

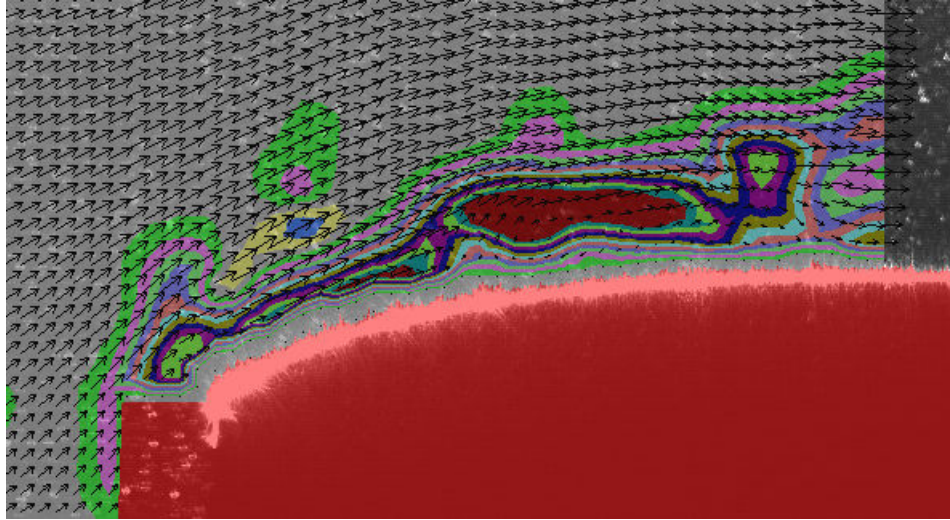


Figure 5.29: Instantaneous high resolution flow field

The instantaneous flow field at the same conditions as in figure 5.27 shows a patch of concentrated vorticity near the leading edge. This patch breaks up quickly and travels downstream. This patch of vorticity identifies a vortex with reverse flow near the wing.

identifying the separation streamline was found. In section 5.1.3, the dark line emitted from the wing's upper surface was interpreted as being the boundary layer which has few particles, and is therefore dark. At the higher  $Re$ , this was also identified, but a new technique which made the separation point white was found.

This technique involved running the laser at maximum power, focusing the light sheet on the wing so that the thinnest part of the sheet hits the wing, making the sheet more narrow in the streamwise direction, and moving the laser in the some way while capturing images. The requirement here is that the laser apply enough intensity (power per unit area) to cause some burning of the surface covering, or ablation of the surface material itself, or revaporization of oil and other droplets on the surface. The movement of the laser is required to set up a time varying intensity field. It was found that moving the laser in the stream wise direction works, as does moving it in the spanwise direction. This technique even works with changing the focus point of the sheet, effectively

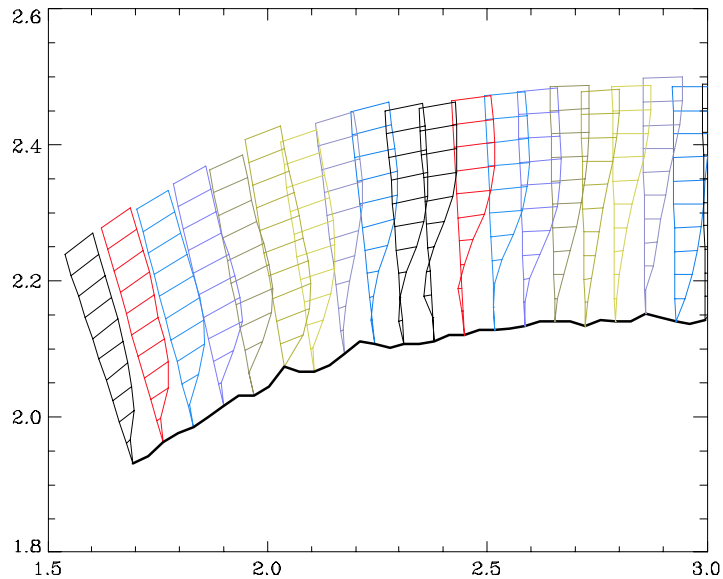


Figure 5.30: Instantaneous boundary layer profile

The boundary layer profiles for the data in figure 5.29 makes the reverse flow near surface more apparent. In the average boundary layer, this reverse flow is not present.

changing the thickness of the sheet at the wing surface. An example of the results of this technique is shown in figure 5.31.

Measuring the separation point at different  $\alpha$ , the results at  $Re = 3 \times 10^4$  are compared with the lower  $Re$  cases in figure 5.32. The separation location moves forward, toward the leading edge, as  $Re$  and  $\alpha$  increase. At  $Re = 30k$ , the separation point moves forward gradually for  $\alpha < 9^\circ$ , but then jumps to the leading edge at  $\alpha = 10^\circ$ . This is consistent with the pervious findings about the laminar separation bubble. Between  $8^\circ$  and  $10^\circ$ , the separated shear layer transitioned quickly, allowing turbulent reattachment. This is interpreted as a laminar separation bubble, as shown in figure 1.9. This bubble forms at the same  $\alpha$  as the discontinuity in the separation point plot.

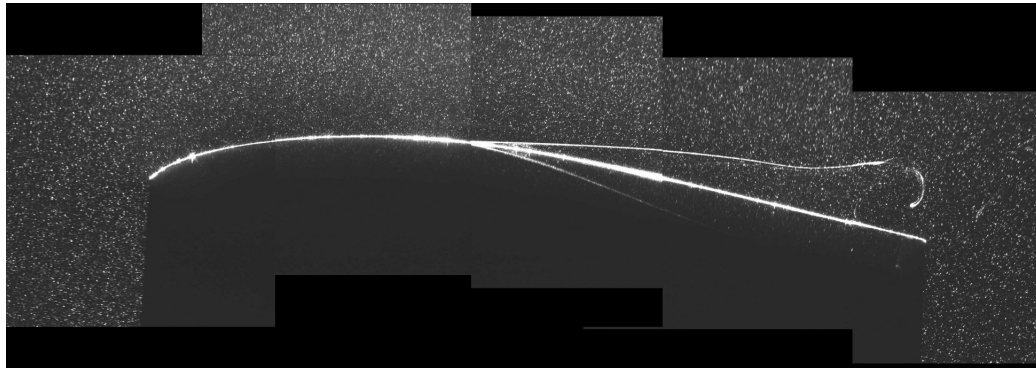


Figure 5.31: Separation streakline for E387

The separation streakline was visualized by using high laser power, and moving the laser within the sheet plane as images were acquired. Moving the high intensity laser caused particles to be released (ie. burned, ablated, or vaporized) into the boundary layer, and as the boundary layer separates, the particles follow the separation streakline and are illuminated by the laser. This image is of the E387 at  $\alpha = 4^\circ$  and  $Re = 3 \times 10^4$ .

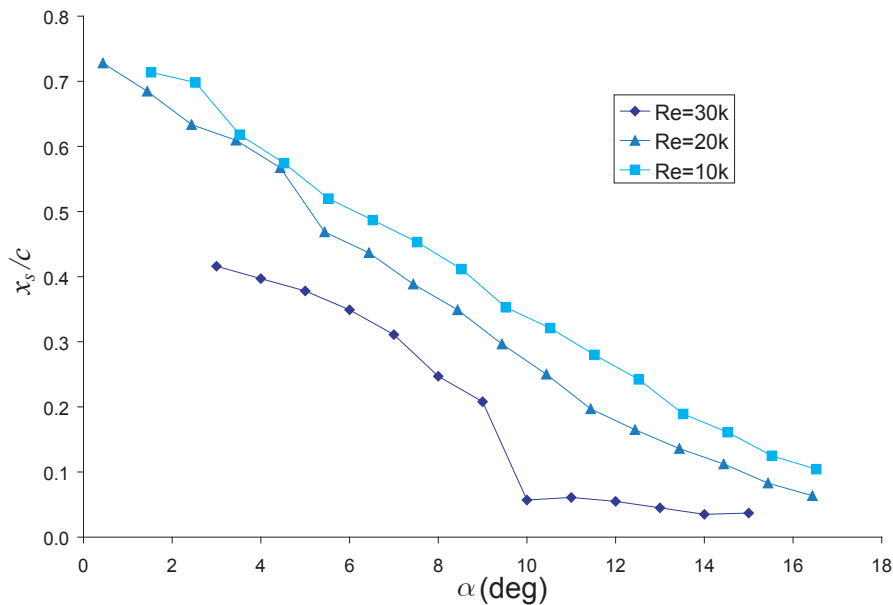


Figure 5.32: Separation point vs angle of attack for E387

The separation point location was measured using images similar to 5.31 at various  $\alpha$ . At high  $\alpha$ , the separation streakline was not illuminated, but was dark similar to  $Re = 10k$  and  $20k$ . The discontinuity for the  $Re=30k$  case occurs where the laminar separation bubble forms.

### 5.2.5 Roughness

The above results were obtained using two different wings. For the lower Re (10k and 20k), a wing with 3.5 cm chord was milled out of aluminum, sanded, and painted with black primer. For the higher Re (30k and 60k), a wing with 9 cm chord was milled out of aluminum, but it was not sanded or painted. The aluminum was not rough to the touch, but roughness and streaks from the mill could be seen on the wing surface.

Since there were two wings being used in the study, an attempt was made to compare them directly by measuring the forces at the same Re. By increasing the wind tunnel to 20 m/s, the smaller wing could be tested at Re = 40k, and by setting the wind tunnel to 6.6 m/s, the larger wing could also be tested at this Re. The results are shown in figure 5.33, and the large rough wing has the sudden increase in lift characteristic of a laminar separation bubble, while the small smooth wing does not.

This difference is caused by a difference in surface roughness. The large rough wing was subsequently sanded to a near-mirror finish, and retested at Re=40k. The results of this test are shown in figure 5.34 and are compared with the previous results at Re=30k and Re=60k.

The rough wing has the abrupt change in force coefficients at both Re. However, after sanding the wing, the abrupt change no longer occurs at Re=30k, and at Re=60k the range of  $\alpha$  where the laminar separation bubble is present has become smaller. At both Re, the  $C_D$  has increased for the smooth wing. These facts indicate that decreasing the roughness of a wing has a similar effect to decreasing the Re.

The small increase in  $C_L$  experienced by the smooth wing at Re=30k can be explained as a transient response to the change in  $\alpha$ . At  $\alpha = 11^\circ$ , the  $C_L$  increases suddenly, but quickly decreases. The data acquisition system should be timed to either avoid this transient response, or capture it fully. Alternatively, post-processing of the data could ignore the transient response.

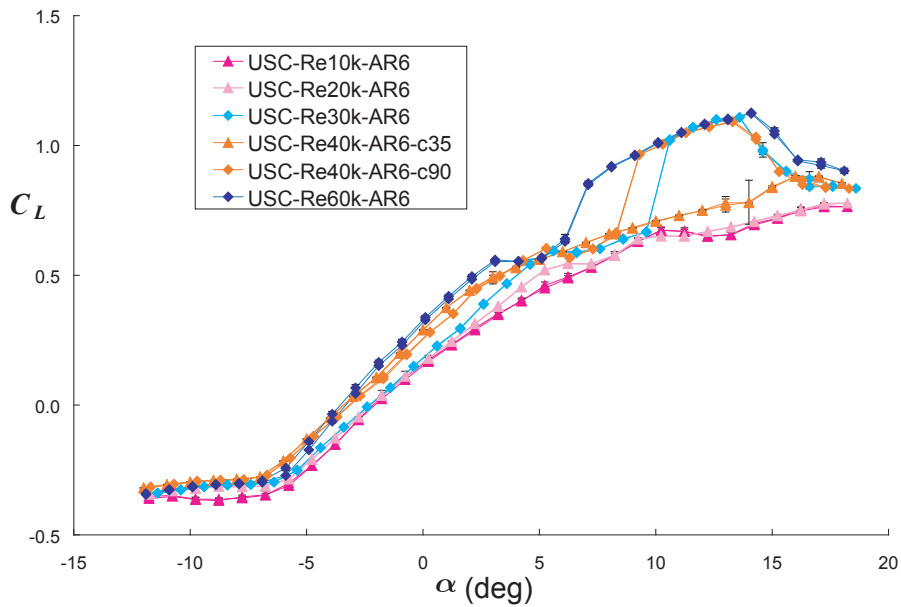


Figure 5.33: Comparison at  $Re=40k$

To ensure the large and small versions of the E387 wing were similar, each wing was tested at  $Re=40k$ . Similar force measurements would indicate similar geometry. Since they are not similar, the geometries must be different.

## 5.3 Leading Edge Vortex

### 5.3.1 Dye Visualization

Flow visualization experiments using dye injection were performed for a swept wings. Experiments were conducted in a water channel, and pictures and videos were taken to document the flow around the swept wings. The goal was to identify sweep angles and  $\alpha$  where a leading edge vortex (LEV) forms.

Four wings were made of 0.08 cm thick brass shim stock, each with a 4.45 cm chord, 5% circular-arc cambered airfoil and sweep angles:  $\Lambda = 0, 20, 40, 60^\circ$ . Each wing has an aspect ratio of 6, an area of  $119 \text{ cm}^2$ , a thickness ratio of 1.8% (0.08/4.45), and no taper. The wings were made by rolling the shim stock to the specified camber,

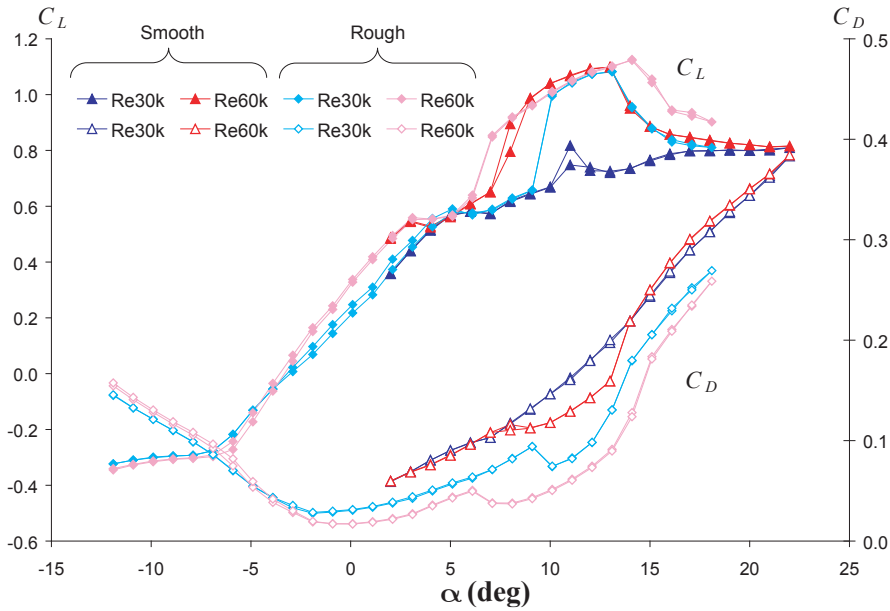


Figure 5.34: Comparison at  $Re=40k$

After sanding and polishing the large E387 wing, it was retested at  $Re=30k$  and  $60k$ . Smoothing the wing down decreased the effect of the laminar separation bubble. This shows that increased roughness is similar to increased  $Re$ , and that the primary difference between the small and large wings was that the large wing was more rough. This means that the large (rough) wing was tested at a higher “effective”  $Re$ , or conversely, that the small (smooth) wing was tested as a lower “effective”  $Re$ .

then soldering each half of the wing together. The sting (support mount) was made by stacking 3 pieces of the same brass shim stock together. It was soldered to the wings in the center of the wing (at the apex). The chord-wise dimension of the sting was 3.4 cm.

These experiments revealed a number of unique flow features for low  $Re$  swept wings, and a full report is given in appendix A. The most relevant result for the current study is that an LEV was formed with the  $60^\circ$  swept wing at  $\alpha = 15, 18,$  and  $20^\circ$ , shown as a sketch in figure 5.35. There are two types of LEV, and the first type is shown in figure 5.35(a). This LEV travels parallel to the leading edge, and the vortex helix angle is less than  $45^\circ$ . The second case begins to develop in figure 5.35(b), and is apparent in

figure 5.35(c). This LEV travels at an angle somewhere between the leading edge and the free-stream velocity. The vortex helix angle is greater than  $45^\circ$ .

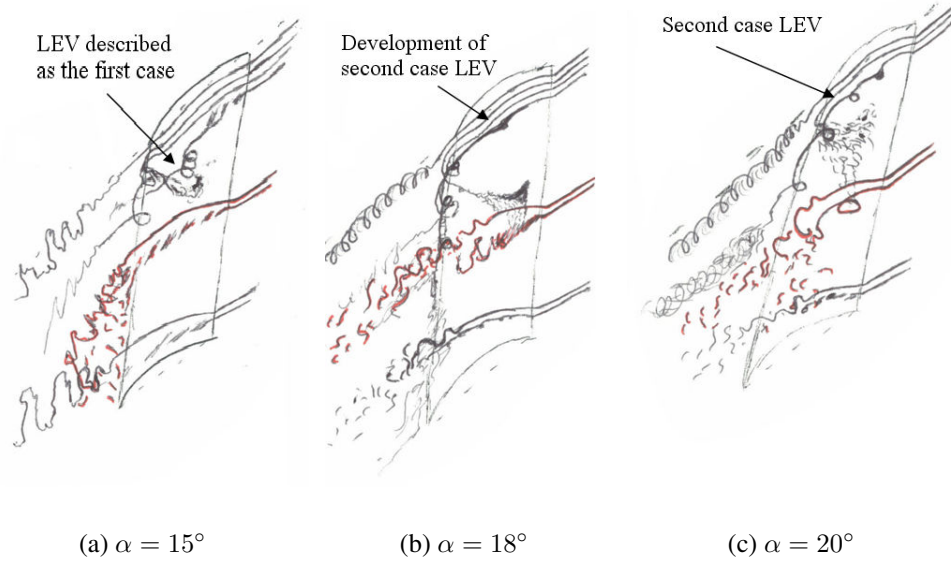


Figure 5.35: Sketches of Dye Visualization Experiments

These sketches show the qualitative flow patterns around the  $60^\circ$  swept wing at  $Re = 5k$ . The upper part of the sketch is the wing center-line (ie. the plane of symmetry of the wing). Dye streaks are drawn at three span-wise locations, and each span-wise location has several different heights above the wing drawn. At any given span-wise location, different stream tubes will illustrate different parts of the flow field depending on how far it is from the surface (ie. how much it is effected by the boundary layer and separation).

As an example of the images and video captured to create the sketches above, figure 5.36 is one image captured of the vortex in figure 5.35(a). The center of the wing (apex) is on the right of the image, and the flow is moving right to left. The red dye streak is impinging on the leading edge of the wing, and is spread down the span. At about the mid-chord, the dye filament is wrapped into a vortex and reverses direction, traveling back upstream. Here, the filament is split, and some travels downstream and into the wake, while another portion travels further upstream, being wrapped into another vortex,

closer to the leading edge than the previous vortex. The filament travels around this vortex 2 times before traveling into the wake. One can estimate the helix angle by comparing the diameter of the vortex to the axial distance traveled by the vortex filament over one rotation. Since the distance traveled is less than the diameter, the helix angle must be less than  $45^\circ$ .

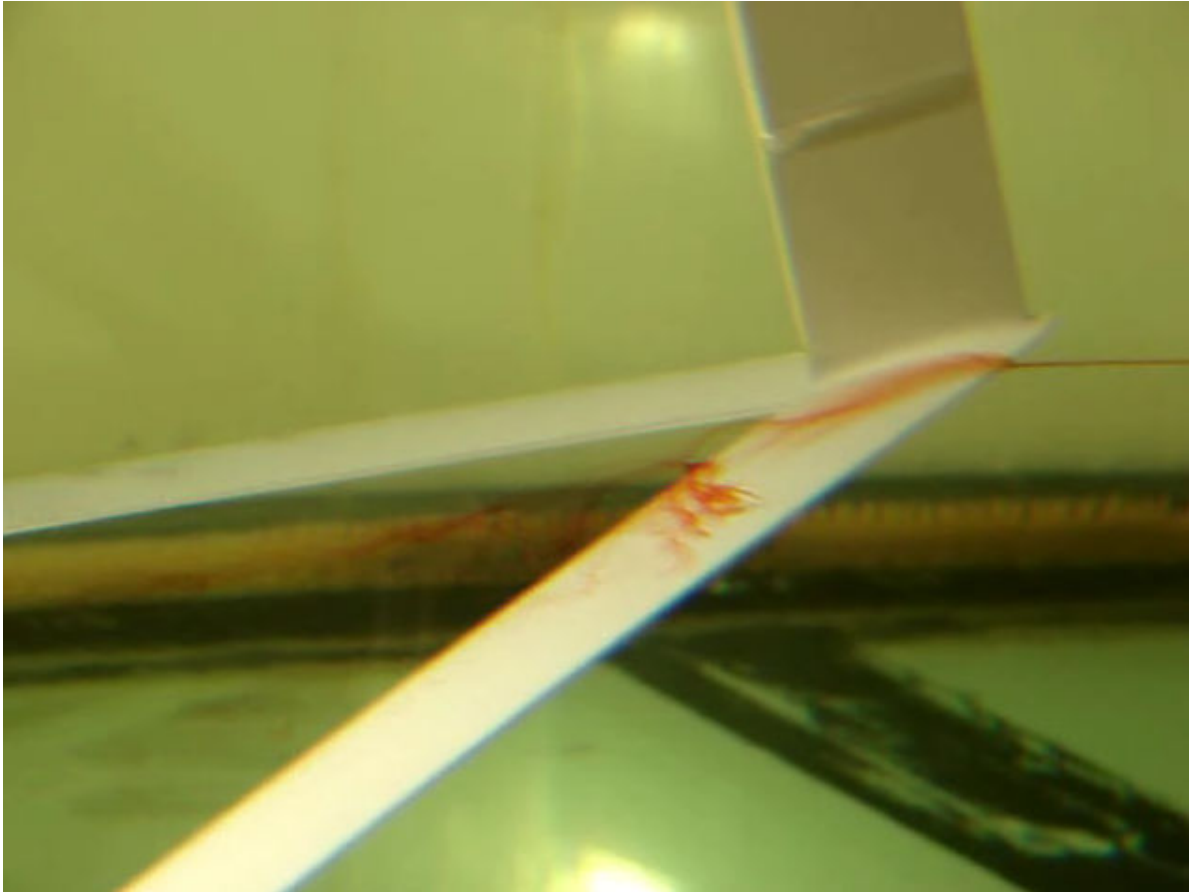


Figure 5.36: Dye visualization of LEV

Video footage of the dye visualization was taken, and this image demonstrates the existence of a vortex over the  $60^\circ$  swept wing at  $\alpha = 15^\circ$ . The dye filament impinges on the leading edge, spreads as it travels downstream and slightly along the span. It is then splits and a portion is carried into the wake, while the other portion is wrapped into a vortex at about mid-chord. The filament is wrapped around the vortex 2 or 3 times, and is then carried into the wake.

### 5.3.2 Smoke Visualization

The LEV identified in the water channel was also present when the wing was placed in the wind tunnel. To maintain the same  $Re$  as in the water channel, the wind tunnel speed was set to 1.6 m/s. This is the slowest speed that the wind tunnel can operate, and the turbulence was not measured at this wind tunnel speed. It is expected that the relative turbulence would be much larger than at 5 or 10 m/s. The turbulence level was not measured in the water channel either.

The PIV system was used to visualize the LEV in the wind tunnel. The flow field around the LEV was not measured, because the core of the vortex was dark, with no particles to track. This is because the vortex is formed by fluid in the boundary layer, and as demonstrated earlier, there are very few particles in the boundary layer. A demonstration of the dark region of the vortex is shown in figure 5.37.

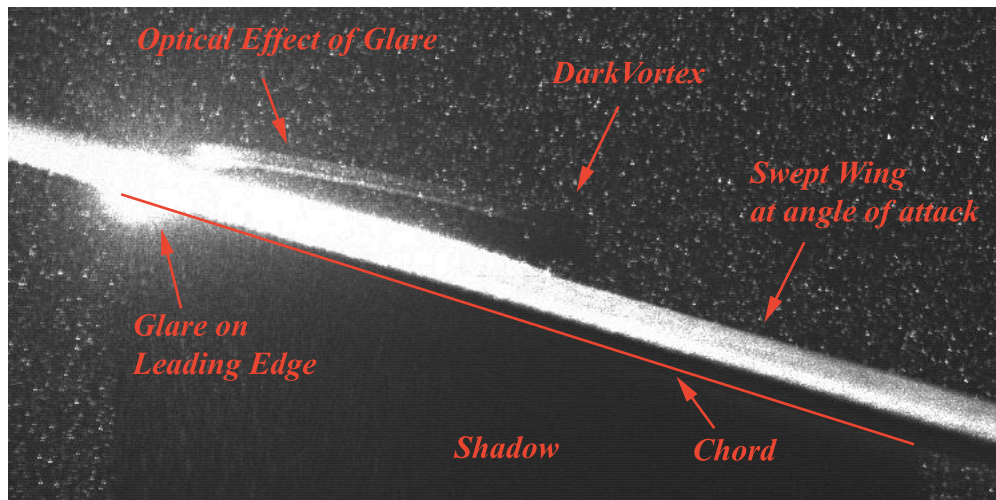


Figure 5.37: Dark region indicating vortex on wing

As in the case of the separation streakline, the boundary layer has few particles in it and thus dark regions in the flow often identify regions that come from the boundary layer. The vortex is formed by boundary layer flow, and is hence dark in PIV images. Here, the laser sheet is 3.1 cm outboard from the wing apex and aligned with the freestream velocity. The local wing chord is identified by the shadow projected below the wing.

Here, the flow is moving left to right, and the laser light sheet is intersecting the wing at 3.1 cm outboard of the wing center (apex). The  $60^\circ$  swept wing is at  $\alpha = 15^\circ$ . When looking upstream, the light sheet is on the left of the apex, and the shadow region indicates the chord length. The laser illuminates the wing, not only in the image plane, but also the inboard and outboard sections. Near the leading edge, there is significant glare that was minimized in the experiments, but could not be eliminated. The glare is causing the streak in the flow emanating from near the leading edge. This is not part of the flow, but is merely an optical effect that could not be removed. The dark region near the mid-chord is the LEV, and is dark because it is composed of boundary layer flow, and there are few particles in the boundary layer.

Similar to the illumination of the separation streakline described in section 5.2, the dark vortex can also be illuminated by turning the laser power up, and moving the laser sheet while obtaining data. In this case, the particles that are emitted from the surface enter the boundary layer, and are later entrained into the vortex. The particles in the vortex are then illuminated by the laser. Figure 5.38 shows the results of this technique where the laser sheet is again 3.1 cm outboard from the wing center (apex). This figure can be compared with figure 5.37 and the location of the dark region coincides with the illuminated vortex.

This light line technique can be applied to various spanwise locations to track the shape of the vortex along the span. In applying this technique, the laser sheet was moved outboard from 2.1 cm to 4.1 cm from the wing center (apex) as images were acquired. In figure 5.39, a series of images illustrates the development of the LEV in the spanwise direction. The images read from left to right, and from top to bottom, and progress from the inboard most station to the outboard most station. This is also the order in which the images were acquired.



Figure 5.38: Vortex illuminated by particles

Similar to the illumination of the separation streakline, the vortex is illuminated by moving a high power laser sheet while acquiring images. The laser is causing particles to be released into the boundary layer, which are subsequently entrained into the vortex. In this case, the laser is moved perpendicular to the laser sheet because the vortex forms inboard and travels out.

Figure 5.39(a) is the beginning of image acquisition, and there is no LEV apparent at this spanwise location. This was also verified by doing this visualization at single spanwise stations. Moving outboard to figure 5.39(b), a small elliptically shaped structure appears at about the mid-chord, and this most likely indicates the early formation of the LEV. A larger structure seems to have formed above and downstream of the LEV, and is present at all outboard stations. At the next station, the vortex is visible still at about the mid-chord, and now the rolled up layers in the vortex are visible. The next image is taken at the same station as figure 5.38, but here the glare from the leading edge is much brighter. The vortex and the structure above it are still identifiable.

The next station is the first sign of vortex stretching. Before this station, the vortex was a triangular shaped structure, whereas in this image, the vortex is stretching up and to the left, distorting this shape. The next station exhibits the end of the LEV, and the vorticity is being shed into the wake. The final two images are at the last spanwise

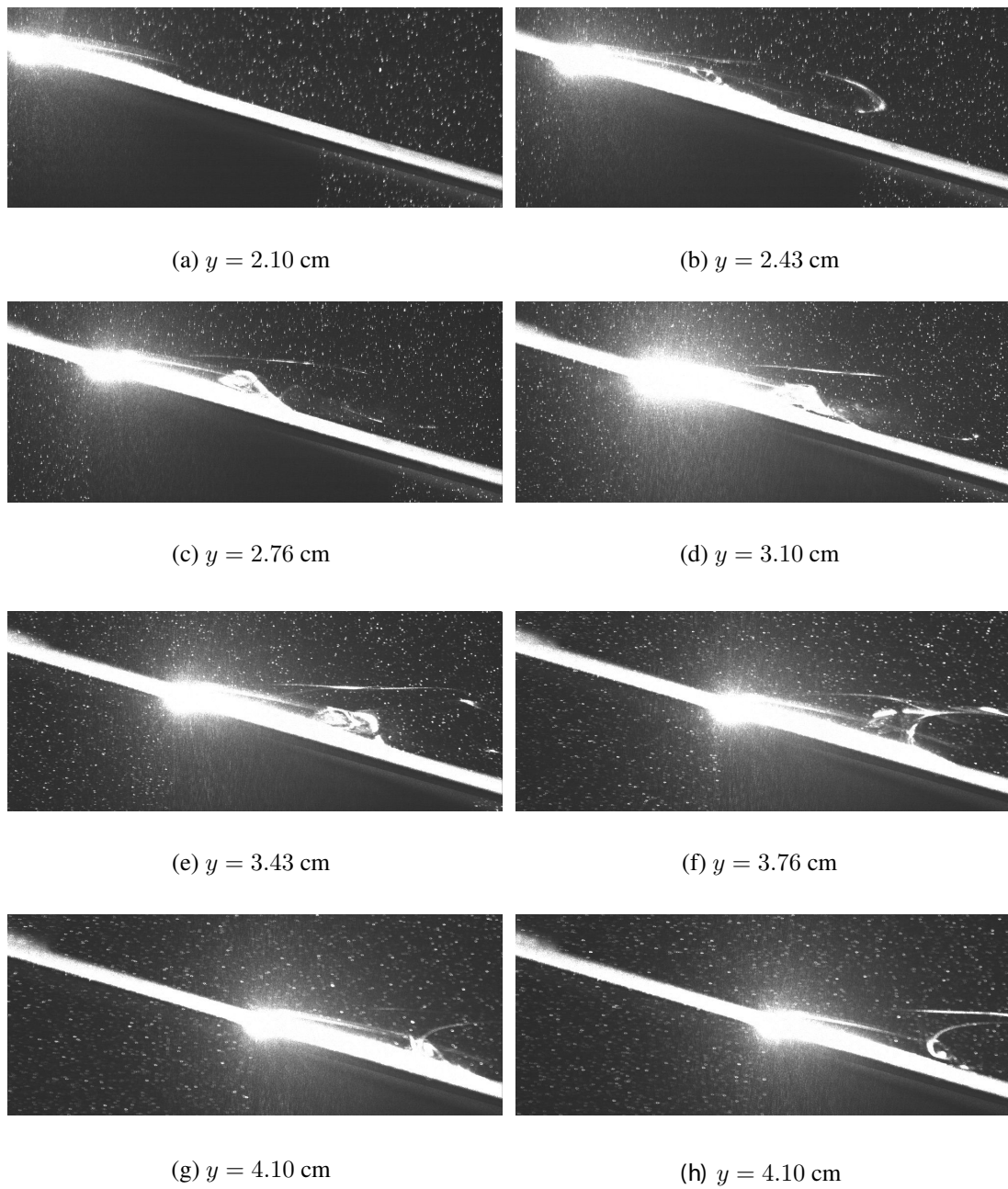


Figure 5.39: Vortex spanwise development

As in figure 5.38, the vortex is illuminated by moving the laser perpendicular to the sheet plane, and images are acquired throughout. The spanwise development of the vortex can be seen. The vortex is clearly present while in the windtunnel.

station, and the first indicates that all vorticity from the LEV has been shed, while the second reveals that there is a secondary vortex with opposite sign, just downstream from where the LEV was located.

### 5.3.3 Force Measurements

The dynamical significance of this vortex was tested by measuring the lift and drag of the  $60^\circ$  swept wing at  $0^\circ < \alpha < 20^\circ$ . If the vortex effects the forces generated by the wing, then there should be some discontinuities in the force curves near  $\alpha = 15^\circ$ . Figure 5.40 is a plot of the  $C_L$  and  $C_D$  for various  $\Lambda$  and Re. Focusing on the  $\Lambda = 60^\circ$  and  $\text{Re} = 5 \times 10^3$  case, there is no discontinuity in the slope of either the  $C_L$  or  $C_D$  curves near  $\alpha = 15^\circ$ . Thus, the vortex identified in the previous section has no significant impact on the forces generated by this wing.

The forces at  $\text{Re} = 1.5 \times 10^4$  are plotted to give some comparisons of performance for different sweep angles. Only the uncertainty for  $\Lambda = 60^\circ$  is plotted here, and is representative of all the other curves. For this higher Re, the uncertainty is often similar to the symbol size. The  $\Lambda = 10^\circ$  swept wing has the highest maximum  $C_L$ , but also the largest minimum  $C_D$ . The 40 and 60 degree swept wings have much lower  $C_L$  than either the 0 or 20 degree swept wings, but also lower  $C_D$ .

Figure 5.41 is a plot of the lift-to-drag ratio for these 4 sweep angles, all at  $\text{Re} = 1.5 \times 10^4$ . The non-swept wing has higher lift-to-drag ratio than any of the swept wings, at nearly all  $\alpha$ . In this plot, the 60 degree swept wing again has no discontinuities in performance near  $\alpha = 15^\circ$ .

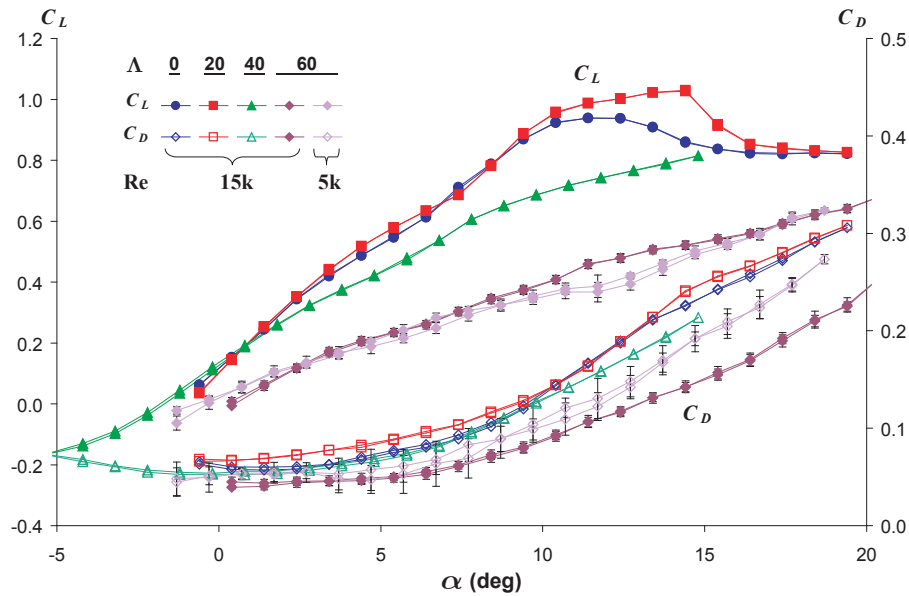


Figure 5.40: Swept wing force coefficients

Force measurements were made to determine the effect of the vortex on the performance of the wing. Most measurements were at  $Re=15k$  as this gave better resolution of the measurements. However, at  $\Lambda = 60^\circ$ , measurements were also made at  $Re=5k$  to test the effect of the vortex identified above. Since the vortex exists for  $\Lambda = 60^\circ$  and  $\alpha = 15^\circ$ , and since there are no discontinuities in the force curves near this condition, the vortex is shown to have no significant effect on the forces.

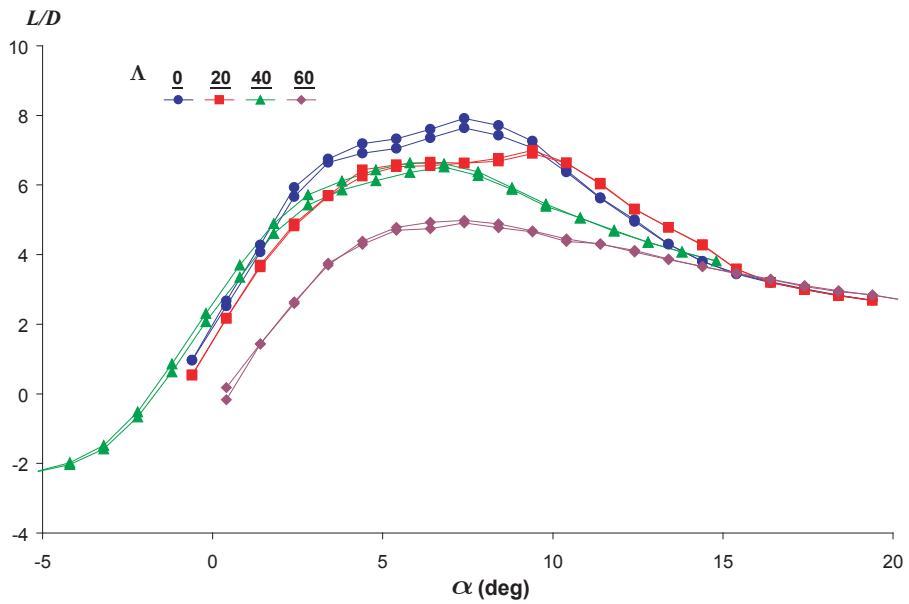


Figure 5.41: Swept wing lift-to-drag ratio

The ratio of lift-to-drag is a common measure of wing performance and efficiency. Again, the vortex is seen to have no significant effect for the  $\Lambda = 60^\circ$ ,  $\alpha = 15^\circ$  case, as the curve is smooth here.

# Chapter 6

## Conclusions

This study is composed of three primary investigations: the forces generated by wings and airfoils at  $10^4 < \text{Re} < 10^5$ , the laminar separation bubble (LSB) on the Eppler 387 (E387) airfoil at  $\text{Re} = 6 \times 10^4$ , and the leading edge vortex (LEV) formed by a swept wing at  $\text{Re} = 5 \times 10^3$ . For each investigation, a combination of quantitative force measurements, qualitative flow visualization, and quantitative flow field measurements were used, and relating them yields increased understanding of how the flow field generates the forces measured. In addition, comparisons with previous measurements, numerical computations, and theoretical predictions were emphasized to illustrate the accuracy of the current measurements.

The investigation of the forces generated by wings and airfoils supported the findings of Laitone [16] in that the thick airfoil did not perform as well as the thin airfoils (see figures 1.7 and 5.6). In Laitone's study the thick airfoil had zero camber, whereas in the present study, the thick airfoil had approximately the same maximum camber as the thin, cambered airfoil. Also, Laitone's study only looked at 3D wings, whereas this study showed that the thin airfoil performs better than the thick airfoil in both 2D and 3D conditions.

The force measurements also allowed the testing of lifting line theory at these Re. Lifting line theory was originally developed for application to high Re cases, where viscous effects were negligible. It can be applied at  $\text{Re} > 10^6$  to accurately determine the drag difference between a 2D airfoil, and a 3D wing with some aspect ratio, but it is undetermined whether this theory can be applied at lower Re with accurate results.

Pelletier & Mueller [28] and Laitone [16] both used their measurements to determine if lifting line theory can be used accurately at  $Re < 10^5$ , but they arrive at opposite conclusions. Pelletier & Mueller find that lifting line theory is an accurate model for their flat and cambered plate wings at aspect ratios of 2, 3, 6 and with  $6 \times 10^4 < Re < 2 \times 10^5$ . However, Laitone's lift measurements on a thin cambered plate at  $Re = 4 \times 10^4$  and aspect ratio 6 showed more than 20% higher lift-curve-slope than predicted by thin airfoil theory. He also concluded that the induced drag of the wing is not predicted accurately by lifting line theory, and that it varies with  $Re$  and airfoil geometry.

The present measurements find no significant disagreements with the initial lift-slope-curves measured, and those predicted by lifting line theory. However, the induced drag predicted by lifting line theory was often significantly different from the measured values (see figure 5.12). For the flat plate, lifting line theory applied rather well for both  $Re$ , and for most  $\alpha$ . There was slightly more disagreement at  $Re = 20k$ , but still not significant. Lifting line theory applied well for the cambered plate at low  $\alpha$  at both  $Re$ , but was significantly different at  $\alpha > 7^\circ$ . The E387 case was the most interesting, because it showed excellent agreement at all  $\alpha$  for  $Re=10k$ , but then increasing disagreement for increasing  $Re$  (see figure 5.21). At the highest  $Re$ , the 2D drag was larger than the 3D drag, which shows not only quantitative disagreement with lifting line theory, but qualitative disagreement as well. The basic assumptions of lifting line theory do not apply to this case, and new models must be developed.

This agreement at low  $Re$ , and more disagreement at high  $Re$  is puzzling because lifting line theory was developed as a high  $Re$  theory. The present results support the notion that there is a middle range of  $Re$ , lower than the high  $Re$  but higher than low  $Re$ , where lifting line theory does not apply. This middle range can be related to Schmitz's results that there is a critical  $Re$  where performance drops. However, now it is seen that it is not a single  $Re$ , but a range of  $Re$  where performance is changing significantly,

and in this range, lifting line theory does not apply. This range can be referred to as the critical Re range, and for each airfoil, there is a different range, but thus far, most airfoils have been shown to have a critical Re range somewhere between  $10^4$  and  $10^5$ .

The best explanation for the breakdown of lifting line theory in this range of Re is the presence and importance of 3-dimensional and spanwise varying flow around the wing. Lifting line theory would suppose that for a 2D airfoil, there is drag due to friction and pressure. In the 3D case, the only difference is the addition of wing-tip vortex drag (ie. induced drag). This additional component of drag should be proportional to  $C_L^2$ . The fact that the E387 airfoil has lower drag in the 3D case than in the 2D case directly contradicts lifting line theories basic assumption that the only difference between the 2D and 3D case is the addition of wing-tip vortex drag. The 3D case must have less friction and/or pressure drag. This decrease in friction and/or pressure drag must be greater than the increase due to wing-tip vortex drag, and it is likely caused by the 3-dimensional and spanwise varying flow introduced with the presence of wing-tips. This 3-dimensional and spanwise varying flow could move the separation location closer to the trailing edge, either by changing the pressure field over the wing, or by inserting momentum into the boundary layer to resist the adverse pressure gradient for longer.

Using the PIV data acquisition technique of seeding the flow with particles, the separation point could be identified and measured. These measurements showed that at Re = 10k and 20k, the separation point for the E387 moved gradually to the leading edge, while for the cambered plate, it jumped suddenly to the leading edge across a one degree increase in  $\alpha$  (see figure 5.14). This sudden jump was related to the forces measured, and occurs near the sudden increase in the lift-curve-slope and the drag-curve-slope (see figure 5.16). This same type of behavior was observed for the E387 at Re = 30k and 60k (see figure 5.32), and the sudden jump of the separation point to the leading edge is related to the formation of the LSB. When the separation point moves to the leading

edge, the LSB forms. It may be possible that a LSB is forming on the cambered plate at  $Re = 20k$  when the separation point jumps to the leading edge. Further investigation would be required to verify this.

Many previous studies of wings and airfoils at  $Re < 10^5$  have included a study of the E387 at  $Re = 6 \times 10^4$ . While the quantitative results of each study have varied by as much as 50% in drag measurements, the qualitative results have been consistent: there is a drag increase at moderate lift coefficients, and as  $\alpha$  increases, the drag decreases and the lift increases (see figure 1.4). This behavior is often related to the LSB, and using surface oil flow visualization, Selig et al concluded that the drag increase was caused by the formation of an LSB. However, these studies were not performed at  $Re = 6 \times 10^4$  where the drag increase is most prominent, and the measurements made previously on the E387 at  $Re = 10k$  and  $20k$  suggested that the LSB may actually be causing the drag decrease at higher  $C_L$ .

Hence, force measurements and particle image velocimetry (PIV) were used to investigate this airfoil at this range of  $Re$  and  $\alpha$  to determine how the LSB effects the forces on the wing. From these results, it is clearly concluded that the LSB is actually responsible for the drag decrease at higher lift, and that the drag increase at moderate  $C_L$  is caused by pure laminar separation with no reattachment. Hence, at  $Re = 10k$  and  $20k$ , there is no laminar separation bubble, just laminar separation with no reattachment. This also occurs at  $Re = 30k$  and  $60k$  for  $\alpha < 10^\circ$  and  $6^\circ$ , respectively. Above these angles of attack, the qualitative nature of the flow changes, and the laminar separated shear layer transitions to turbulence before reaching the trailing edge (see figure 5.25). The turbulent separated shear layer transports momentum towards the surface of the wing. The instantaneous flow field may have separation and reattachment along the chord, but the time average flow field will be reattached, increasing the lift and decreasing the drag.

To better compare the results at the two lowest Re (10k and 20k) to the higher Re (30k and 60k), the two models were tested at Re = 40k. This would indicate any differences in the models. The test indicated that the models were significantly different, as the small wing had no discontinuity (which implies no LSB) at Re = 40k, while the large wing did (see figure 5.33). The most apparent difference between the wings was the roughness, and so the large wing was sanded and smoothed to a polish finish, and retested. These results demonstrates that decreasing roughness is similar to decreasing the Re (see figure 5.34. This is not a new result, but the current demonstration is rather dramatic due to the discontinuities in the force curves.

Previous studies have indicated that a swept wing in steady flow at  $10^3 < Re < 10^4$  may generate an LEV. This LEV may improve the performance of some species of birds that have large sweep angles and spend much of their life in flight. The formation of an LEV is a dominant feature of insect flight ( $Re < 10^3$ ) and explains the large  $C_L$  achieved by many insects, but the unsteady effects of wing flapping has always been believed to be necessary for the formation of an LEV. The studies that indicate a swept wing in steady flow can form an LEV were not done rigorously, as the wings were not rigid, and many parameters were not measured and changed throughout the study.

The present study concludes that simple cambered airfoil shapes can form a stable vortex on the upper surface by simply sweeping the wings to a sufficiently large angle ( $\Lambda > 40^\circ$ ). The vortex of the present study is not similar to the LEV formed on insect wings during flapping motion, nor was it similar to the vortex formed by previous studies on swept wings in steady flow at these Re. The vortex identified in this study had a small radius compared with insect LEVs and had a small span-wise length (see figure 5.35 and 5.36). From this, it is concluded that sweep alone is not sufficient to generate an LEV, but that additional features must be considered, such as unsteadiness, taper, or curvature. Also, aspect ratio, airfoil geometry and dihedral angle must be considered.

By measuring the forces on the  $60^\circ$  swept wing at  $Re = 5 \times 10^3$  and at a range of  $\alpha$  will determine whether or not the vortex has any significant impact on the wing's performance. If a sudden increase in lift, or decrease in drag is detected at an angle where the vortex is present, then the vortex is causing this improved performance. Force measurements are more difficult to make in a water channel, so the wind tunnel was used for this. Before making force measurements however, the presence of the vortex had to be determined. This was done using the PIV system described earlier.

The regular PIV data acquisition method was conducted in hopes of attaining data that could yield quantitative information on the velocity field. However, current techniques do not have high enough spatial resolution to give this quantitative information. Improved techniques could be developed, but for now, it is sufficient to say that there is a vortex above the wing at  $Re = 5 \times 10^3$ , at  $\alpha = 15^\circ$ , while in the wind tunnel. This was verified by identifying the dark region above the wing as the vortex, and also using the separation streakline illumination technique (see figures 5.37, 5.38, and 5.39).

With evidence that the vortex exists in the wind tunnel, force measurements were made at a range of  $\alpha$ . Measurements for each sweep angle studied in the water channel were made, but at the higher  $Re$  of 15k. For the  $\Lambda = 60^\circ$  swept wing where the LEV was found, measurements were made at both this higher  $Re$ , and at the same  $Re$  as the water channel experiments. There is no sign of change in force-slopes, or in the shape of the lift-to-drag ratio curve near the  $\alpha$  at which the vortex forms over the wing (see figures 5.40 and 5.41). This indicates that this small vortex has no significant effect on the forces generated by this wing. Perhaps if the vortex were larger (by including flapping, or taper, or spanwise variation of the sweep angle), then the forces might be effected by its presence.

# References

- [1] ABBOTT, I. H., AND VON DOENHOFF, A. E. *Theory of Airfoil sections*. Dover, New York, 1959.
- [2] ABBOTT, I. H., VON DOENHOFF, A. E., AND L. S. STIVERS, J. Summary of airfoil data. *NACA Technical Report 824* (1945).
- [3] ALTHAUS, D. *Profilparen fur den Modellflug. Windkanalmessungen an Profilen im kritischen Reynoldszahlbereich. (Profile Polars for Model Flight. Wind-Tunnel Measurements on Profiles in the Critical Reynolds Number Range.)*. Neckar-Verlag, VS-Villingen, 1980.
- [4] ALTHAUS, D., AND WORTMANN, F. X. *Stuttgarter profilkatalog I - Experimental results for the laminar wind tunnel of the University of Stuttgart*. Friedr. Vieweg and Sohn, Braunschweig, 1972 (English version in 1981).
- [5] ARENA, A. V., AND MUELLER, T. J. Laminar separation, transition, and turbulent reattachment near the leading edge of airfoils. *AIAA Journal* 18, 7 (1980), 747–753.
- [6] BRENDEL, M., AND MUELLER, T. J. Boundary layer measurements on an airfoil at a low Reynolds number in an oscillating freestream. *AIAA Journal* 26, 3 (1988), 257–263.
- [7] BROEREN, A. P., AND BRAGG, M. B. Flowfield measurements over an airfoil during natural low-frequency oscillations near stall. *AIAA Journal* 37, 1 (1998), 130–132.
- [8] BROEREN, A. P., AND BRAGG, M. B. Unsteady stalling characteristics of thin airfoils at low Reynolds number. In *Proc. Conf. on Fixed, Flapping and Rotary Wing Vehicles at Very Low Reynolds Numbers* ((Notre Dame, Ind., June, 2000 2000), pp. 396–420.
- [9] FINCHAM, A. M., AND SPEDDING, G. R. Low cost, high resolution DPIV for measurement of turbulent fluid flow. *Experiments in Fluids*, 23 (1997), 449–462.

- [10] GRASMEYER, J. M., AND KEENON, M. T. Development of the black widow micro air vehicle. AIAA Aerospace Sciences Meeting and Exhibit, Jan 2001.
- [11] GRUNDY, T. M., KEEFE, G. P., AND LOWSON, M. V. Effects of acoustic disturbances on low re aerofoil flows. In *Proc. Conf. on Fixed, Flapping and Rotary Wing Vehicles at Very Low Reynolds Numbers* (Notre Dame, Ind., June, 2000 2000), pp. 91–113.
- [12] GYLLHEM, D., MOHSENI, K., AND LAWRENCE, D. Numerical simulation of flow around the colorado micro aerial vehicle. 35th AIAA Fluid Dynamics Conference and Exhibit, June 2005.
- [13] HOERNER, S. F., AND BORST, H. B. *Fluid Dynamic Lift*. Hoerner Fluid Dynamics, Bricktown, NJ, 1975.
- [14] JACOBS, E. N., AND SHERMAN, A. Airfoil section charactersitics as affected by variations of the Reynolds number. *NACA Technical Report 586* (1937).
- [15] KESTER, W. ADC input noise: The good, the bad, and the ugly. Is no noise good noise? *Analog Dialogue 40*, 02 (2006). <http://www.analog.com/analogdialogue>.
- [16] LAITONE, E. V. Wind tunnel tests of wings at Reynolds numbers below 70000. *Experiments in Fluids 23* (1997), 405–409.
- [17] LAITONE, E. V. *Fixed and Flapping Wing Aerodynamics for Micro Air Vehicle Applications*. AIAA, 2001, ch. Wind Tunnel Tests of Wings and Rings at Low Reynolds Numbers, pp. 83–90.
- [18] LENTINK, D., MULLER, U. K., STAMHUIS, E. J., DE KAT, R., GESTREL, W. V., VELDHUIS, L. L. M., HENNINGSSON, P., HEDENSTROM, A., VIDELER, J. J., AND VAN LEEUWEN, J. L. How swifts control their glide performance with morphing wings. *Nature 446* (2007), 1082–1085.
- [19] LISSAMAN, P. B. S. Low-Reynolds-number airfoils. *Annual Review of Fluid Mechanics 15* (1983), 223–239.
- [20] LYON, C. A., BROEREN, A. P., GIGUERE, P., GOPALARATHNAM, A., AND SELIG, M. S. *Summary of Low-Speed Airfoil Data vol. 3*. SoarTech Publications, Virginia Beach, Virginia, 1997.
- [21] MAXWORTHY, T. Experiments on the weis-fogh mechanism of lift generation by insects in hovering flight. part1: Dynamics of the fling. *Journal of Fluid Mechanics 93*, 1 (1979), 7–63.

- [22] MCGHEE, R. J., JONES, G. S., AND JOUTY, R. Performance characteristics from wind-tunnel tests of a low-Reynolds-number airfoil. AIAA 26th Aerospace Sciences Meeting, January 1988.
- [23] MCGHEE, R. J., WALKER, B. S., AND MILLARD, B. Experimental results for the eppler 387 airfoil at low Reynolds numbers in the Langley low-turbulence pressure tunnel. NASA Technical Memorandum, 1988.
- [24] MCMASTERS, J. H., AND HENDERSON, M. L. Low-speed single-element airfoil synthesis. *Technical Soaring* 4, 2 (1979), 1–21.
- [25] MUELLER, T. J., AND BATILL, S. M. Experimental studies of separation on a two-dimensional airfoil at low Reynolds numbers. *AIAA Journal* 20, 4 (1982), 457–463.
- [26] MUELLER, T. J., AND DELAURIER, J. D. Aerodynamics of small vehicles. *Annual Review of Fluid Mechanics* 35 (2003), 89–111.
- [27] OL, M. V., MCAULIFFE, B. R., HANFF, E. S., SHOLZ, U., AND KAHLER, C. Comparison of laminar separation bubble measurements on a low Reynolds number airfoil in three facilities. 35th AIAA Fluid Dynamics Conference and Exhibit, June 2005.
- [28] PELLETIER, A., AND MUELLER, T. J. Low Reynolds number aerodynamics of low-aspect-ratio, thin/flat/cambered-plate wings. *Journal of Aircraft* 37, 5 (2000), 825–832.
- [29] PELLETIER, A., AND MUELLER, T. J. Effect of endplates on two-dimensional airfoil testing at low Reynolds number. *Journal of Aircraft* 38, 6 (2001), 1056–1059.
- [30] RADESPIEL, R., WINDTE, J., AND SCHOLZ, U. Numerical and experimental flow analysis of moving airfoils with laminar separation bubbles. 44th AIAA Aerospace Sciences Meeting and Exhibit, Jan 2006.
- [31] RIEGELS, F. W. *Airfoil sections*. Butterworth, London, 1961.
- [32] SCHLICHTING, H., AND GERSTEN, K. *Boundary Layer Theory*. Springer-Verlag, Berlin, Germany, 2003.
- [33] SCHMITZ, F. W. *Aerodynamik des Flugmodells*. C. J. E. Volckmann Nachf. E. Wette, Berlin-Charlottenburg, 1942.
- [34] SELIG, M. S., DONOVAN, J. F., AND FRASER, D. B. *Airfoils at Low Speeds*. H.A. Stokely, Virginia Beach, Virginia, 1989.

- [35] SELIG, M. S., GUGLIELMO, J. J., BROEREN, A. P., AND GIGUERE, P. *Summary of Low-Speed Airfoil Data vol. 1*. SoarTech Publications, Virginia Beach, Virginia, 1995.
- [36] SELIG, M. S., LYON, C. A., GIGUERE, P., NINHAM, C. P., AND GUGLIELMO, J. J. *Summary of Low-Speed Airfoil Data vol. 2*. SoarTech Publications, Virginia Beach, Virginia, 1996.
- [37] SELIG, M. S., AND MCGRANAHAN, B. D. Wind tunnel aerodynamic tests of six airfoils for use on small wind turbines. *Transactions of the ASME 126* (2004), 986–1001.
- [38] SPEDDING, G. R., AND MAXWORTHY, T. The generation of circulation and lift in a rigid two-dimensional fling. *Journal of Fluid Mechanics 165* (1986), 247–272.
- [39] SRYGLEY, R. B., AND THOMAS, A. L. R. Unconventional lift-generating mechanisms in free-flying butterflies. *Nature 420* (2002), 660–664.
- [40] VAN DEN BERG, C., AND ELLINGTON, C. P. The vortex wake of a hovering model hawkmoth. *Phil. Trans. R. Soc. Lond. B 352* (1997), 317–328.
- [41] VIDELER, J. J., STAMHUIS, E. J., AND POVEL, G. D. E. Leading-edge vortex lifts swift. *Science 306* (2004), 1960–1962.
- [42] VOLKERS, D. F. Preliminary results of windtunnel measurements on some airfoil sections at Reynolds numbers between  $0.6 \times 10^4$  and  $5.0 \times 10^5$ . Internal Memorandum: M-276, <http://home.hccnet.nl/d.f.volkers/m276.ppt>, June 1977.
- [43] WEIS-FOGH, T. Quick estimates of flight fitness in hovering animals, including novel mechanisms for lift production. *Journal of Experimental Biology 59* (1973), 169–230.